ALMA MATER STUDIORUM
Università degli studi di Bologna

Dottorato di Ricerca in Fisica
XXV Ciclo - FIS/04

Study of the forward photons productions in pp collisions at $\sqrt{s} = 7$ TeV with the ZDC detector of the ATLAS experiment

Relatore:
Chiar.mo Prof.
Antonio Zoccoli

Correlatore:
Dott.
Matteo Negrini

Coordinatore Dottorato:
Dott. Fabio Ortolani

Candidato:
Simone Monzani

Anno Accademico 2012-2013

Introduction

The Zero Degree Calorimeters (ZDC) of the ATLAS experiment at the Large Hadron Collider (LHC) are compact hadronic calorimeters that are located exactly on the incident beam axis on either side of the interaction point (IP) in the ATLAS Detector, 140 m downstream from the IP. They thus observe forward going neutral particles that are produced in heavy ion (HI), pA or pp collisions.
The ZDC uses Tungsten plates as absorber material and quartz rods interspersed in the absorber as active media. The energetic charged particles crossing the quartz rods produce Cherenkov light, which is then detected by photomultipliers and sent to the front end electronics for processing. The ZDC are longitudinally segmented in 4 modules and some modules are also equipped with transverse position sensitivity. The first section (the one closer to the interaction point) acts as an electromagnetic calorimeter, while the remaining 3 act as a hadronic calorimeter. Both ZDC arms have the first hadronic module transversely segmented and, in one of the arms, the electromagnetic module is transversely segmented for position information about the incident particles. Each ZDC module individually provides energy and trigger information.
In heavy ion collisions the ZDC measures "spectator" neutrons, providing an important handle on Pb-Pb collisions centrality and allowing ATLAS to trigger on ultra-peripheral collisions. The ZDC is a versatile device in that it serve to study heavy ion physics, pp physics and provide a tool to tune both the HI and pp beams. It is designed to be as radiation hard as practicable, since the radiation levels in the position of the ZDC are extremely high.
While the ZDC is a physically small device, it occupies a large and critical region of phase space. The ZDC fills the transverse aperture of the neutral particle absorber (TAN) and captures all neutral particles leaving the interaction point with pseudorapidity η¿8.5.
Up to now the ZDC has been used for the analysis of HI interactions. This work presents the first results obtained with the ATLAS ZDC in the analysis of pp collisions at $\sqrt{s} = 7$ TeV, starting with the study of the detector calibration and performance in pp interactions, with the main goal to study the high energy photon production in p-p collisions, at the large energy that is available at the LHC.

This measurement will be compared with the predictions of different MonteCarlo generators (Pythia and EPOS) that are usually adopted in the simulation of minimum bias events at the LHC. These generators are tuned and validated only in the central part of ATLAS, while the ZDC measurement will help in understanding the MC generators behavior in the forward region.
This measurement has many drawbacks in the simulation of the impact of the high energy cosmic rays in the atmosphere.
In the following we will illustrate the physics potential of the device and will describe the ZDC detector in detail. The data analysis will start from the detector calibration, with particular emphasis on the measurement of electromagnetic shower. This is achieved through the reconstruction of the π^0 invariant mass peak, adopting approximations that are needed because of the specific ZDC design. A MC simulation of the detector will be used in order to test and validate data. Three generators has been tested and compared with experimental results: Pythia6, Pythia8 and EPOS, with different tunings.
After a description of the main features of the selected generators, they will be used to obtain predictions on the π^0 reconstruction and the energy and position distributions of single photon candidates in the ZDC.
Finally, the last chapter we will present the comparison between MC and data regarding the single photon energy distribution.

Contents

Chapter 1

ZDC physics

The Zero Degree Calorimeter (ZDC) of the ATLAS experiment has been designed for its use in Pb-Pb collisions, as a trigger for ultra-peripheral collisions and the measurement of the centrality of the heavy ions collisions.
In this work the ZDC will be used to study the high energy photon production in p-p collisions, at the large energy that is available at the Large Hadron Collider (LHC).
This measurement has many drawbacks in the simulation of the impact of the high energy cosmic rays in the atmosphere. The measurements can be compared with the predictions obtained using different MonteCarlo event generators, like Pythia and EPOS.

1.1 Cosmic rays

1.1.1 Energy distribution

While measuring cross sections and energy distributions in a new energy domain is inherently of value, a ZDC at the LHC is particularly useful for the understanding of the initiation of primary cosmic ray showers by high energy protons. At the LHC the proton energy is about $10^{17}eV$ in one of the proton's rest frame [1]. This energy is of particular interest in the study of cosmic rays since it is just above the *knee* in the cosmic ray energy spectrum [2]. Measurements in this region will give clues to understand the physical processes at play in the formation of primary cosmic rays.
It is interesting to note that at high energy colliders the acceptance of the detectors extends over a limited range in pseudo rapidity (η is usually less than 5, for ATLAS is 4.9) and is concentrated on hard scattering in the central region. On the other

hand, cosmic ray showers are mostly initiated in a more forward direction with soft scattering. Cross section measurements in this direction and at LHC energies will bear on cosmic ray production as protons strike the upper atmosphere, and will increase the understanding of the early generation of particle production in air showers.
It is difficult to confine cosmic rays in our galaxy when the primary energy exceeds $4 \cdot 10^{17} eV$, even when asymmetrical magnetic field of 3 μGs is assumed to fill the halo [4]. Within the present scheme of physics, it is very hard to conceive the source of the origin of such high energy particles, especially by a bottom-up scenario. Extra-galactic protons of this extreme energy are not expected to arrive at the Earth due to photo-nuclear interactions with 2.7K photons by the 3-3 resonance interaction process (formation of $\triangle 1232$ baryons). This is called the Greisen-Zatsepin-Kuzumin (GZK) cut-off [4]. It is also difficult for extreme energy extra-galactic particles other than protons to reach the Earth. Therefore, the existence of the events above the GZK cut-off (super GZK events) must be explained by a top-down scenario such as the decay of cosmic strings, Z_0, bursts [5] or by some yet unknown scenario. Within top-down scenarios, the hypothesis that Lorentz invariance might be violated under the bottom-up scenario is involved [6] [7]. Because of this situation it seems that a detailed study of super GZK cosmic rays may lead to a break-through in the field of fundamental particle physics and astrophysics. On the other hand the HiRes group has reported a cosmic ray energy spectrum that is consistent with the GZK cut-off [8] [9] [10] [11] as shown as the red points in Fig. 1.1.

Recently also the AUGER [12] experiment located in Argentina started to take data. According to the analysis made by this experiment, the existence of the GZK cutoff may have been confirmed, but important uncertainties remain in the interpretation of the experimental results and further work is required. In 2010 final results of The High Resolution Fly's Eye (HiRes) experiment confirmed earlier results of the GZK cutoff from the HiRes experiment. In Figure 1.2 (lower plot) we report a comparison between the 2 experiments [13]. This plot shows the fractional differences with respect to an assumed flux proportional to $E^{-2.69}$. HiRes I data [14] show a softer spectrum where the index is 2.69 while the position of suppression agrees within the quoted systematic uncertainties. The energy spectrum in Fig. 1.2 is based on around 20, 000 events. In the upper plot, the differential flux J as a function of energy is shown. The statistical uncertainties and 84% confidence-level limits are calculated according to [15]. Systematic uncertainties on the energy scale due to the calibration procedure are 7% at 10^{19} eV and 15% at 10^{20} eV, while a 22% systematic uncertainty in the absolute energy scale comes from the energy measurement made by the fluorescence detectors.
These results were brought into question when another experiment, AGASA [16],

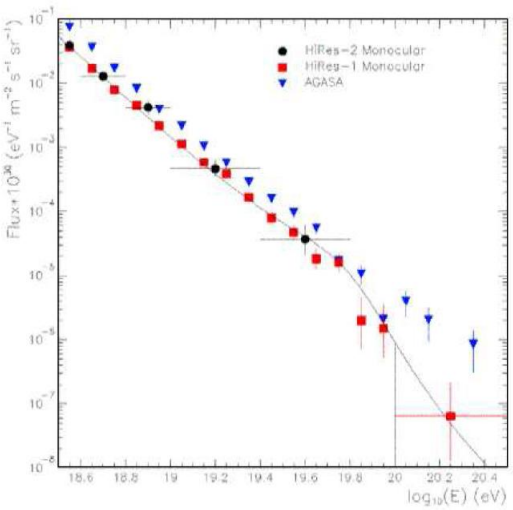

Figure 1.1: Energy spectra of cosmic rays at highest energies. Blue triangles represent the AGASA dat taken by an array of surface detectors, red and black marks represent HiRes data taken in Utah by the observation of fluorescence in the atmospheres. A clear discrepancy between AGASA and HiRes can be seen in the region over $10^{20}eV$ [4].

hinted at suppression of the GZK cutoff in their spectrum. The AUGER collaboration results agree with some parts of the HiRes final results on the GZK cutoff, but some discrepancies still remain [13].
These groups use quite different experimental methods, each of which has advantages and drawbacks. Many of the experimental procedures for deriving the energy spectrum depend strongly on the model of nuclear interactions that is used in MonteCarlo simulations of the air showers. Therefore, in order to calibrate the nuclear interaction models in the MonteCarlo codes, it is very important to establish the energy spectrum of particles emitted in the very forward region, which is effective for air shower development, at a much higher nuclear interaction energy than the UA7 case. The laboratory equivalent energy of LHC is $10^{17}eV$, therefore the calibration of MonteCarlo codes at such high energy will give a firm base to explore the GZK problem.
Here we must mention another important puzzle that present experiments cannot resolve, that is whether the cosmic ray composition or the nuclear interaction cross section changes at high energy. Cosmic rays are not purely protons but they also contain nuclei of helium, carbon and iron. When heavy nuclei enter the top of the atmosphere, they disintegrate quickly and nuclear cascade showers develop rapidly in comparison with the showers produced by protons. The impossibility to identify the primary nucleon leads to confusion on whether the primary composition or the

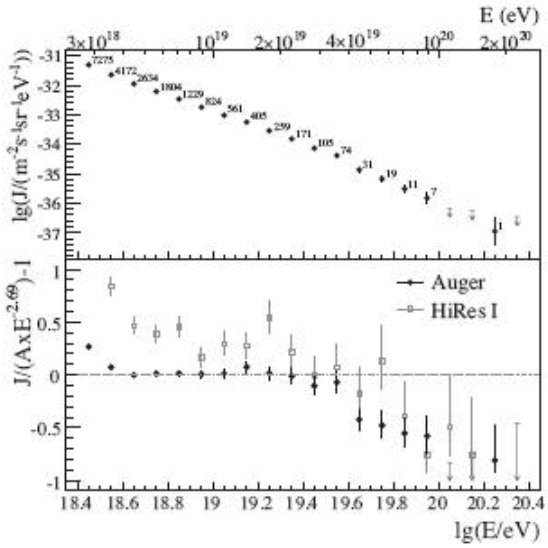

Figure 1.2: Upper panel: The differential flux J as a function of energy, with statistical uncertainties. Lower Panel: The fractional differences between Auger and HiRes I data compared with a spectrum with an index of 2.69 [4].

nuclear interaction cross section is changing with energy. The primary cosmic ray composition situation is presented in Fig. 1.3 [17]. The QGSJET model for the primary interaction model in a MonteCarlo code predicts that the composition of cosmic rays at $2 \cdot 10^{19} eV$ must be dominated by protons. However the DPMJET2.5 model indicates that the composition of cosmic rays is a mixture of several nuclei (protons, helium, carbon and iron) and that the composition does not change over a wide energy range.
The measurement of forward photons and π^0 production that is presented in this work will give insights on the production spectrum of secondary particles in the very forward region. The proposed measurement is important not only to fix the cross sections in the different MonteCarlo codes but can then be used to understand the composition of cosmic rays which cannot be determined by direct observations.

We have to consider also the case where the GZK cutoff is absent. This would directly lead to new physics for an explanation. Until now the concept of a cutoff comes from the fact that high energy protons interact with 2.7K background photons and lose energy and therefore cannot come from distant places. The AGASA group observed super GZK events while the HiRes group gave no super GZK events. The AUGER experiment is reporting no obvious super GZK events but the energy resolution is not enough at present to draw a definite conclusion on the GZK issue [4].

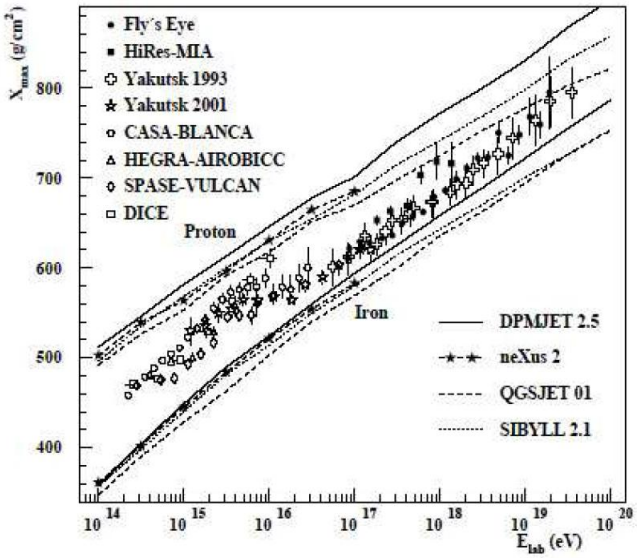

Figure 1.3: The position of the shower maximum X is shown as a function of the primary cosmic ray energy. The line corresponds to the prediction by the DPMJET2.5 model for iron primaries and proton primaries, while the dashed dotted curve represents the predictions by the QGSJET model. The dotted line reflects the predictions by the SYBILL2.1 model [4].

If the GZK cutoff exists, there should be also the following pair creation process:

$$p + 2.7K\gamma \rightarrow p + e^+ + e^- \tag{1.1}$$

This creates a dip in the cosmic ray energy distribution around 10^{19}eV. This dip is discussed in detail by Berezinsky [18]. If this dip is regarded as due to the pair creation process, the energy scale is under-estimated by 20% and the AUGER energy scale is under-estimated by 25% [18].
If this is the case, the AGASA energy estimate may be more accurate than the others. If the systematic error in the energy measurement by the experiments is not more than around 10%, the absolute energy calibration by the dip could be reliable and we can discuss the GZK issue on a firm basis. So far only two experiments have obtained data in the energy region exceeding $10^{17}eV$; the experiment that has been done by CERN UAT7 collaboration [3] and the LHCF experiment [4].
A ZDC measuring forward particle production cross sections presents a unique opportunity to make measurements in a region that is utmost importance for primary cosmic ray studies and to make the comparison with MC simulation predictions, using generators that are normally studied and tuned in the central pseudorapidity region. Only the LHCF experiment obtained results on the measurement of the

photon energy distribution in p-p collisions at $\sqrt{s} = 7$ TeV at the LHC along the p-p collisions as it is summarized in Fig. 1.4. The LHCF result shows an upper limit of 3 TeV for the proton energy distribution in the forward region [4].
The LHCF detector covered an η range between 8.81 and 8.99 and the result has

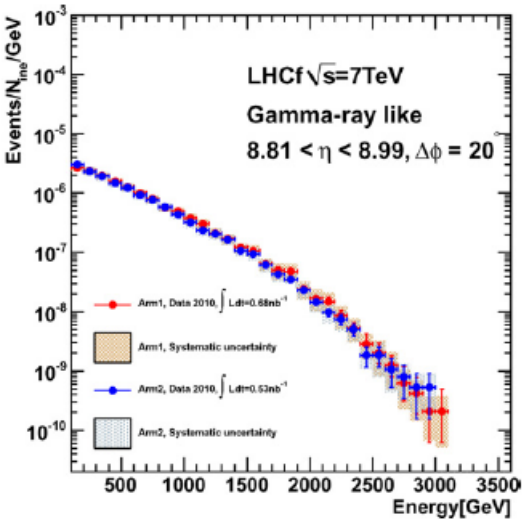

Figure 1.4: Single photon energy spectrum obtained by the LHCF experiment. These are results for Arm1 (red line) and for Arm2 (blue line) [4].

been obtained using a total integrated luminosity equal to 0.68 nb^{-1} for Arm1 (red line) and 0.63 nb^{-1} for Arm2 (blue line).

1.1.2 Model dependence of air shower development

Here we discuss the impact of model differences in the MonteCarlo simulation of shower development. In Fig 1.5 we stress the importance of measurements in the very forward region for cosmic ray phisics. The simulations have been performed using the DPMJET3 model that includes PYTHIA and PHOJET MC generators [19]. The simulated air showers have an inclination angle of 60 and a primary proton energy of $5 \cdot 10^{19}$eV.
Cosmic rays are selected in Fig. 1.5 with respect to the Feynman variable X_F. In inclusive hadronic interactions at large energies, this quantity is defined as the ratio between the longitudinal momentum of a particle P_L and its maximum value $P_{L(max)}$:

$$X_F = \frac{P_L}{P_{L(max)}} \tag{1.2}$$

where the maximum allowed longitudinal momentum is also equal to $\frac{\sqrt{s}}{2}$ with $\sqrt{s}$ the total center of mass energy of an interaction. Then Eq. 1.2 becomes:

$$X_F = \frac{2P_L}{\sqrt{s}} \tag{1.3}$$

Sometimes we can find the same equation relative to the transverse momentum P_T, in this case we have:

$$X_T = \frac{2P_T}{\sqrt{s}} \tag{1.4}$$

Using X_F to discriminate between showers, Fig. 1.5 shows the shower development produced by all components of the shower, the shower with photons emitted in the region $X_F > 0.05$ excluded (this cut also excludes π^0s with $X_F > 0.10$), the sower excluding all charged pions and neutral and charged kaons with $X_F > 0.10$ [4].
This result illustrates how important the contribution of the forward photons with $X_F > 0.05$ is for the total development of showers. The contributions of photons with $X_F < 0.05$ and $X_F > 0.05$ are similar in magnitude so we must know precisely the production cross section for the small number of high energy secondary particles emitted in the very forward region in order to adequately simulate shower development.
To see the impact of model differences in shower development it is possible to change the primary interaction model in the MonteCarlo code in the region $X_F = 0.01 - 1.0$ as it has been done in [4]. The models have been built to fulfill energy conservation. As Fig 1.6 and 1.7 show, the model A production curve deposits its energy deeper in the atmosphere, while model B leads to the early development of showers. It is not possible to know whether pion production can ben explained by model A or model B or something in between. Without accurate knowledge of the production cross section of secondary particles in the very forward region, we may misidentify the primary particle, mistaking protons for iron nuclei and viceversa.
Fig. 1.6 and 1.7 indicate another very important point for this analysis. If we measure a giant air shower at an altitude of $900 g/cm^2$, we can misidentify the energy of the showers by a factor of 1.75, due to the difference in shower development between models A and B. This possibility may resolve the shower energy between the AGASA and HiRes groups that was shown in Fig 1.1. If we reduce (increase) the absolute value of the energy measured by AGASA (HiRes) group by 20% than the AGASA and HiRes data agree rather well. This uncertainty must be proven by future experimental measurements.

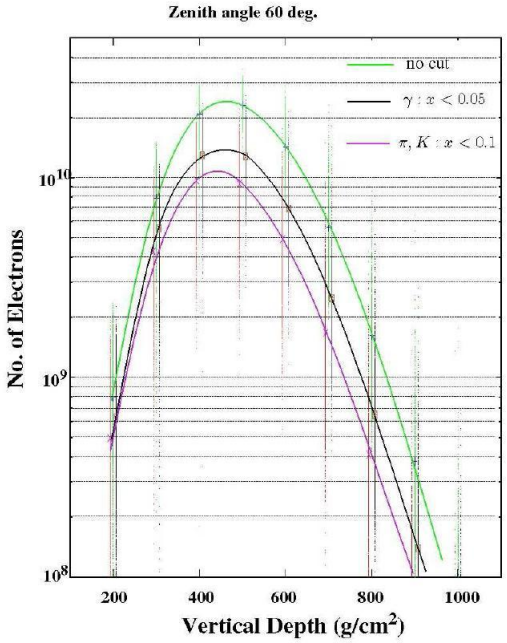

Figure 1.5: The transition curve of proton showers calculated by the DPMJET 3 model for primary proton energy $5 \cdot 10^{19}$eV. The top curve shows the shower curve without cutting any kinds of particles. The middle curve shows the showers created only by photons with Feynman variable $X_F < 0.05$. The bottom curve represents the showers created by pions and kaons with Feynman variable $X_F < 0.1$ [4].

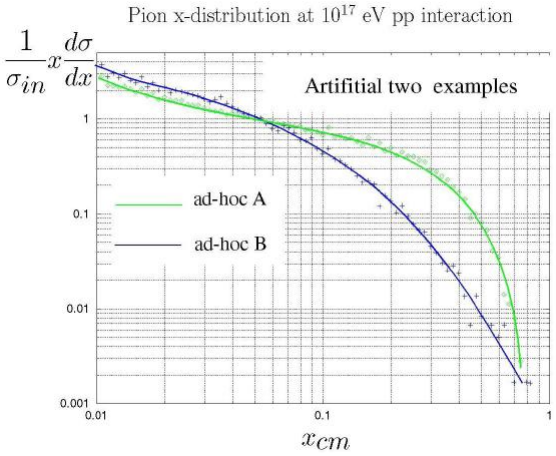

Figure 1.6: Two different production models A and B of secondary particles presented as a function of the Feynman variable X_F in the center of mass for primary energy of $1 \cdot 10^{19}$ eV [4].

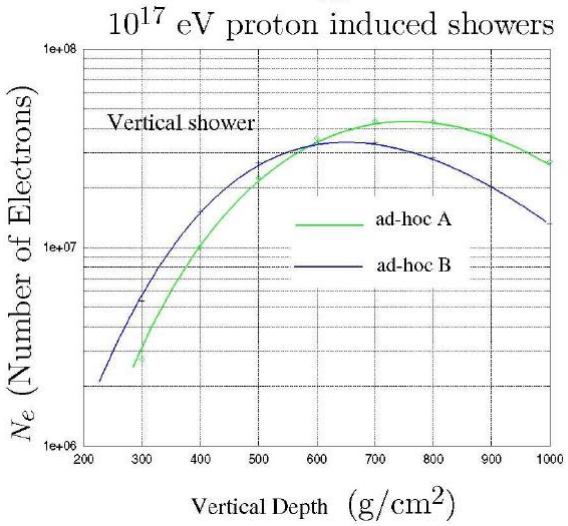

Figure 1.7: Shower development curve for both models. At $900 g/cm^2$ the number of particles differs by a factor of 1.75 between the models [4].

1.1.3 Impact of the ZDC measurements on cosmic ray physics

In this analysis we will measure the photon energy spectrum in the forward region in pp collisions at the LHC with $\sqrt{s} = 7$ TeV. This measurement has important drawbacks in high energy cosmic rays physics.
The important quantities governing HECR (high energy cosmic rays) air shower development are:

- the forward production energy distribution of photons and neutral pions;
- the leading particle spectrum;
- the total inelastic cross section.

ZDC can provide information on the first 2 points but we are not able to access the third directly. The TOTEM experiment instead, has been designed to provide a precise measurement of the total inelastic cross section [4]. The air shower observation experiments generally rely on MonteCarlo simulations of air showers when they derive the incident cosmic ray energy. Except for the muon component, air shower development is sensitive to the particles generated in the forward region. At energies over 10^{15} eV there is no accelerator calibration of the MonteCarlo codes for the hadronic interaction; so the difference among the codes become sizable [4]. For instance the π^0 and photons X_F-distributions show differences. The leading particle spectra also show sizable differences for $X_F > 0.7$. The leading particle

difference is reflected in the leading particle neutron spectrum which we can measure with the ZDC. Cosmic ray interactions in air are not with a proton target, but the nucleus effect in the forward region is expected to be small. Then we can use LHC pp interactions to compare different MonteCarlo models that can be used to simulate UHECR.

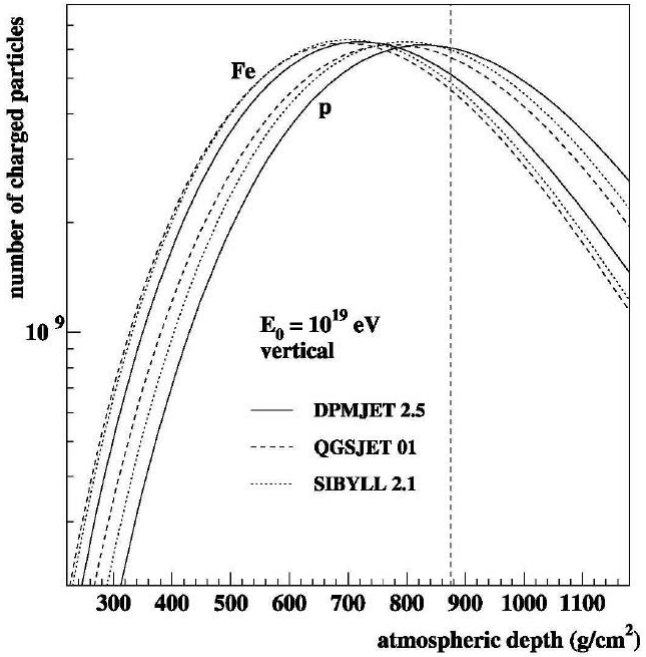

Figure 1.8: The shower development curves obtained from three interaction models, DPMJET2.5, QGSJET, SIBYLL2.1. They predict different atmospheric depth for the shower maximum. The doted vertical line shows atmospheric depth at the AUGER site. Number of charged particles in the shower at the site depends on the interaction models [17].

The difference between the models of air shower development appear in the number of electrons and positrons (N_e) in the air shower observed a at given atmospheric depth. For example we see a systematic difference of around 20% in N_e for 10^{19}eV incident proton air at the AUGER site shower (shown as the dotted vertical line), as it is shown in Fig. 1.8 [17]. Near the shower maximum the difference is not so large but generally showers are observed over a wide range of depths. The ZDC can provide information on the forward production energy distribution of photons and neutral pions (the scope of this thesis) and the leading particle spectrum and helped in the discrimination between the models and reduce the systematic errors due to the difference in MonteCarlo codes. What is important is that none of the

codes used in the calculation of Fig. 1.8 may be close to reality; the ZDC results may in principle lead to quite different spectra. A systematic difference of around 20% in the flux of electrons and positrons given by the particle production models leads to 50% difference in the flux of primary cosmic rays. This may also influence the GZK cutoff.

1.2 Use of the ZDC in HI physics

The primary role of the ZDC in heavy ion physics (HI) is in event characterization of HI collisions. The following requirements drove the detector design, as it will be illustrated in Section 2.
When heavy ions collide only a portion of the ions overlap and interact. Those interacting nucleons are called *participant* nucleons and those that travel essentially unaffected are called *spectators*.
The spectators neutrons, observed by the ZDC, carry the nominal beam energy. Due to Fermi motion of the nucleons in the initial nuclei, their energy has about a 10% dispersion and their position at the ZDC has an RMS 6 mm scatter about the central value. The energy of the spectator neutrons as measured by the ZDC allows the determination of their number. The ZDC can thus determine the participant number in an unbiased way by sampling the spectators neutrons. Measurement of the number of spectator neutrons is equivalent to measuring the magnitude of the impact parameter or *centrality* of the collision since the more central the collision, the larger the number of widely scattered particles.
The spectator neutrons also receive a small amount of transverse momentum. Their momentum vectors, in combination with those of the incident ions, form a plane which is called *the reaction plane*. Since the ZDC can also measure the transverse position of the spectator neutrons, they can determine the orientation of this reaction plane. We use the first term in Fourier expansion of the azimutha distribution of particles in a HI event to describe the directed flow. This is found to increase linearly with rapidity, reaching a maximum in the beam fragmentation region covered by the ZDC. The orientation of the flow and hence the reaction plane is observed by the displacement of the center of gravity of the ZDC energy deposition, a measurement well suited to the ZDC design. It should be noted that a lack of spectator neutrons can be a result of central collisions or *ultra-peripheral* collisions in which many neutrons remain bound in larger nuclear fragments. It is through observation the central particle multiplicity in the ATLAS inner detector (ID) that this ambiguity can be resolved and the centrality of the event determined.

An example of this can be seen in Fig. 1.9,where the correlation between the total transverse energy deposited in ATLAS calorimeters and the amplitude signal

from the ATLAS Zero-Degree Calorimeters is presented.
The correlation corresponds to the interplay between hadronic interactions of the

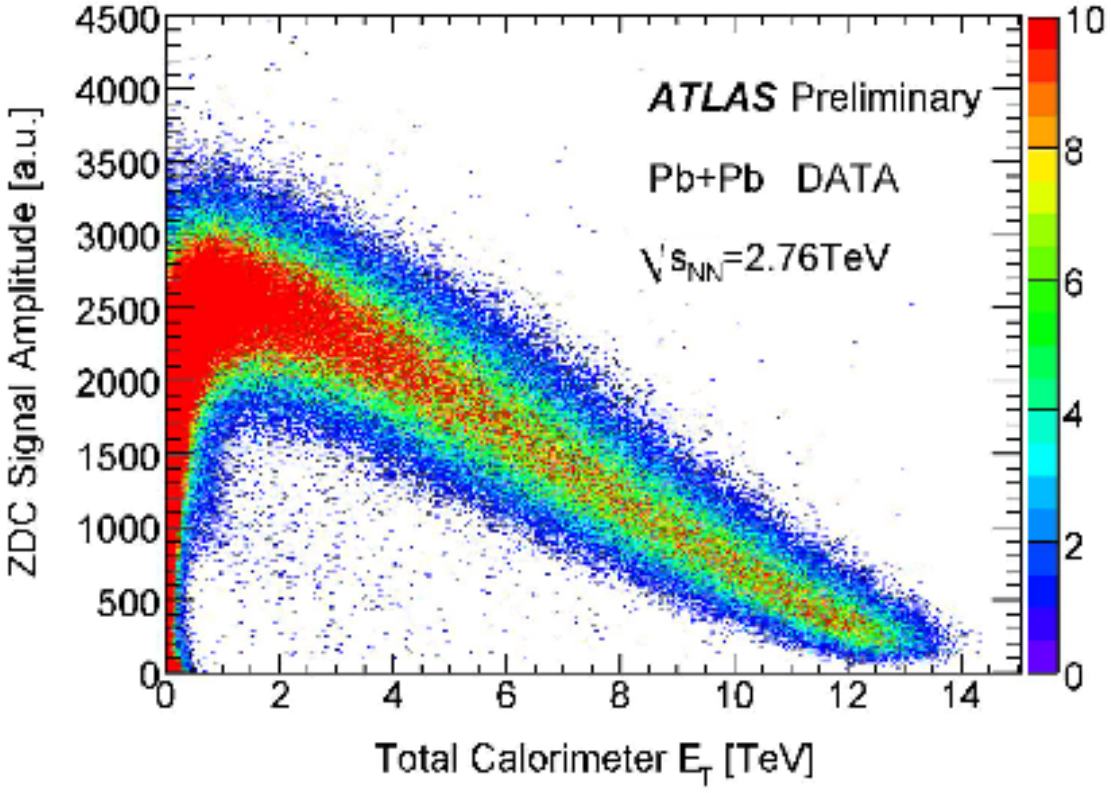

Figure 1.9: Correlation between the total transverse energy deposited in ATLAS calorimeters and the amplitude signal from the ATLAS Zero-Degree Calorimeters for Pb-Pb collisions at $\sqrt{s}$=2.76 TeV.

colliding nuclei and Coulomb interactions of the colliding nuclei in Ultra-Peripheral Collisions (UPC). For low transverse energy (E_T), the events come primarily from the UPC through exchange of one or more photons, exciting one or both nuclei, which subsequently de-excite through neutron emission, the neutrons continuing in the forward direction. For these reactions, the number of neutrons impacting the ZDC can be large, e.g. up to several dozen neutrons. In this plot, up to 10 neutrons are seen. In this case, little energy is deposited in the rest of ATLAS. Signals with large E_T indicate hadronic interactions of the nuclei, which cause deposits of energy in the central ATLAS that can be very large (exceeding 12 TeV in this plot). Peripheral collisions involving hadronic interactions (in distinction to the Coulomb-only interactions) occur at smaller values of E_T and these also deposit large numbers of neutrons in the ZDC. This is because most of the nucleons in

the nucleus continue to move forward with nearly the same energy as before the collision, as quasi-spectators of the collision. More central hadronic collisions tend to have many fewer spectators, leaving little in the way of forward-going nuclear fragments, thus the energy deposition in the ZDC decreases as E_T increases.
Finally, the ZDC is needed to tag a wide variety of topics in ultra-peripheral HI collisions such as hard photo-production and quasi elastic vector meson production. In these events there is relatively little central detector activity and a ZDC coincidence is a useful complement to the trigger.
In Heavy Ion running the ZDCs have proven to be a valuable tool in luminosity calibration. Electromagnetic dissociation (EMD) with neutron emission can be reliably determined using the Weizsacker-Williams formalism, and the effective cross section for ZDC minimum bias trigger coincidences has been calculated for LHC Pb-Pb collisions [20]. With RHIC data it was shown that EMD events can also be identified [21] and used to provide an independent luminosity calibration to about 5%.

Chapter 2

The ZDC detector

The ATLAS Zero Degree Calorimeter (ZDC) at the Large Hadron Collider (LHC) is a set of two sampling calorimeters modules symmetrically located at 140m from the ATLAS interaction point. The ZDC covers a pseudorapidity range of $|\eta| > 8.3$ and it is both longitudinally and transversely segmented, thus providing energy and position information of the incident particles. The ZDC is installed between the two LHC beam pipes, in a configuration such that only the neutral particles produced at the interaction region can reach this calorimeter.
The ZDC uses Tungsten plates as absorber material and rods made of quartz interspersed in the absorber as active media. The energetic charged particles crossing the quartz rods produces Cherenkov light which is then detected by photomultipliers and sent to the front end electronics for processing, in a total of 120 individual electronic channels. The Tungsten plates and quartz rods are arranged in a way to segment the calorimeters in 4 longitudinal sections. The first section (the one closer to the interaction point) acts as an electromagnetic calorimeter ($32X_0$) while the remaining 3 act as a hadronic calorimeter (1.2λ each). Both ZDC arms have the first hadronic module transversely segmented in 24 channels and, in one of the arms, the electromagnetic module transversely segmented in 64 channels for position information about the incident particles (pixels).
Each ZDC module individually provides energy and trigger information using a dedicated set of quartz rods that are grouped together and connected to a photomultiplier tube (BigPMT). The ZDC encounters its main motivation in Heavy Ion Physics, providing trigger and energy measurements based on the spectator neutrons dissociated from the colliding nuclei. In fact, this is the only trigger available for ultraperipheral interactions where very little activity is present at central rapidities. Besides the heavy ions, the ZDC can also be used to measure the forward neutral particle production in low luminosity proton-proton runs.
In the following sections we will provide further details about the detector and its performance.

The ZDCs reside in a slot in the neutral beam absorbers (TAN). Fig. 2.1 schematically shows the location of the TANs and thus the ZDCs. The TAN is located 140 m from the IP, and is required to absorb the flux of forward high energy neutral particles that would otherwise impinge on the twin aperture superconducting beam separation dipoles. The ZDCs are placed in a slot in the TAN that would otherwise contain inert copper bars as shielding, at the point where the beam pipe transitions from one pipe to two. Fig. 2.2 shows two configurations of ZDC modules in the TAN. The two configurations are discussed in section 2.1.

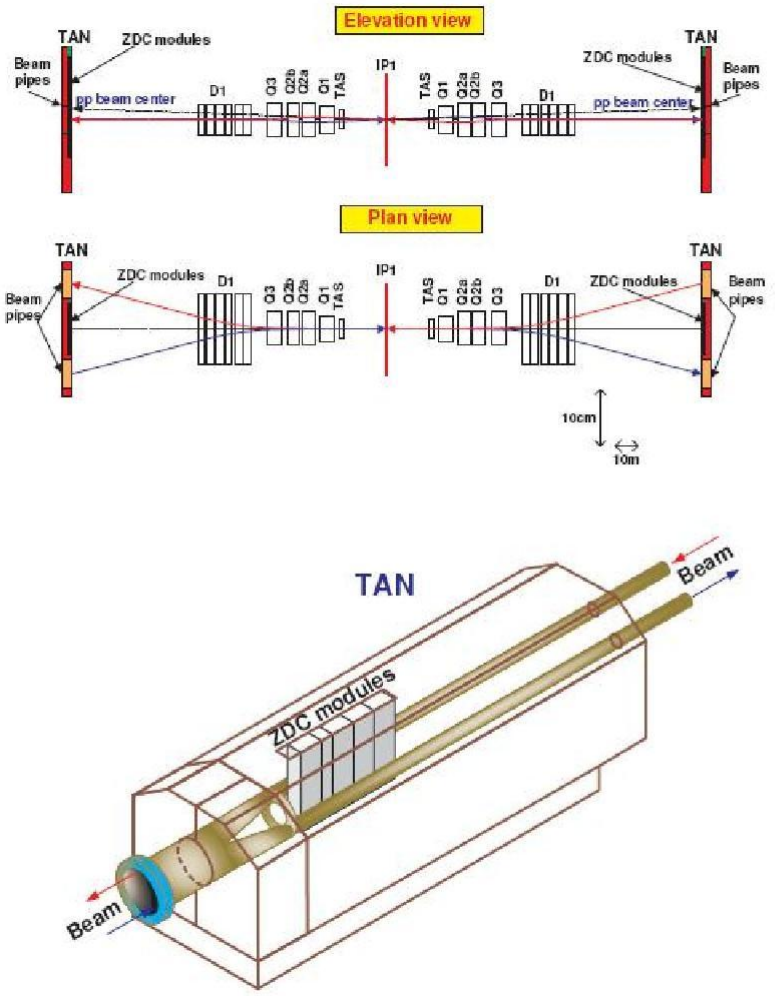

Figure 2.1: LHC beamlines in the region of IP1 showing the location of the ZDCs (left). Transparent view of the TAN showing the beam pipe and location of ZDC modules (right). The TAN is 140 m from the IP [1].

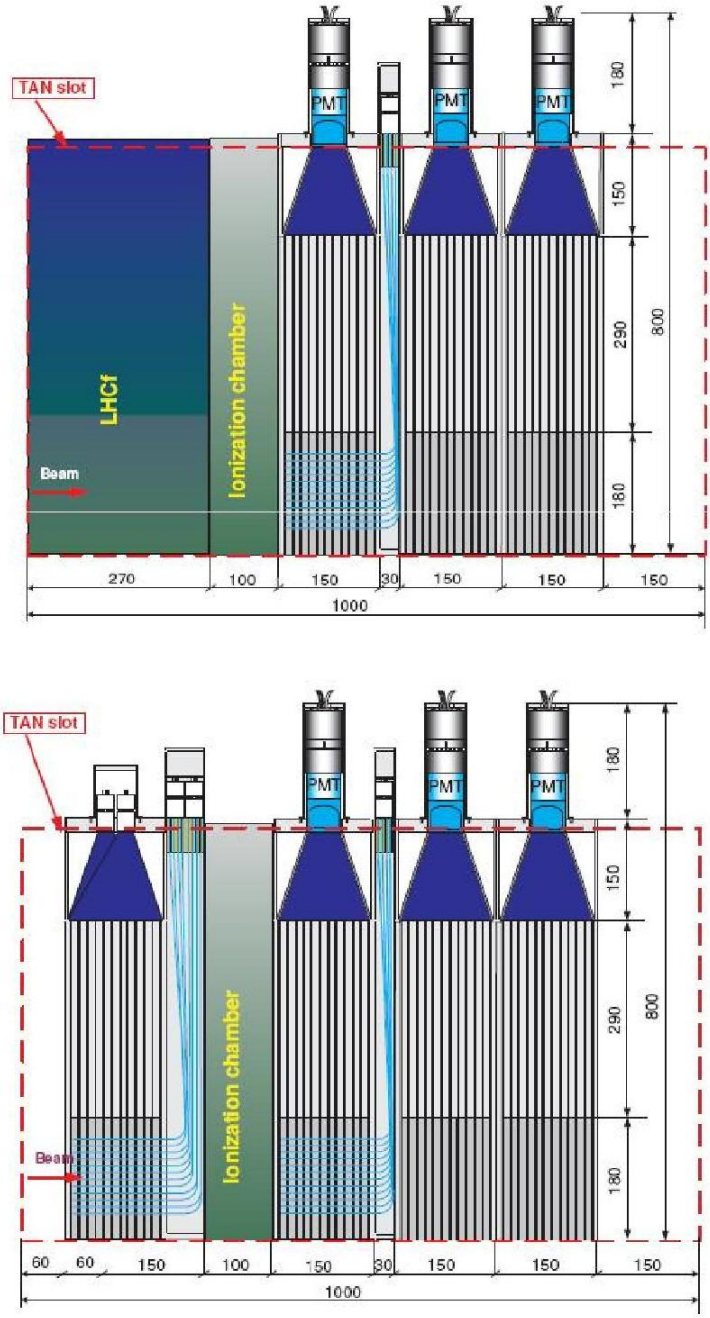

Figure 2.2: ZDC modules as situated in TAN during running for Phase I (top), and Phase II (bottom). The two configurations are discussed in section 2.1 [1].

2.1 ZDC Module Description

The ZDC is composed by four modules: one electromagnetic (EM), about $32X_0$ thick, and 3 hadronic (each about $1.2\lambda_{int}$ thick) on each arm. In describing the modules we will first describe the EM module since the hadronic modules are similar.
For one arm the EM module is shown in Fig. 2.5 . It consists of 11 tungsten (W) plates 91.4 mm wide, 180 mm high, and 10 mm thick in the beam region, with steel plates extending above for 290 mm. 1.0 mm diameter Quartz rods penetrate the W plates parallel to the beam in an 8x8 matrix transverse to the beam. At the front end of the module the rods are bent 90 vertically and are optically coupled at the top of the module to multi-anode phototubes (MAPMTs). Cerenkov light from shower products of incident particles is captured by the quartz rods and observed by the multi-anode tubes. The position of the rods with Cerenkov light signal corresponds to the transverse position of the incident particle, and the intensity of the light reflects the energy of the particle. The position sensing rods are usually called *pixels*. There are no position sensing rods in the EM module on the other arm.
EM pixels are all placed at the distance of 1cm by each other at the vertices of a square. In Had1 modules, pixels forming a 8x10 matrix are grouped in a total of 24 read-out channels, as it is shown in Fig. 2.3).
Between the plates are placed 1.5 mm quartz strips that run vertically and are viewed by one photomultiplier tube from above via air light pipes, or funnels. These strips are actually rows of quartz rods which we term strips to distinguish them from the above described position measuring rods. They are depicted in Fig. 2.4. The purpose of the strips is to get the measurement of the incident particle energy.
Also, the hadronic modules only have one funnel. Groups of spectator neutrons remain together and appear as a single, large neutron.
Multi-anode phototubes (Hamamatsu R8900-03-16 [22]) are employed for the position sensing function: one hadronic module on each arm with two tubes on each, and one electromagnetic module with six tubes in one arm, while the electromagnetic module in the other arm has no coordinate readout. We will use Photonis XP3292B tubes [24] for single funnels.

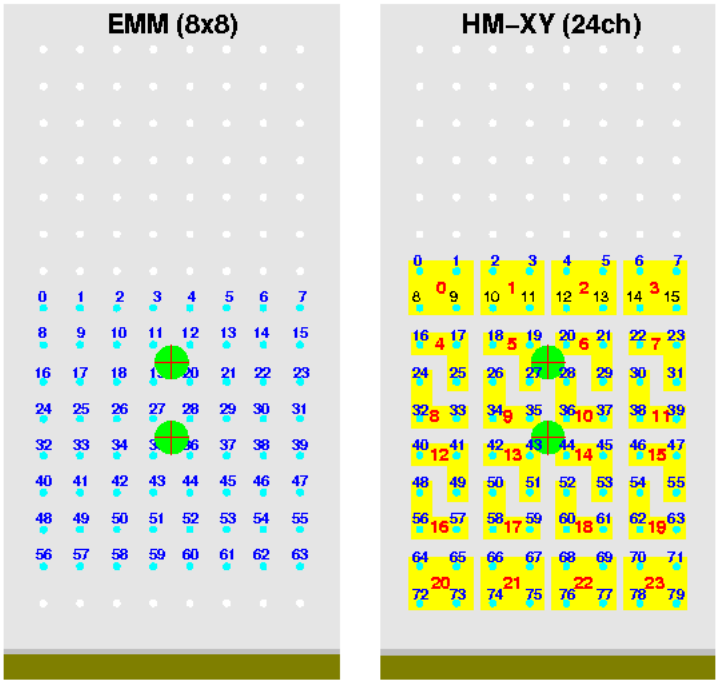

Figure 2.3: The hadronic (a) and electromagnetic (b) modules with the fiber number indication [1].

2.2 Data Acquisition System

2.2.1 ATLAS Readout Protocols

It is briefly recalled here that ATLAS operates the TDAQ system with three trigger levels [25, 26]. The first trigger level (L1A) will carry out a rate reduction from 40 MHz down to at most 100 kHz. The second level trigger (LVL2) will reduce the rate by almost two orders of magnitude (3-4 kHz), and the Event Filter (EF) will bring down the recorded rate to the order of 100 Hz.
The ATLAS TDAQ is functionally decomposed into four blocks: the ReadOut subSystem (ROS) including L1A logic, the LVL2 trigger with the the Regions Of Interest (ROI) selection, the Event Builder (EB) and the Event Filter I/O (EF I/O). The ROS is implemented in dedicated hardware while the last three blocks are implemented as processor farms.
The ROS is the main interface between 1600 detector front-end readout links and the high-level trigger farms. This subsystem, on the L1A request (around 100 kHz), is responsible for transferring/receiving event fragments (by parallel streams via optical links and RODs - ReadOut Drivers) from Front End Electronics on

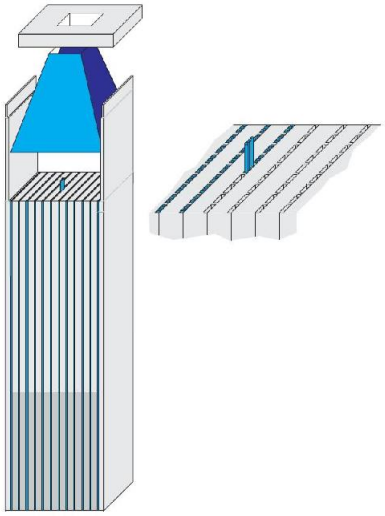

Figure 2.4: Detail of configuration of strips. Left: isometric schematic drawing of the module. Beam enters from the left. Right: isometric drawing of the top of the steel with rods being inserted. Groups of 1.5 mm rods form the strips [1].

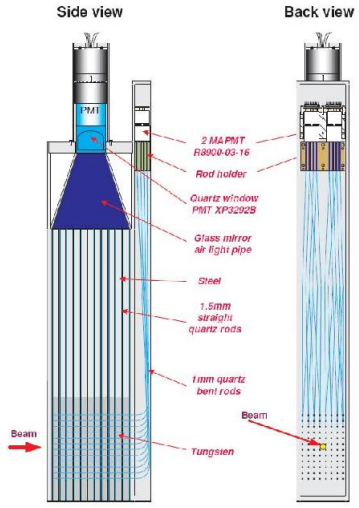

Figure 2.5: ZDC module. It has only one PMT viewing the strips, and two MAPMTs viewing the rods [1].

the detectors (FEEs) to a fragmented PC-based ReadOut Buffer (ROB) subsystem. There the data are stored in the corresponding Readout-Buffer Inputs [27] (ROBIns) which are custom-made core devices of the ROB subsystem and which are capable of handling events at a latency of up to 100 ms, for forwarding for analysis on the LVL2 request or the EB request.
A concurrent part of the ATLAS TDAQ system is a Timing, Trigger and Control (TTC) subsystem [28] that distributes an LHC clock and trigger signals to the readout electronics via a special optical link.

2.2.2 ZDC ROS scheme

In designing the ZDC ROS scheme, the ATLAS TDAQ protocols, the 100 kHz L1A trigger rate, and the demands of the ZDC resolution, among other issues were considered.
The ZDC also provides an input to the L1A trigger. For HI running this consists primarily of a 2 arm coincidence with a 0.5 TeV threshold. For pp running it consists of 1 arm signal above a 0.5 TeV threshold with a prescale. The ZDC triggers as a NIM logic input through the Central Trigger Processor CALibration (CTP CAL) module, which acts, according to its specifications [29], as a patch panel for NIM inputs from small sub-detector systems [30]. Since the ZDC signals arrive at USA15 1.4 μsec after the crossing, the trigger will fit in the 1.8 μsec time specification for the CTP response.
These considerations lead us to the following specification of the ZDC Readout Scheme:

- The ZDC readout schematic has to include two independent arms under control of a common global L1A-trigger. One arm includes the readout of a combined hadronic/electromagnetic calorimeter (4 ZDC modules) that contains energy/timing PMTs and 24 coordinate PMT channels for one ZDC module. Another arm includes the readout of a combined hadronic/electromagnetic calorimeter that contains 7 energy/timing PMTs, 24 coordinate PMT channels for one ZDC hadronic module and 64 coordinate PMT channels for the ZDC electromagnetic module.

- Due to the high radiation level, digitized electronics could not be located around the ZDC detector. In this case, all analog PMT signals have to be amplified and sent, via coaxial cables, to special ZDC receiver modules in USA15. Here each signal is processed by a variable gain amplifier/shaper, which produces a unipolar differential output signal with full length of around 60 ns and amplitude within -1 - 0 V range.

- To reach the required energy and timing resolution, all energy/timing PMT signals (11 channels) should be digitized, at least, by 14-bits 80 MHz Wave-Form Digitizer (WFD). The dynamic range of 14 bit is set by requirements of detecting 100 GeV hadrons/photons in pp running, and a cluster of up to 70 2.75 TeV (spectator) neutrons in HI running.

- To reach the required coordinate resolution, 144 signals of the coordinate PMTs should be digitized by 14-bits 40 MHz WFD.

- Capability for pile-up analysis of the ZDC response in a time window of 125 - 150 ns (around 5 crossings: 1 past, present and 3 - 4 future) requires a minimal event readout length of 10 - 12 amplitude samples for the ZDC energy/timing channel and 5 - 6 amplitude samples for the ZDC coordinate channel.

- Each WFD channel has to be "dead-time-less" and each WFD channel or group of the WFD channels has to include a WFD pipeline buffer for acquisition and for a parallel readout.

- Each WFD pipeline buffer must include the possibility of reading the digitized data out of a firmware-defined window of the WFD pipeline buffer (under control of an "on-board" FPGA), and to transfer these data to the module‘s output buffer.

- A shift of this window inside of the WFD pipeline and the depth of the window has to be programmed into the FPGA firmware.

- Each ZDC readout arm has to include one collecting ROD to collect various components of the event format (header, data and trailer) and to build the event fragment according to the ATLAS TDAQ protocols. This ROD must also include the possibility of data transfer to a high level of the ZDC ROS (ROBIn) via a 160 Mbytes optical link - High-speed Optical Link (HOLA)[31].

- The whole ZDC readout system has to include a special module of the TTC subsystem that will distribute the LHC clock and the L1A trigger signal to every module of the ZDC ROS system via a special bus and will also provide an interface to the ATLAS DCS.

This specification for the ZDC readout leads us to employ electronic modules developed for the ATLAS Level-1 Calorimeter Trigger system (L1Calo) [32]. Three main components of this electronics will be needed:

- The PreProcessor Module (PPM): Digitizes, processes 64 analog signals, and identifies them with specific bunch crossings. The 10-bit PPM FADCs will digitize the signals with a sampling frequency of 40 MHz, the same as the bunch crossing rate for the accelerator. The digitized values will be sent then to a custom PreProcessor ASIC (PPrASIC), which has a 2.5 μs pipeline memory to store the raw digitized values and processed data. These data will be readout via an 800 Mbit/s serial optical G-link to the next stage of DAQ upon a L1A trigger.

- The ROD module: Receives, formats, compresses, and buffers the PPM transmitted data. The ROD also receives the L1A signal and some data for the ATLAS ROD fragment header via the TTC subsystem. When all required information has been received from the TTC subsystem and PPM, the ROD assembles a complete ZDC event fragment with header, PPM data, and trailer. The ROD then sends the completed fragment to the ZDC ROBIn via a HOLA S-link

- The Timing Control Module (TCM): Distributes the LHC clock to every PPM or ROD module and provides an interface to the ATLAS DCS, which monitors and controls the operating conditions of the experiment.

The performance level that can be achieved with this technique is consistent with the ATLAS TDAQ protocols and needs of the ZDC readout.
The block-diagram and schematics of the ZDC readout is shown in Fig. 2.6.

- To achieve the 14-bit resolution for the the coordinate PMTs, the analog signals is split and amplified into two output differential signals with relative amplification of 1:10. This is done by special ZDC receiver modules. The subsequent processing of these split signal pairs by pairs of the 10-bit FADCs emulates the 14-bit signal digitization.

- In reaching the 14-bit 80-MHz scale for the energy/timing PMTs, these analog signals is split and amplified into two pairs of output differential signals with relative amplification of 1:16, which also represents the high gain (HG) and low gain (LG) channels. Each pair of split signals is combined with another pair of split signals, delayed by 12.5 ns, and digitized by a pair of 10 bit FADC. This emulates 14-bit digitizing at 80-MHz speed.

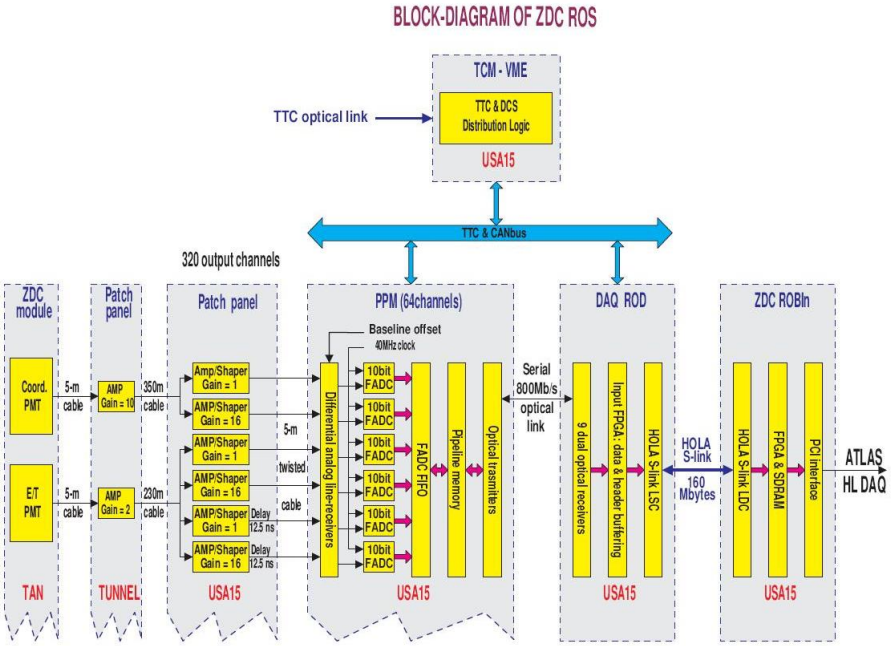

Figure 2.6: A schematic diagram of ZDC ROS. See text for details [1].

2.3 Data Acquisition System Calibration and Monitoring

2.3.1 Flashers

Measurements over a long period of time and the lack of access to the tunnel requires that the PMTs be monitored. Monitoring the gains to an accuracy of around 1% is sufficient, and can be achieved with a system based on blue LEDs - for instance NICHIA NSPB310A [33]. Using a controllable generator located in USA15, we excite the LED in the tunnel. On each MAPMT we have reserved one pixel to receive a fiber connected to the LED, and one fiber each illuminates the single channel PMTs. Tracking the stability of the LEDs is accomplished by observing their light output with PIN diodes, for instance Hamamatsu S1722-02 [23].

2.3.2 Particles

Full calibration of the ZDC detector begins with determination of the gains in all rod/phototube chains, and measuring shower shape distribution functions,

e.g. the dependence of single rod amplitudes on the distance to the shower center. These parameters will be permanently monitored during the LHC run. As described in Ref. [34], the full calibration of the EM up to a common normalization coefficient can be done even if the energy and coordinates of the photons are not known.

In pp collisions, this preliminary calibration is followed by an in-situ calibration using π^0 decay. This method, described in *Comment to the ECAL calibration algorithm* by A.A. Poblaguev Ref. [35] and in section **??**, uses events where there are two and only two photons in the detector. It is based on a previous parametrization of transverse EM shower profiles as observed in the quartz rods. This will be obtained through shower shape analysis at the LHC.

Once an Electromagnetic module has been calibrated, the hadronic modules will be calibrated. This will be done with $\Lambda \to \pi^0 n$ events in pp collisions. These events will be selected as having one and only one neutron, and two and only two gammas whose invariant mass is that of a π^0 when the decay vertex is taken as coming from downstream from the IP. Events whose invariant mass is in the peak of the mass spectrum will be chosen as calibration events. Once the π^0 has been reconstructed the angle between the neutron and π^0 trajectories is known, and we will use the method of Ref. [35], assuming the event was caused by a Λ decay, to calibrate the counters.

One might think that having three modules to absorb the full neutron energy in Λ decay would make this method problematical, but as was demonstrated in a test beam run, we correctly simulate the distribution of hadronic energy deposited in individual modules for different amounts of material in front of those modules. Again, this procedure has been demonstrated to work with Monte Carlo data.

When the collider switches to heavy ions, peripheral ion collisions provide a sample of mono-energetic neutrons with energy corresponding to their original momentum inside the nucleus. With these it is possible to have a redundant check of our calibration constants.

As mentioned above, monitoring the gains of the tubes in the ZDC system is done by flashers. The stability of the gains is also monitored with single photon distributions. Individual pixel gains differ by factors as large as 2 or 3 within a MAPMT. Once determined in initial calibration, however, these gains are constant relative to one another to one percent as observed at RHIC. They can be monitored with single photon distributions, but only the overall gain of a tube should need adjusting.

2.4 Design detector performance from simulation

2.4.1 Resolution

The design spatial and energy resolution of the ZDC system have been determined by means of a full detector simulation based on GEANT4 plus a program to describe light propagation and attenuation in rods, as well as the response of the phototube. Figure 2.7 displays the result of the simulation for photon and neutron energy resolutions of the ZDC system as described above. Figure 2.8 displays the position resolution for the two. Figure 2.9 shows the time resolution for neutrons. The time resolution for photons is about the same as that of neutrons.
The EM energy resolution of the strip readout settles to about 4%, while that of the hadronic modules (neutrons) is about 20% at 1 TeV. Spatially, the resolution for 1 TeV photons is about 0.5 mm and that for the neutrons is roughly 1 mm. One also sees that the time resolution for neutrons is in the 100 ps range, as is the time resolution for 1 TeV photons.
As an example of the resolution of a ZDC in heavy ion collisions, Fig. 2.10 shows the sum energy of spectator neutrons as measured by a $33cm^2$ area centered on the neutron spectator cluster vs. the known number of spectator neutrons. Several hundred events were generated by HIJING for each particular number of spectators.
The $33cm^2$ area was chosen on an event by event basis and analyzed to obtain the energy and measured centroid of the cluster of neutrons. The uncertainty in the measured energy is dominated by the fluctuation of the number of participant neutrons impinging on the selected 33 matrix for each event and the fluctuations of energy deposited in the module. Clearly in HI events with such large neutron multiplicities our ability to reconstruct π^0s will be limited, but this is not a major objective for the HI program.

2.4.2 Geometric Acceptance

The configuration space acceptance at 140 m from the IP is displayed in Fig. 2.11 where the limitations of all upstream apertures are projected to the 140 m point and superimposed to the detector scheme.
We have used the region that is free of the limitations of apertures in our calculations of signal. For background calculations, using GEANT4 we have allowed particles to scatter off the walls of the limiting components. These calculations have been found to be consistent with those of Ref. [36].

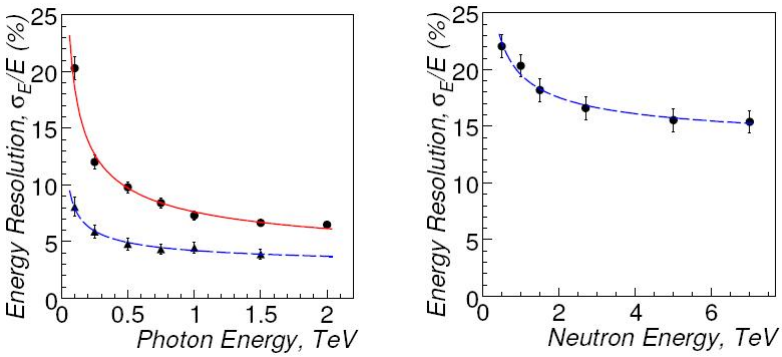

Figure 2.7: ZDC energy resolution for photons (a) and neutrons (b) as a function of energy of the respective particles. Solid (or red) line is for pixel readout and dashed (or blue) lines are for strip readout [1].

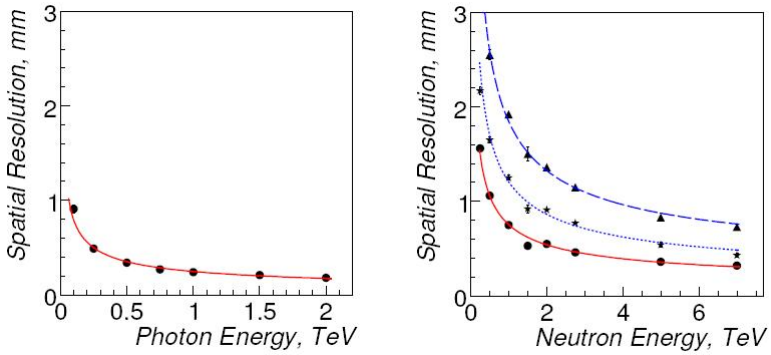

Figure 2.8: ZDC spatial resolution for photons (a) and neutrons (b) as a function of energy of the respective particles. Solid (or red) lines are for electromagnetic ZDC module, dotted line is for hadronic module with fine granularity (one rod per pixel), and dashed line is for hadronic module with coarse granularity (four rods per pixel) [1].

2.4.3 Kinematic Acceptance

The acceptance for several particle types as a function of x_f, P_T, and $|\eta|$ is displayed in Fig. 2.12. The acceptance of Λ_S and Δ_S is similar to that of π^0s. The K_S distributions are quite different from the latter since they involve detection of four gammas as well as decay in flight of the K_S.

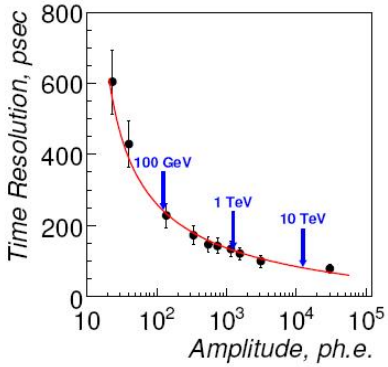

Figure 2.9: ZDC time resolution as a function of number of photoelectrons. Resolution for various neutron energies are shown [1].

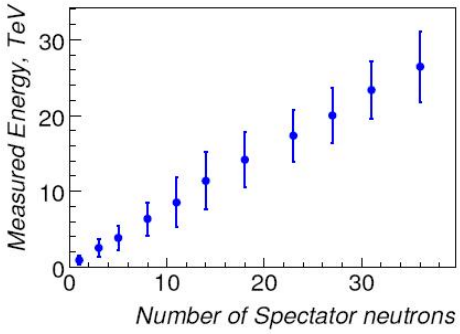

Figure 2.10: Energy measured by a $33cm^2$ area centered on the spectator neutron cluster vs. the known number of spectator neutrons in the cluster. Error bars correspond to the rms of measured energy fluctuations. See text for details [1].

2.4.4 Background

Fig. 2.13 and Fig. 2.14 displays the numbers of neutrons and photons per energy bin as a function of energy for each 7 TeV on 7 TeV pp interaction, respectively (note: bin size varies from histogram to histogram). This is shown for several energy ranges of the particles. The color code for these distributions is: red for particles in the ZDC coming from walls of limiting apertures, green for particles coming from decay in flight products, and blue are particles directly from the IP. Also shown in these plots is the average number of the respective particle , $\langle N \rangle$, and the total

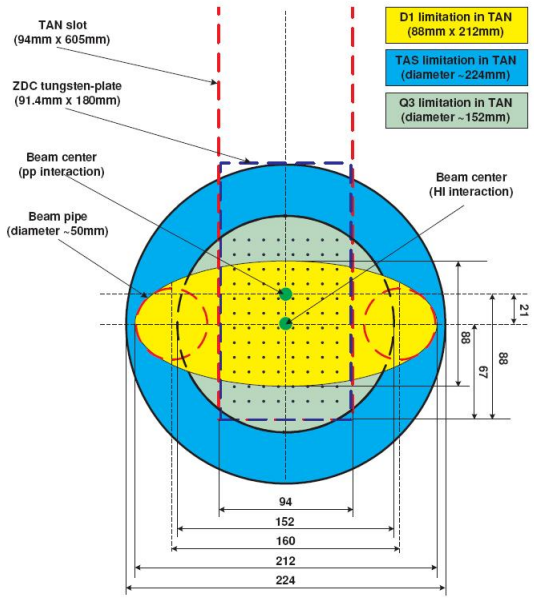

Figure 2.11: Geometrical acceptance of the ZDC at 140 m from the IP. Limiting apertures from upstream elements are projected to the 140 m point and displayed. The horizontal 94 mm by vertical 88 mm region in the center of the Figure is the geometrically unobscured region of the ZDC [1].

energy, Etot, of those particles to impinge on the ZDC per pp interaction. It is possible to observe that all the neutrons hitting the ZDC with an energy above 1 TeV are essentially all coming from the IP. Similarly, all photons above 60 GeV are essentially originating at the IP. Those are our signal particles. The only other particles with such high energies are products of particles which decay in flight.

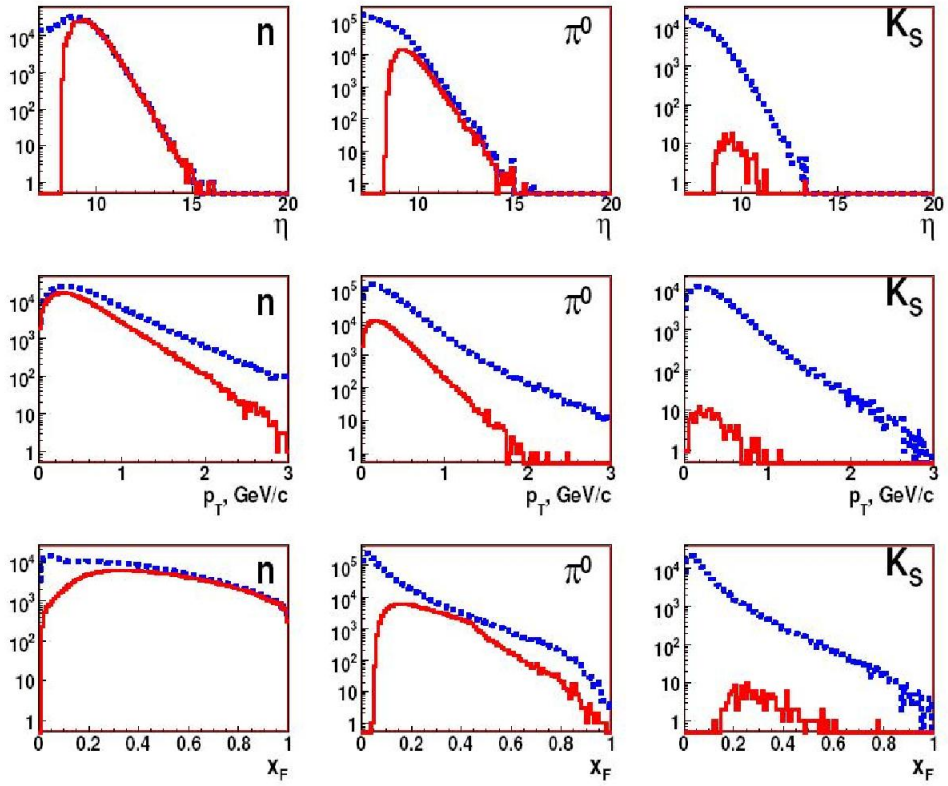

Figure 2.12: Acceptance of a ZDC for n, π^0 and K_S as a function of $|\eta|$, P_T, and x_f. In each distribution the top (Blue) curve is the number of generated events by Pythia, and the bottom (Red) is the number accepted [1].

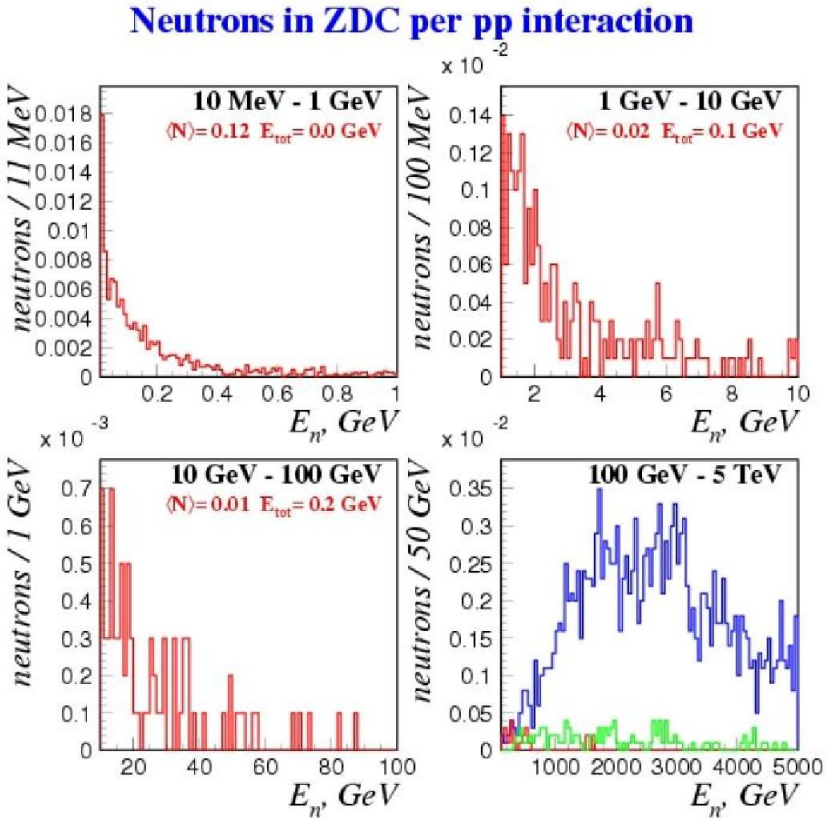

Figure 2.13: Numbers of neutrons per energy bin impinging on the ZDC as a function of energy for each pp interaction. Note: the size of energy bins varies between histograms. $\langle N \rangle$ and P_{tot} are for neutron energy ranges within the limits of the respective histograms. See text for details [1].

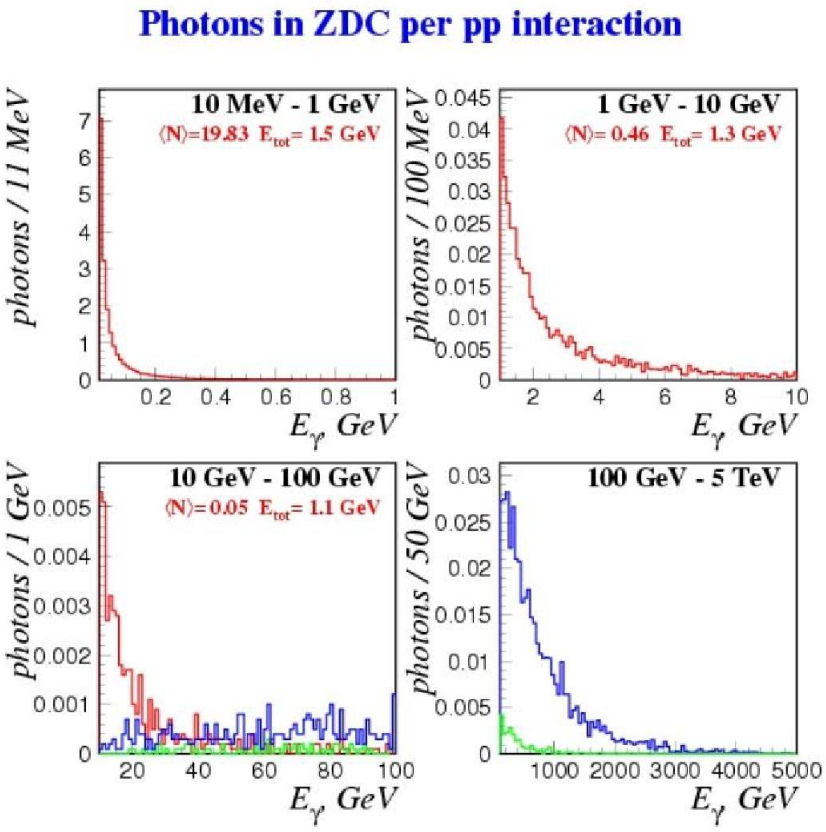

Figure 2.14: Numbers of photons per energy bin impinging on the ZDC as a function of energy for each pp interaction. Note: the size of energy bins varies between histograms. $\langle N \rangle$ and P_{tot} are for photon energy ranges within the limits of the respective histograms. See text for details [1].

Chapter 3

Analysis

This chapter will describe the ZDC performance in pp collisions at $\sqrt{s} = 7$ TeV, focusing on the analysis for the measurement of the energy ditribution of forward photons.
A sample of low luminosity (around $1.5 \cdot 10^{30}$ cm^{-2}s^{-1}) runs taken in March 2011 are selected for this analysis.
The procedure and the approximations that are needed for the π^0 reconstruction, because of the characteristics of the ZDC, will be outlined. The π^0 invariant mass peak will be used to extract the parameters for the calibration of the EM calorimeter. The results will be compared with simulated detector response through single particle MonteCarlo simulation.

3.1 Data sample

For the analysis of the single photon energy distribution we will use a subset of data taken by ATLAS during 2011 run at $\sqrt{s} = 7$ TeV. One requirements is to use low-luminosity and low pile-up runs, in order to minimize pile-up effects.
The analysis focuses on data taken in the first half of 2011. The ZDC suffered from radiation damage, degradating its performance during the whole 2011 run, introducing non linear effects in the detector response that makes the energy calibration for the second part of the year more challenging.
For all these reasons, 4 runs at 7 TeV center of mass energy have been chosen.
In Tab. 3.1 all used runs at 7 TeV chosen for analysis are listed. The average multiplicity (μ), for 7 TeV runs is around 3.
The total integrated luminosity for the set of selected runs is 90.25 nb^{-1}. Considering the prescale of the ZDC trigger used in this analysis, the total integrated luminosity will be 23.29 mb^{-1}.

Runs	Peak Luminosity	Peak μ	Stable beams	Prescale	Date
177531	$1.3 \cdot 10^{30}$ cm$^{-2}s^{-1}$	2.78	27.38 nb^{-1}	3740000	14/03/2011
177540	$1.8 \cdot 10^{30}$ cm$^{-2}s^{-1}$	3.77	26.91 nb^{-1}	3740000	14/03/2011
177593	$1.6 \cdot 10^{30}$ cm$^{-2}s^{-1}$	3.33	15.09 nb^{-1}	3740000	14/03/2011
177682	$1.5 \cdot 10^{30}$ cm$^{-2}s^{-1}$	3.12	28.26 nb^{-1}	3740000	16/03/2011

Table 3.1: Runs at 7 TeV chosen for analysis.

3.2 Detector alignment

When a particle hits the ZDC, a certain amount of energy is released on one or more than one pixels, that falls within the region of development of the electromagnetic or hadronic showers. Different pixels may receive different amounts of energy, as a function of their position with respect to the central point where the particle hits the detector. For the determination of the particle impact point, we calculate the averaged x and y coordinates distributions relative to the energy deposited on all pixels for each event. These averaged values have been calculated weighting the pixel position with the energy deposited on it, that is with the relative value expressed in ADC channels:

$$\bar{x} = \frac{\sum x_i ADC_i}{\sum ADC_i} \tag{3.1}$$

$$\bar{y} = \frac{\sum y_i ADC_i}{\sum ADC_i} \tag{3.2}$$

where x_i and y_i are the single pixel coordinates and are different for the EM and Hadronic modules (see Fig. 2.3). In Fig. 3.1 we show the result of the reconstructed shower centroid after the EM module alignment, obtained using the Run 177682. Watching the Fig. 3.1 we can appreciate the alignment of the x coordinate of ZDC with EM and hadronic particles arriving to ZDC from the interaction point along the beam pipe, as the mean value for the x coordinate is equal to 0. Instead for what concerns the y coordinate, result was obtained after the correction of a little misalignment (about 0.5 cm).
The multiple peaks present in both figures are due to the pixel discrete distribution on the EM module.
Fig. 3.2 shows the cross section of the particle shower hitting the EM module, where the origin corresponds to the center of the detector, located on the beam axis.

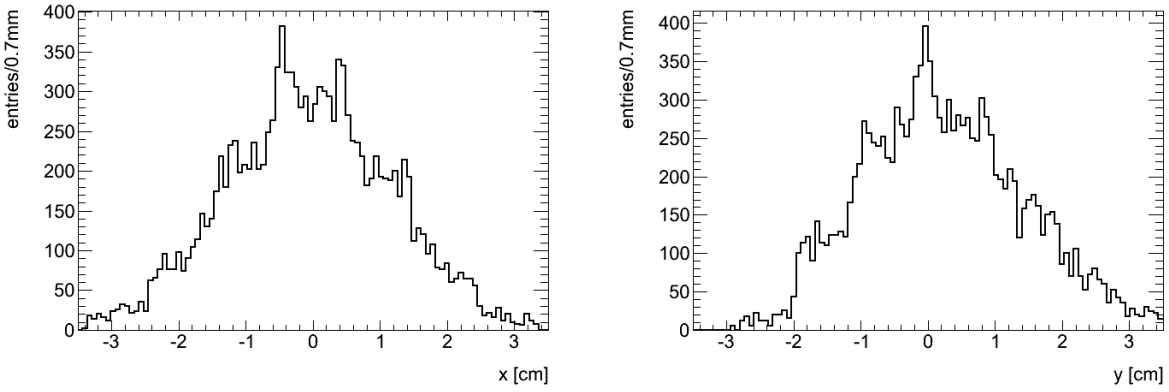

(a) (b)

Figure 3.1: x (a) and y (b) coordinates distribution of the energy centroid reconstructed using the pixels of the EM module, taken from Run 177682 with 7 TeV of center of mass energy.

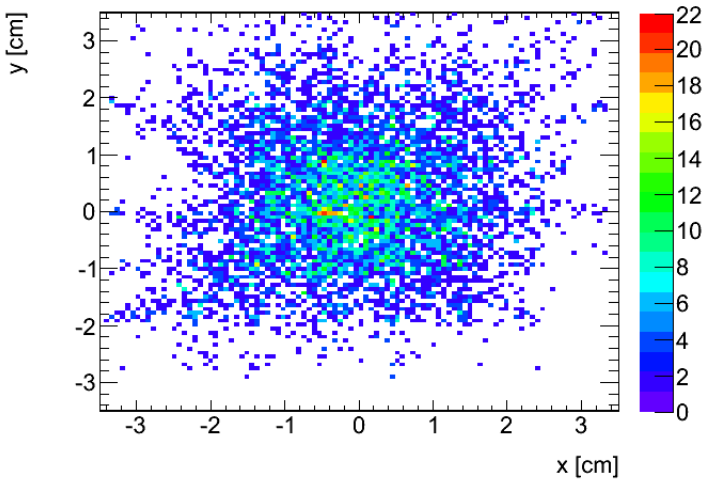

Figure 3.2: Profile of the particle shower hitting the EM module of ZDC, where x and y are the coordinates with respect to the point of intersection of the ZDC with the beam axis. The different colors are function of the density of particles that deposit energy in the detector as it is shown in the color scale. Results have been obtained from Run 177682 at 7 TeV of center of mass energy.

3.3 Clusters and impact position measurement

In order to determine the impact position of particles on the ZDC, clusters have been constructed using the pixels signal. Pixels in the EM module form a

8x8 square array with 1 cm pitch and they are used to reconstruct the position of the EM shower. Fig. 3.3 shows the distribution of the energy collected by the EM pixels. Pixels signals are considered if they exceed a particular threshold of 10 ADC counts in order to remove the contribution of electronic noise.
In Fig. 3.4 there is the number of activated pixel in the EM module for events taken by Run 177682 at 7 TeV of center of mass energy.

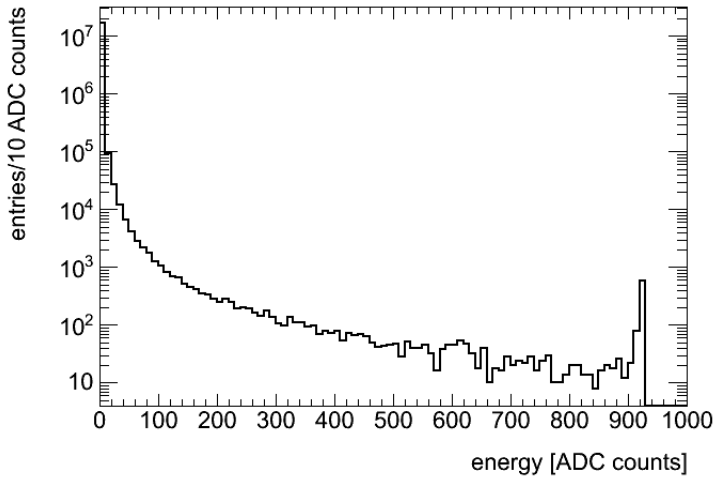

Figure 3.3: Distribution of uncalibrated signal amplitude collected by the EM pixels in events taken from Run 177682.

For clusters definition, the algorithm starts looking for the pixel with the highest uncalibrated signal, this is taken as a seed to form the cluster. All pixels around the seed in a 3×3 array with signal above the threshold are included in the cluster. Fig. 3.5 shows the distribution of the number of pixels forming the most energetic cluster in Run 177682 at 7 TeV. It is possible to observe that almost all clusters are composed by 1 to 4 pixels, in agreement with a transverse size of the shower of the order of the centimeter, expected for the tungsten.
The cluster coordinates (x and y) are obtained calculating the weighted average (see Eq. 3.1) using all the pixels in the cluster. At this point a cluster has been produced and completely studied.
The algorithm then starts from the beginning removing all the pixels already included in a cluster and this process is repeated till no more clusters are found.

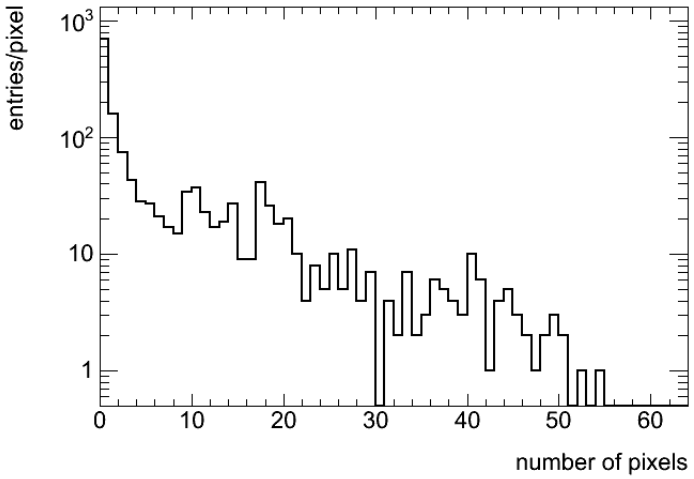

Figure 3.4: Number of pixels of the EM module with an energy higher than the threshold per event from Run 177682 at 7 TeV of center of mass energy.

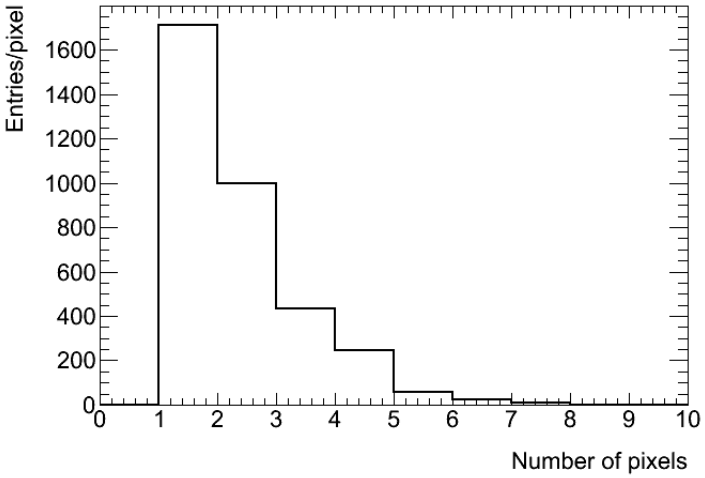

Figure 3.5: Distribution of the number of pixel in the most energetic cluster from Run 177682 at $\sqrt{s} = 7$ TeV.

3.4 Energy measurement from pixel read-out

For what concerns the energy of each particle shower, it is not correct to sum all the energy related to all the pixels included in the same cluster, as pixels cover just a little area with respect to the whole surface. In Fig. 3.6 we have a demonstration

of this, where we find the ratio between the signal by the full module read-out (see Chapter 2.1) and the sum of the pixel signals.

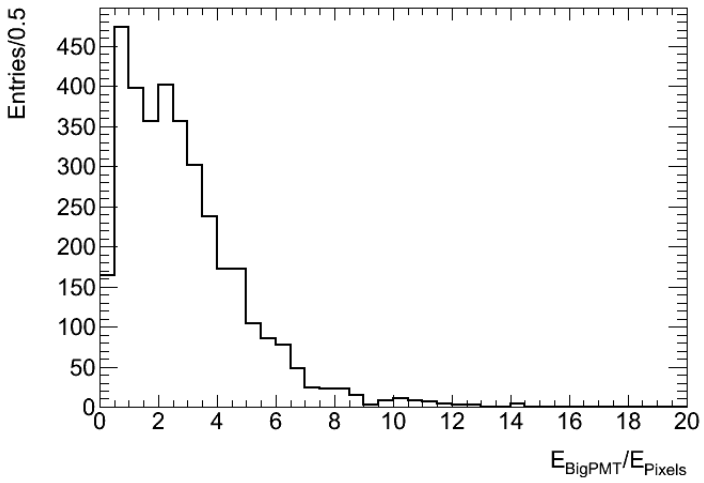

Figure 3.6: Ratio between the energy collected by the EM full module read-out and the sum of all pixels for the Run 177682 at 7 TeV of center of mass energy.

The only possibility to perform an energy measurement with the ZDC is to consider the signal coming from the full module read-out. In this case we know the sum of energy deposited by all particles in the same event, but it is not possible to reconstruct the energy of each single cluster. This is a key point in the ZDC design that will have effects on the π^0 reconstruction, as it will be shown in the next section.

3.5 π^0 reconstruction technic for total EM energy calibration

EM showers are limited to the first module of the calorimeter (EM module). The energy calibration of the module will be obtained through the rconstruction of the $\pi^0 \to \gamma\gamma$ invariant mass peak. As we saw in previous chapters, every time a particle hits ZDC, a certain amount of "Cherenkov light" reaches the PMT on the top of the module and it is converted into an electric signal. The analog signal is sampled and digitized to extract the signal amplitude (usually expressed in ADC counts of the peak of the signal waveform). To calibrate the ADC counts in term of energy of the EM shower, the invariant mass of the $\pi^0 \to \gamma\gamma$ where both protons are reconstructed in the ZDC has been used.

In order to reconstruct $\pi^0 \to \gamma\gamma$ we need to know the amount of energy that has been deposited and the γ positions. For the first quantity we use the total signal given by the full module read-out (see 2.1). For the second one, the pixels (see 2.1) are used to determine the exact position of the point where the energy has been released, with a read-out pitch of 1 cm.
For the π^0 reconstruction we selected events with exactly 2 reconstructed clusters in the EM module. As it has been mentioned in section 3.4, it is not possible to separately measure the energy of the 2 clusters, therefore we can assume for the π^0 reconstruction that the 2 cluster have the same energy which is exactly half of the total energy. This assumption will obviously have an effect on the π^0 invariant mass resolution, as it will be shown by MC simulation. As we saw in detail for pixels, also for the full module read-out the raw signal is expressed in ADC channels of the waveform peak. As for each calorimeter there are an EM module and 3 Had. modules, we have 4 full module read-out PMTs. The energy collected by these 4 module is shown in Fig. 3.7. At the end of scale (around 900 ADC counts), corresponding to the higher energies, we notice a peak due by a saturation of the detector. In these examples, as HG signals (see chapter 2.2.2) are plotted we reach maximum values of energy detectable by ZDC. On the other hand, LG signals do not show the same problem and can be used to analyze high energy depositions. In this analysis the HG signal is preferred in order to exploit the better energy resolution.
Hadrons (mainly neutrons) in the ZDC produce hadronic showers that are not limited to the first module but have longitudinal development in all the 4 modules. Therefore, to select events with only photons in the ZDC we apply cuts to remove events presenting signals in the hadronic modules.
In order to remove the noise contribution, a threshold of 50 ADC counts has been chosen for the EM module: only all the signal higher than this threshold has been included in the analysis. For the rejection of events with hadrons participating to the signal, a cut of 20 ADC counts has been put to the 3 Hadronic modules: events with all the signal lower than this value has been selected, as particles like neutrons release a bigger amount of energy in Hadronic calorimeters.
The π^0 mass has been calculated by adopting some approximations to express all these quantity in terms of variable detectable by ZDC, applied to the usual invariant mass formula:

$$m_{\pi^0} = \sqrt{E_{TOT}^2 - P_x^2 - P_y^2 - P_z^2} \tag{3.3}$$

where E_{TOT} is the energy of the π^0, that is the sum of energy of the 2 photons $E_1 + E_2$.
P_x, P_y and P_z are the 3 components of the total momentum of π^0,also in this case, they represent not only the π^0 but also the sum of the 2 photons.

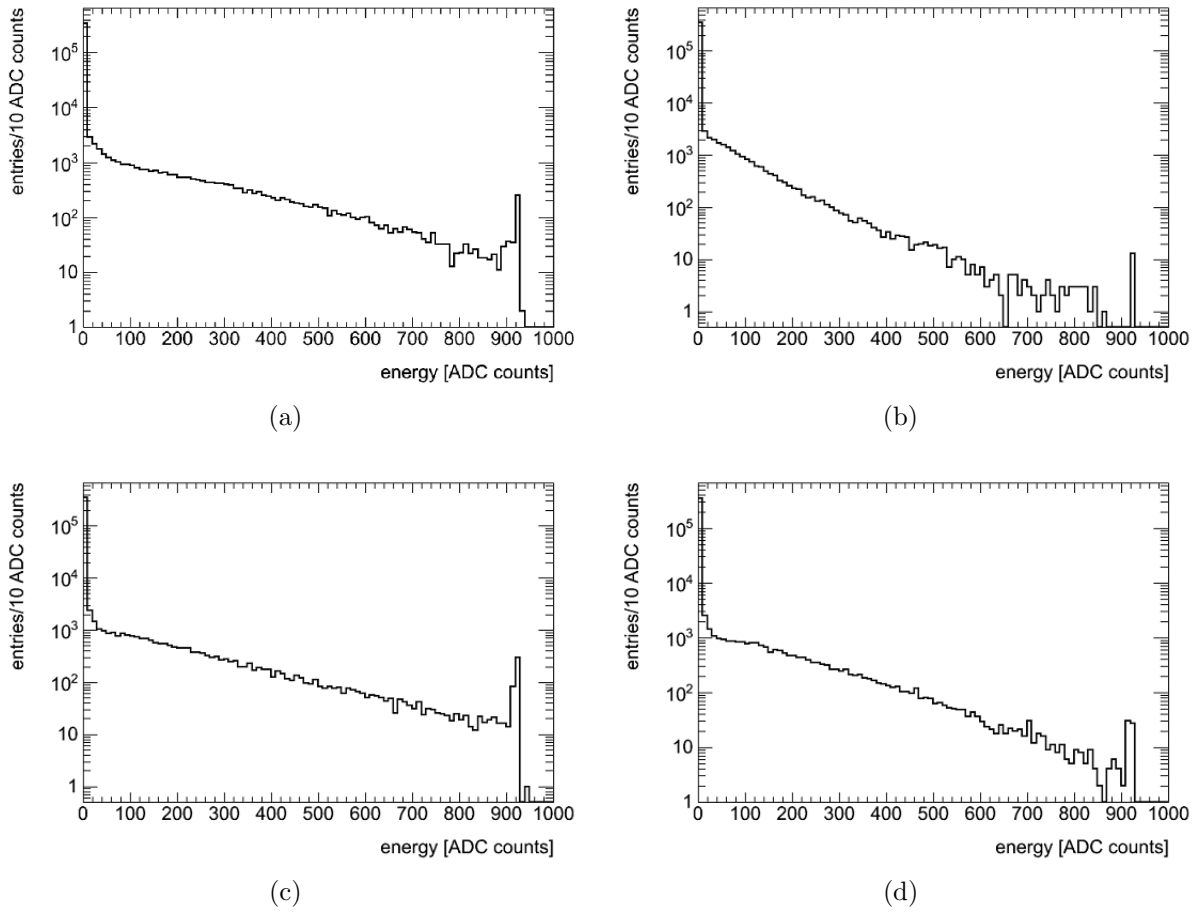

Figure 3.7: Raw energy signal distributions expressed in ADC counts, from the EM module (a), the first Hadronic module (b), the second Hadronic module (c) and the third Hadronic module (d) during the Run 177682 at 7 TeV of center of mass energy.

We can start with the photon positions x and y, which correspond to the clusters position information. The z coordinate is fixed by the detector position at 14110 cm from the interaction point. For what concern their energy, as it was mentioned before, we assigned to each cluster half of the total energy collected by the EM module.
It is possible to calculate the distance of the photon impact position in ZDC in the ATLAS reference frame, with respect to the origin determined by the interaction point:

$$r_i = \sqrt{x_i^2 + y_i^2 + z^2} \tag{3.4}$$

where $i = 1, 2$ is the photon index. This quantity will be useful to obtain the different projection of momenta of the 2 photons.
From Relativity we know that a massless particle has a momentum equal to its enrgy:

$$E = p \tag{3.5}$$

The EM module provides the information on the total energy deposited by the 2 photons. For the π^0 reconstruction we will make the assumption that the total energy is equally shared between the 2 photons:

$$E_1 = E_2 = \frac{E_{TOT}}{2} \tag{3.6}$$

This assumption is appropriate for the observation of the π^0 invariant mass peak for the purpose of the detector energy calibration, as it will be shown later using a full detector simulation. Within this approach we can write:

$$P_x = E_1 \cdot \frac{x_1}{r_1} + E_2 \cdot \frac{x_2}{r_2} \tag{3.7}$$

$$P_y = E_1 \cdot \frac{y_1}{r_1} + E_2 \cdot \frac{y_2}{r_2} \tag{3.8}$$

$$P_z = E_1 \cdot \frac{z}{r_1} + E_2 \cdot \frac{z}{r_2} \tag{3.9}$$

that are the π^0 energy and momenta expressed in terms of measured quantities and they can be used to calculate the π^0 mass.

3.6 π^0 mass results

Applying all the equations in the previous section to all the selected runs (Tab. 3.1), it is possible to obtain the distribution of the pion mass for pp collisions at $\sqrt{s} = 7$ TeV (Fig. 3.8). It is evident how the mass distributions are approximately the same for the different runs.
We expressed the mass distributions in arbitrary units, as at this phase the detector is not calibrated yet, and results have been obtained by the original signal expressed in ADC counts.
In all the figures we can see the whole distribution made of 2 main contributions: the main peak which mostly represents the π^0 signal superimposed to a broader distribution, which is mainly due to background.
In previous section we mentioned that in the cluster reconstruction we adopted a threshold for pixels that was fixed to 10 ADC channels. We verified the effect in the π^0 reconstruction of the variation of this threshold. At lower values, the π^0

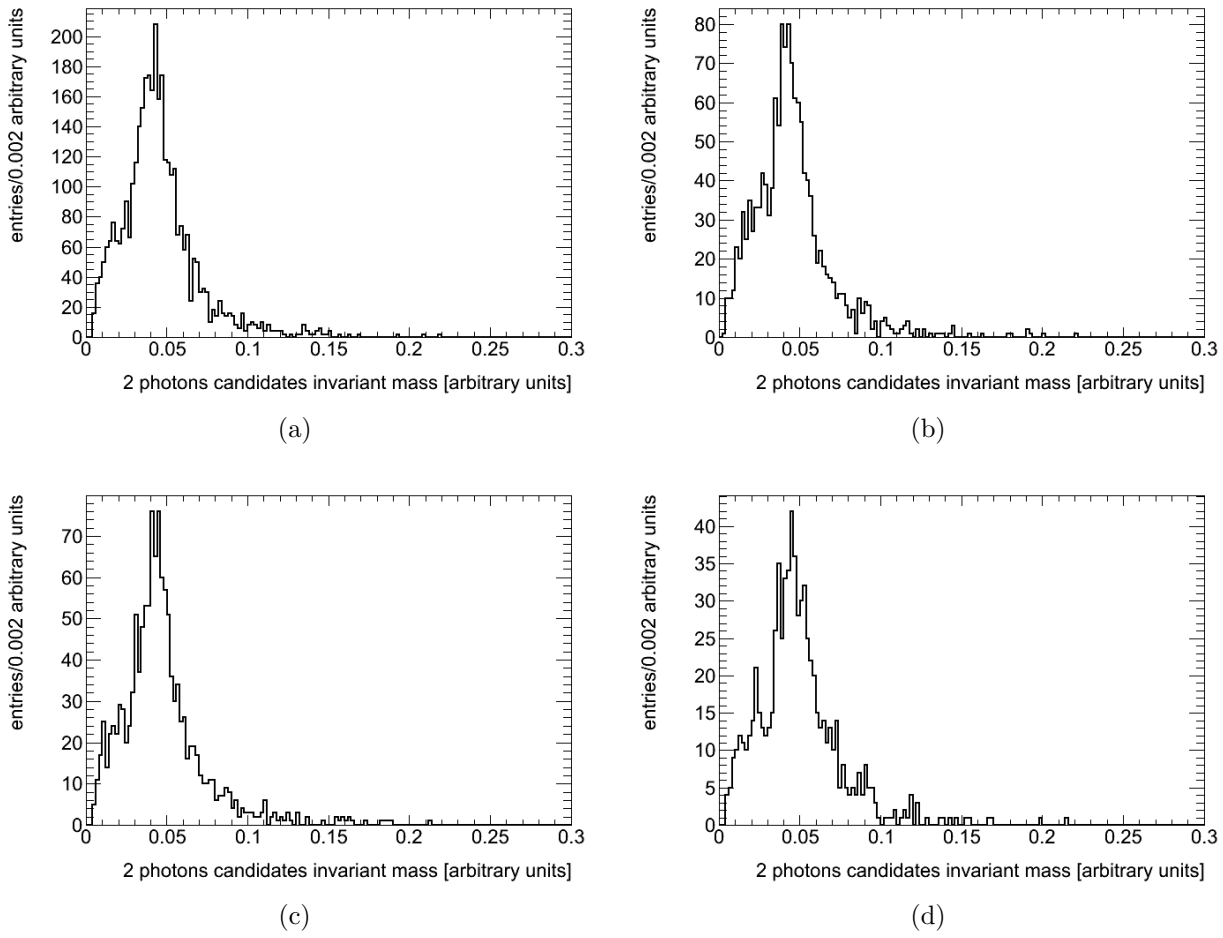

Figure 3.8: The preliminary uncalibrated mass distribution of reconstructed π^0 candidates in ZDC-C in pp collisions at $\sqrt{s} = 7$ TeV for Run 177531 (a), 177540 (b), 177591 (c) and 177682 (d).

invariant mass peak is not longer evident, as background became not negligible with respect to the signal. So some attempt has been made: at 15 and 20 ADC channels. Results are shown in Fig. 3.9.
From these 2 plots we can argue that threshold at 10 ADC counts is appropriate for the cluster reconstruction. In fact the 2 results are similar to the ones obtained using 10 ADC channels threshold, as their mean values and σ values are almost the same for all the 3 cases.
The only difference is that increasing the threshold for cluster reduces the background at the left of signal, at the price of a reduced number of π^0 signal events.
We are dealing with photons producing EM showers in the detector. Then in order

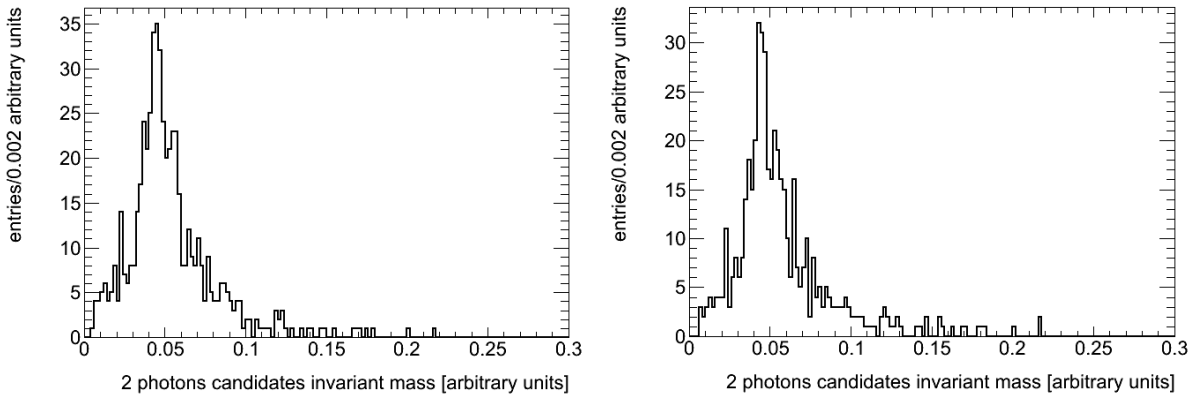

(a) (b)

Figure 3.9: The uncalibrated mass distribution of reconstructed π^0 candidates in ZDC-C in pp collisions at $\sqrt{s} = 7$ TeV for Run 177531 (a) with a threshold for clusters at 15 ADC channels. and at 20 ADC channels (b).

to extrapolate their energy we are using information from the EM module only. The effect of possible leakages in the first Hadronic module has been considered. This effect has been checked including the hadronic module in the π^0 mass calculation. This means that E_{TOT} is now the total energy of the EM module summed to the energy coming from the hadronic one and excluding all events with some energy deposition in the other 2 hadronic modules, maintaining relative cuts already described for the standard π^0 reconstruction. In Fig. 3.10 we can see a comparison between the results with this new assumption and the results with the standard method.
These 2 plots are very similar. In fact we have similar mean values (around 0.043 for both cases) and similar σ values (0.009 for the case with the only EM module and 0.011 for the sum of the EM and the first hadronic module). Also the shape of signal is consistent with what we already obtained, in this new procedure.
We can derive that the contribution from the hadronic module is negligible respect the energy coming from the EM one. This is confirmed also by the direct comparison between the amount of energy coming from the 2 modules (see Fig. 3.11). That amount of energy in the first hadronic is generally less than 1/30 of the energy in the EM module. For this reason we chose to use only the EM module for the measurement of EM showers.

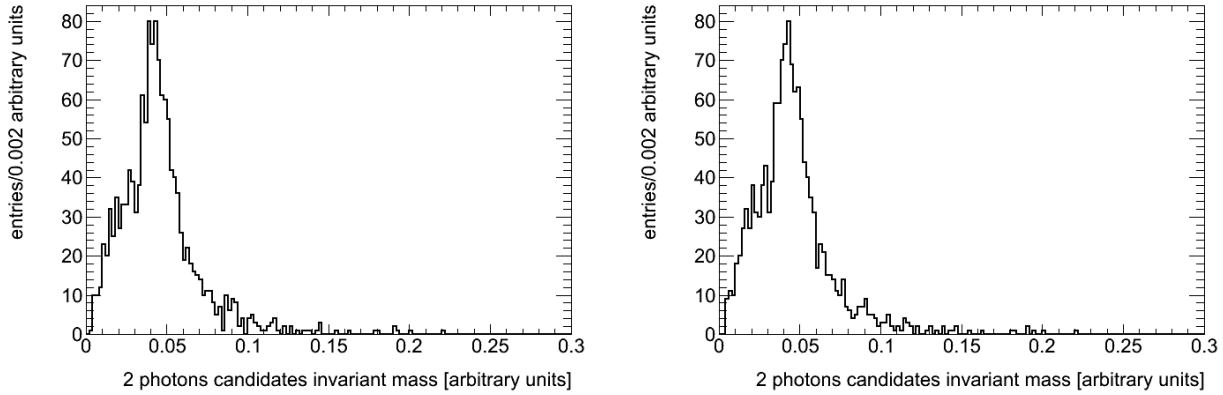

(a) (b)

Figure 3.10: The preliminary mass distribution of reconstructed π^0 candidates in ZDC-C in pp collisions at $\sqrt{s} = 7$ TeV for Run 177531 with energy coming only from the EM module (a) and with energy coming from the sum of the EM and the first hadronic modules (b).

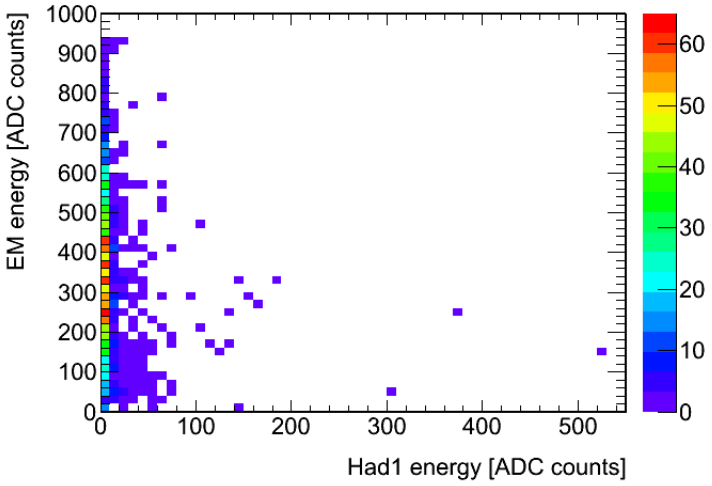

Figure 3.11: Comparison between the total amount of energy per event coming from the entire EM and from the entire hadronic module.

3.7 π^0 mass fit

In order to obtain the energy calibration of EM showers, we need to fit the entire π^0 invariant mass distribution, discriminating between π^0 signal and the

background, and to extract the fit parameters, to obtain the mean value for π^0 invariant mass peak.
Several attempts has been made in order to find the best equation representing the signal. We will now give a description of the invariant mass fit technique.
The π^0 invariant mass peak position must be extracted to obtain the detector calibration constant for the measurement of the EM shower energy. The main π^0 peak is modeled with a gaussian distribution, the background around the main peak has been modeled using a third degree polynomial. Other functions have been tested for the background model but the detector calibration has shown to be independent from the background shape.
Results for all the 4 selected runs are shown in Fig. 3.12.
The fit parameters are listed in Tab. 3.2.
We can see from the table how the values of Peak are all around 0.045. Also the

Runs	Peak	σ	K [GeV/ADC]
177531	0.044	0.009	3.07
177540	0.044	0.008	3.07
177593	0.047	0.008	2.87
177682	0.043	0.010	3.14

Table 3.2: Fit parameters for the 4 Runs at 7 TeV.

σ values of the main gaussian peak are almost all the same and they are reported in Tab. 3.2.
Run 177593 shows a sensibly lower calibration constant with respect to the others 3 runs. This is due by the high voltage applied to the photomultiplier of the EM module. For all runs it was set to 1065 V, while during the 177593, the HV was increased to 1087 V (see Tab. 3.3).
We made some check in order to verify that these results are stable varying the

Runs	PMT HV [V]
177531	1065
177540	1065
177593	1087
177682	1065

Table 3.3: HV applied to the PMT of the EM module (ZDC-module C) for the 4 selected Runs at 7 TeV.

function which fits the background. So also a landau and a second degree polynomial curves has been used. In Fig. 3.13 results are shown.
In both cases the Peak value of the gaussian distribution does not vary, as it is

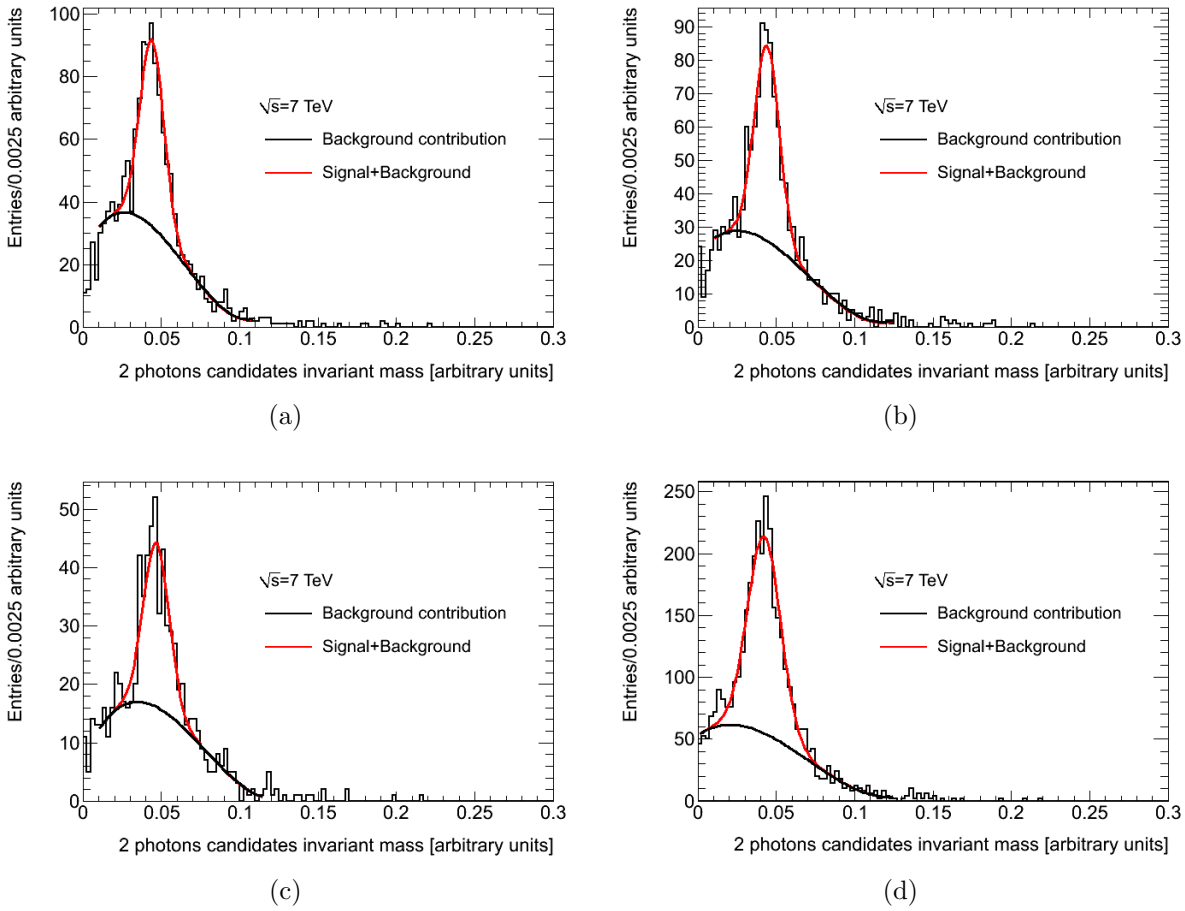

Figure 3.12: Uncalibrated invariant mass of π^0 candidates for pp collisions at 7 TeV in Run 177531 (a), 177540 (b), 177593 (c) and 177682 (d) reconstructed using the ZDC-C. The distribution is fitted using the sum of a gaussian distribution for the main π^0 peak and a third degree polynomial for the background events, whose contribution is shown by the black curve.

equal to around 0.04 as it was for the third degree polynomial case. The same can be said for the σ value which is around 0.01.
We can argue that the choice of the background shape does not affect the calibration procedure. Anyway, among all the selected functions, the third degree polynomial gives a better description of the background contribution.
When using a landau function, the χ^2 relative to the total fit is too high and several parts of the plot are not compatible with the fit.
Different attempts have been made in order to check the quality of the fit.
The first one has been to change the bin size. Different bin size of 4 and 5 ADC

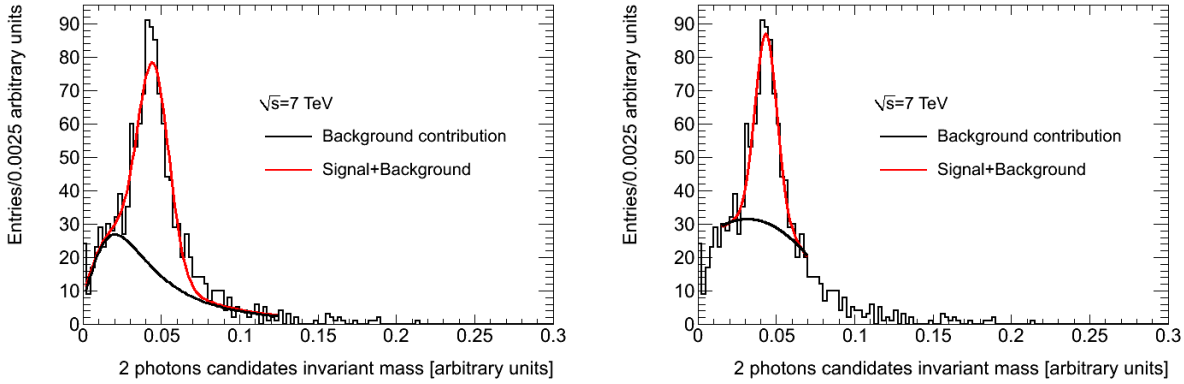

(a) (b)

Figure 3.13: Invariant mass of π^0 candidates for pp collisions at 7 TeV in Run 177540 reconstructed using the ZDC-C. The distribution is fitted using the sum of a gaussian distribution for the main π^0 peak and a landau one (a) and a second degree polynomial (b) for the background events, whose contribution is shown by the black curve.

counts have been tried. The second attempt regards the reduction of the domain of fit arriving to a range of mass comprised between 0 and 300 MeV, with a possible change of bin size.
With these changes we noticed a little improvement, as it was expected in the best case the σ value also decreased by 20%. For what concerns the χ^2 of the landau fit, values are approximately equal to 2, still too high for an acceptable fit. Moreover, while the sum gaussian+landau looks anyway well fitting the entire domain, the only landau seems still too low with respect to the expected background characterized by the local maximum value on the left of the signal shape.
For the second degree polynomial the same procedure has been followed. We also decided to fit not the entire domain but to concentrate ourself just on the signal region and a part of the background region, including its maximum value usually present on the left part of plots.
This solution fit looks appropriate in the restricted domain (Fig. 3.13b). The standard deviation is smaller than the previous solution and above all the whole fitting line seems to cover enough all the selected region. In particular, also the fit to background has been improved, as it covers now the maximum at left of signal. Anyway despite of all these improvements, an eventual extension of the fit to the rest of domain would not be satisfactory as it is now in a limited range. This can not be negligible as the selected region for fit has been very reduced and it partially involves the main part of background.

All these checks leaded us to a third degree polynomial equation to fit the background.
The σ value with this last solution is the best obtained till now, acceptable and compatible with the simulated data. The χ^2 is around 1.6. The fited region is significantly wider than the signal Peak region and it covers the important left part of the plot, where the main amount of background is concentrated.
This result has been also confirmed by the MonteCarlo analysis, that will be presented later in the following chapter.
Through the fit procedure, we have one mean value per run. In order to have take into account possible differences in the experimental setup we calculate for each run its calibration constant.
Calculating the ratio between each obtained mean value with the π^0 mass, that is 135 MeV, we obtin the calibration constants (see Tab. 3.2). Summing all the contributions of signal run by run, weighted with their own calibration constants, we can obtain a π^0 reconstructed mass relative to the whole collected statistics. The result is shown in Fig. 3.14.

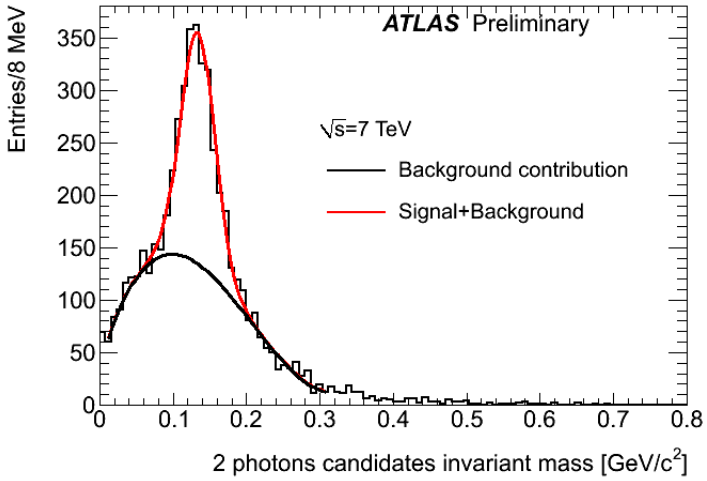

Figure 3.14: Invariant mass of π^0 candidates for pp collisions at 7 TeV, run n 177531, 177540, 177593 and 177682, reconstructed using the ZDC-C. The invariant mass resolution is found to be around 18%. The two photons are reconstructed as separate energy depositions on the first ZDC module (EM module). The distribution is fitted using the sum of a gaussian distribution for the main π^0 peak and a Polynomial of 3 degree distribution for the background events, whose contribution is shown by the black curve.

3.8 Features of single photon di-photon events

Events with EM showers only (EM events) can be selected by requiring signal only in the first (EM) ZDC module. Single photon or di-photon events can be classified using the number of reconstructed clusters in the EM pixels. The total energy of EM events can be obtained by applying the energy calibration constants to the module signal. Fig. 3.15 and 3.16 show respectively the reconstructed energy and the number of pixels per cluster of di-photon events.
The same di-photon selection used for π^0 reconstruction can be used for the energy measurement of di-photon events, the result is shown in Fig. 3.15.

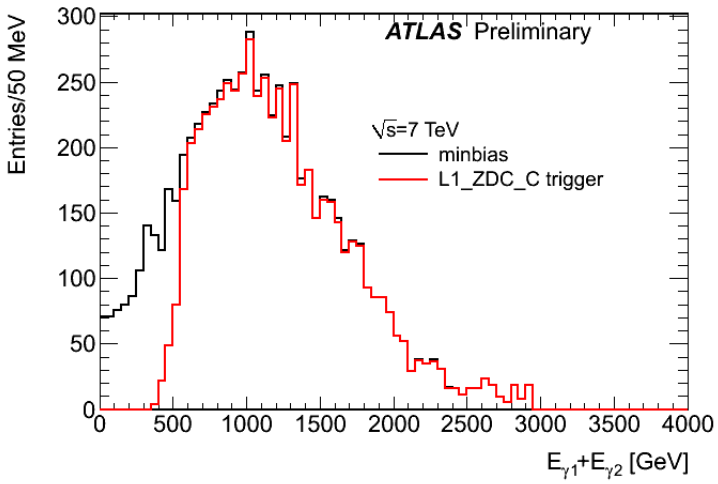

Figure 3.15: Energy distribution of di-photon candidates reconstructed in the ZDC-C for pp collisions at 7 TeV, Run 177531, 177540, 177593 and 177682. The black line represents all the data from the minbias stream while the red one after the ZDC trigger selection.

In Fig. 3.16 we notice, as it was expected from MC simulations for di-photon events, that there are more included pixels forming the first cluster which is the most energetic, than in the second one.
By using EM events with a single reconstructed cluster we can obtain the single photon energy distribution, which is shown in Fig. 3.17 for the 4 runs separately. We can notice a sharp peak at high energy (starting at around 2500 GeV) due to the saturation of the ADC signal in the high gain (HG) read-out chain. To avoid the saturation effect we will also consider the low gain (LG) read-out which have worse energy resolution but can measure higher energy values.
By design the ratio between HG and LG signal is around 10, to check the correct

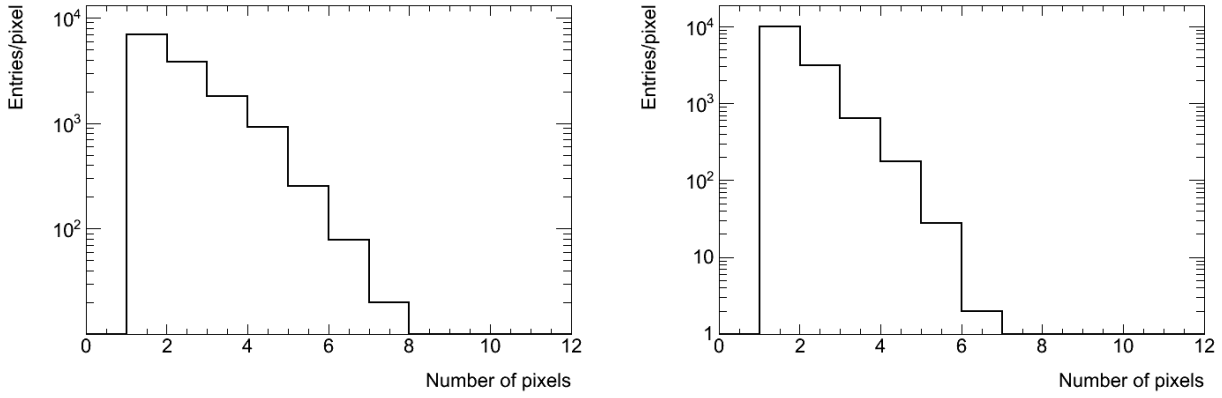

(a) (b)

Figure 3.16: Number of pixels included in the first (a) and second (cluster) for diphoton events in ZDC-C in pp collisions at $\sqrt{s} = 7$ TeV for Runs 177531, 177540, 177593 and 177682.

value for each run we can fit the main peak in the HG/LG ratio. The result is shown in Fig. 3.18 and the results are summarized in Tab. 3.4.

Using the HG/LG ratio we can obtain the calibration constant for the LG read-

Runs	HG/LG	K_{LG} [GeV/ADC]
177531	9.615	29.52
177540	9.843	30.22
177593	9.611	27.58
177682	9.602	30.15

Table 3.4: Ratio between the HG and LG energy collected by the first module in the ZDC-C HV and calibration constnt for the energy measurement in the LG read-out chain for the 4 Runs at 7 TeV.

out and obtain the single photon energy spectra without the saturation effect (Fig. 3.19), so it is possible to determine the correct position of the end point of the distribution.

Fig. 3.20 and 3.21 show the energy distribution of single photon candidates obtained from all the 4 runs (HG and LG) with again the relative number of pixel included in the single cluster in Fig. 3.22. Fig. 3.23 shows the impact position of the single photon candidate in the EM module.

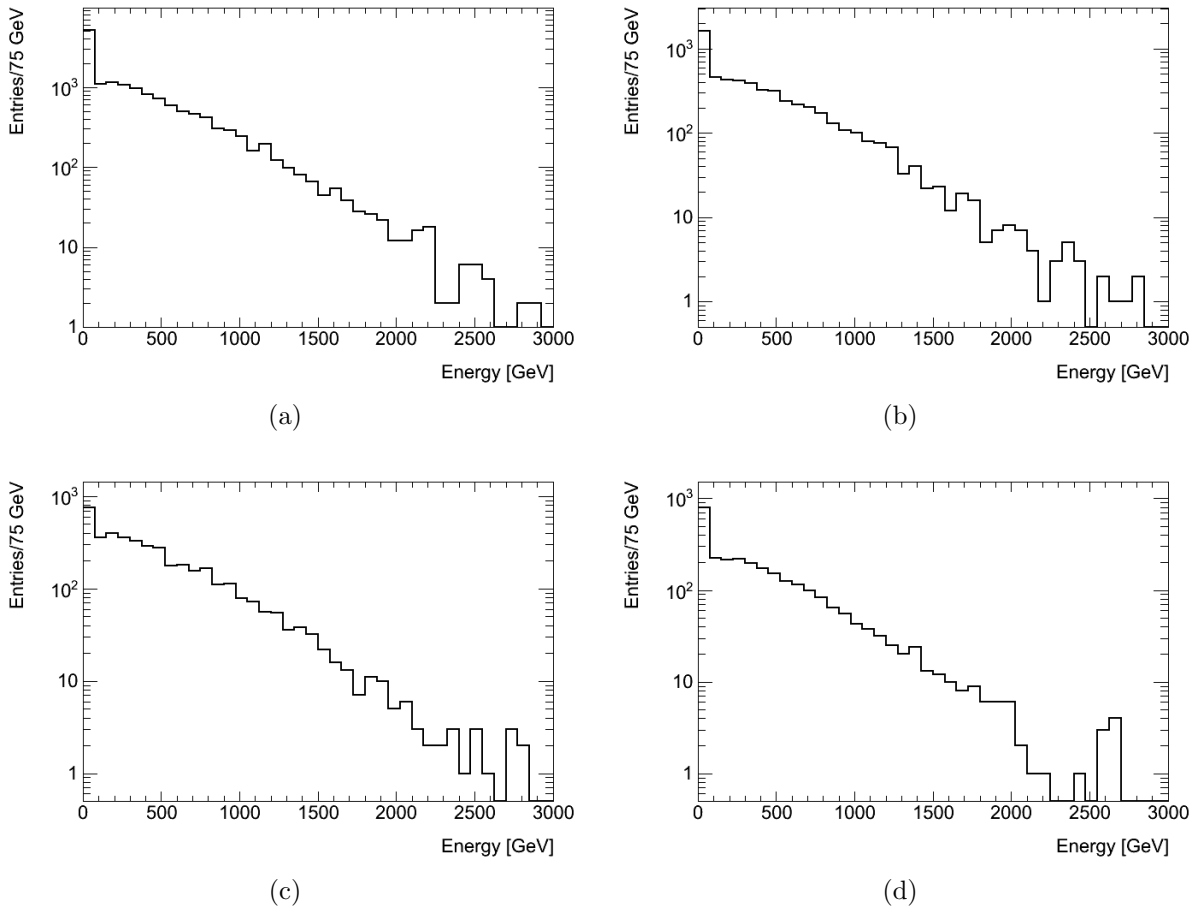

Figure 3.17: Energy distribution of single photon candidates reconstructed in the ZDC-C using the HG read-out for pp collisions at 7 TeV, Run 177531 (a), 177540 (b), 177593 (c) and 177682 (d). The curve represents all the data from the minbias stream.

In Fig. 3.21 the saturation effect is totally removed, but the rest of the distribution is pretty consistent with the HG case.
From Fig. 3.23 we can notice that a large fraction of photons reaching the ZDC are detected exactly along the p-p collision direction, impacting the detector in its center.

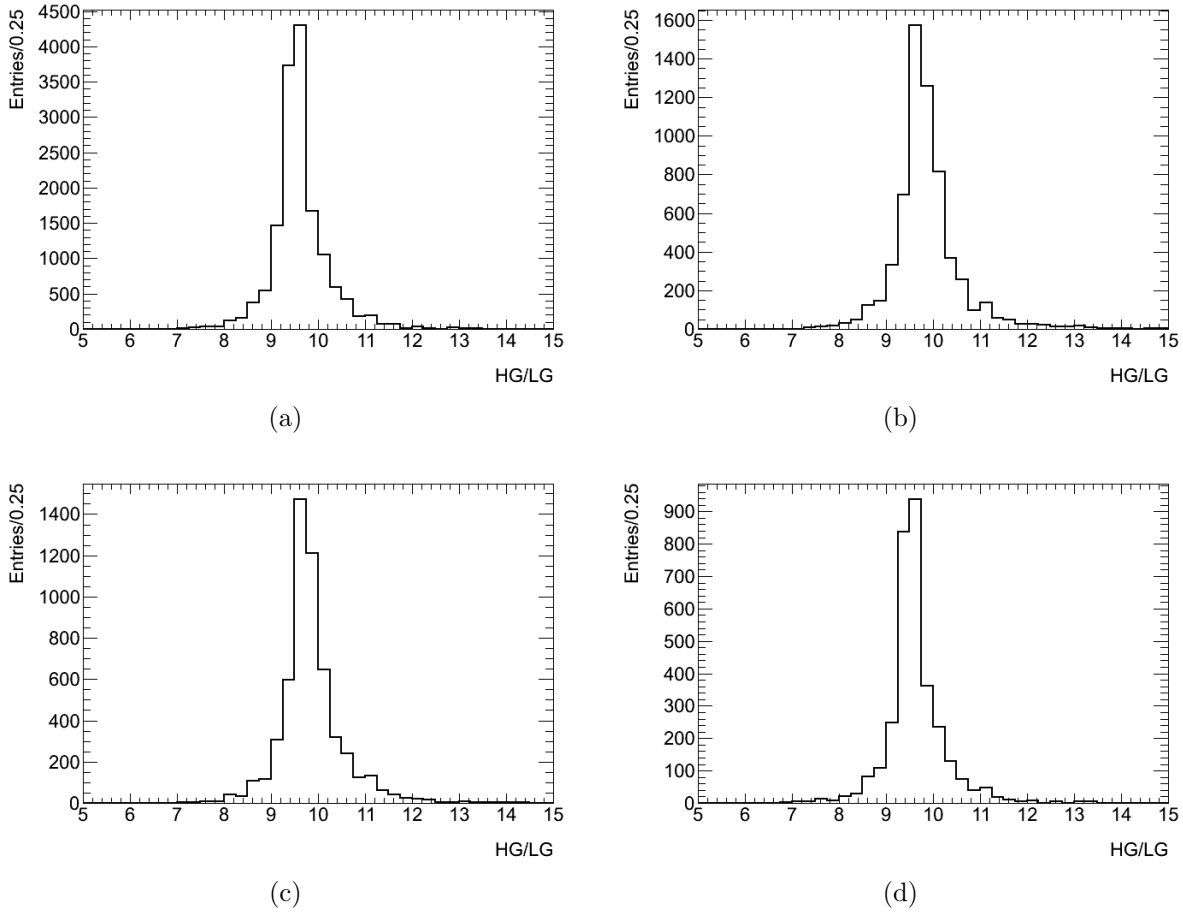

Figure 3.18: Ratio between the HG and LG energy collected by the first module in the ZDC-C for pp collisions at 7 TeV, Run 177531 (a), 177540 (b), 177593 (c) and 177682 (d). The curve represents all the data from the minbias stream.

3.9 Trigger efficiency

The ZDC trigger contains events in which the total (summed) signal of the 4 modules is above a fixed threshold. This threshold corresponds to about 600 GeV for EM events as it can be seen in Fig. 3.14 ,3.15 and 3.20. In our analysis we need to consider the energy region where the ZDC is fully efficient. We must point out that we are interested in EM events, so we will evaluate the trigger efficiency for events with no signal in the last 3 modules; for these events the signal from the EM module is the only contribution to the trigger signal. The ZDC trigger efficiency has been evaluated by using events from an independent trigger (MBTS).
The efficiency can be measured as the ratio between the number of events seen by

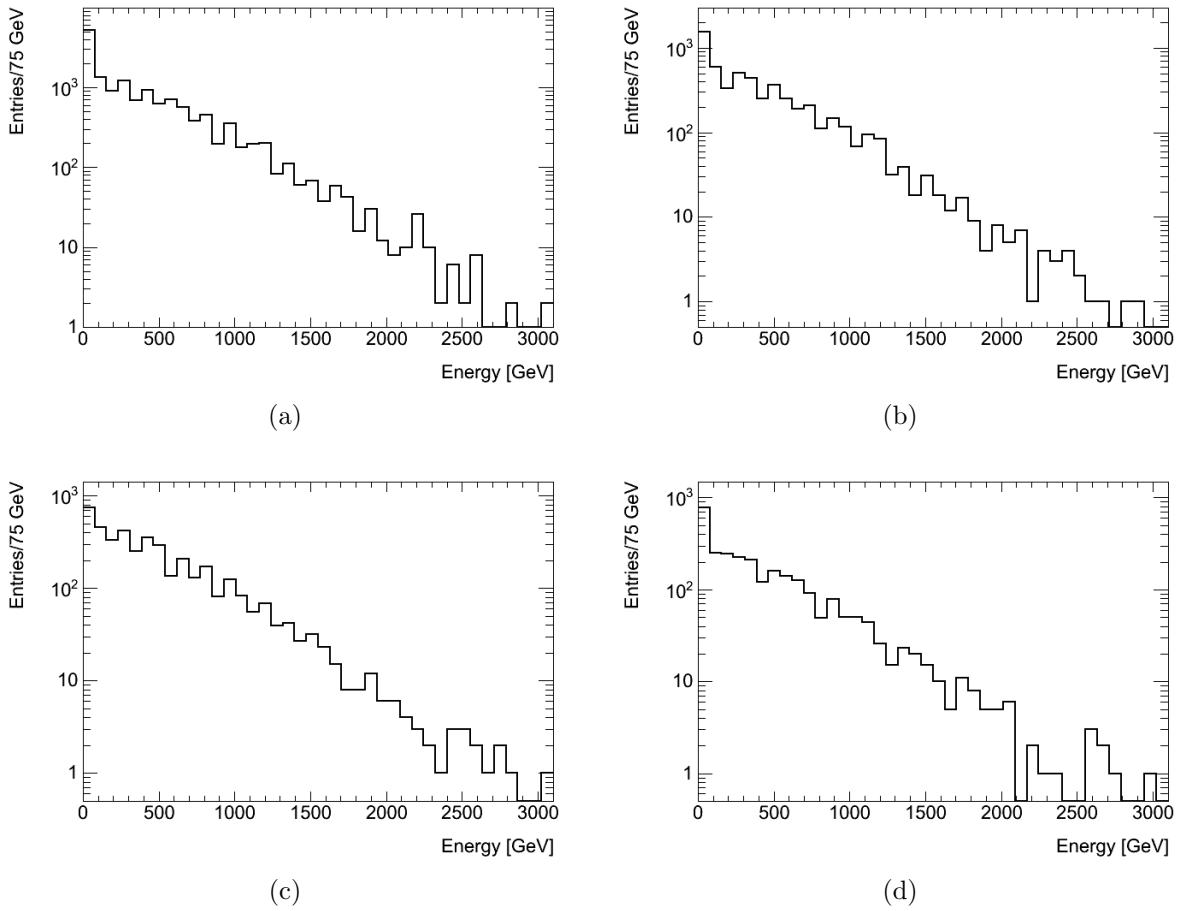

Figure 3.19: Energy distribution of single photon candidates obtained from the LG channel of the ZDC-C for pp collisions at 7 TeV, Run 177531 (a), 177540 (b), 177593 (c) and 177682 (d). The curve represents all the data from the minbias stream.

both ZDC and MBTS and the number of events seen only by MBTS, at a given ZDC measured energy:

$$\epsilon = \frac{N_{ZDC+MBTS}}{N_{MBTS}} \tag{3.10}$$

where with $N_{ZDC+MBTS}$ and N_{MBTS} we indicated respectively the number of events collected by both ZDC and MBTS and only by MBTS, respectively.
Obviously this parameter varies as a function of energy. We defined 10 ranges of energy where to calculate the efficiency, in the range 300 and 900 GeV, large approximately 100 GeV using 25 and 50 GeV steps around the trigger threshold and 100 GeV steps where the trigger is fully efficient. This choice has been done in

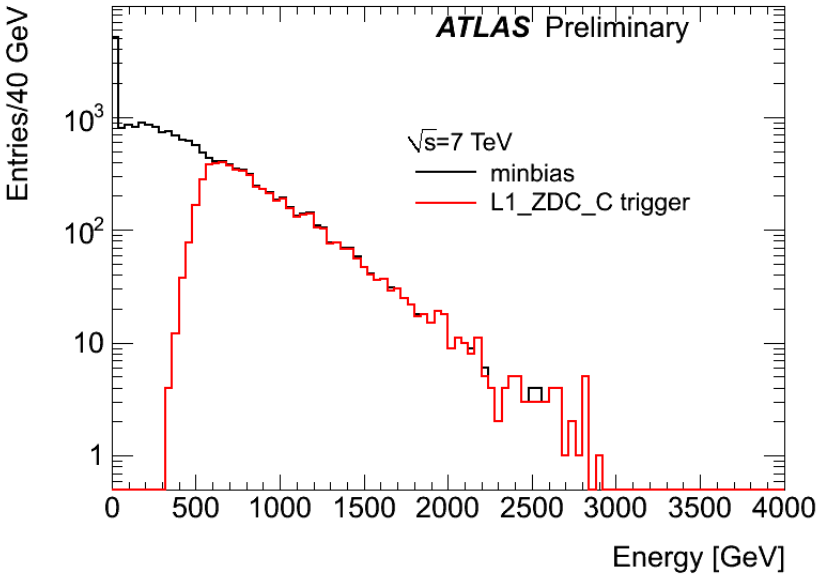

Figure 3.20: Energy distribution of single photon candidates reconstructed in the ZDC-C for pp collisions at 7 TeV, Run 177531, 177540, 177593 and 177682. Photon candidates are defined using the longitudinal shower development, by selecting events with energy deposition only in the first module. The energy scale is set using the π^0 mass peak. The black curve represents all the photon candidates in the MinBias stream, the red curve is for events triggered by ZDC-C.

order to have a better resolution in the part of the curve where the trigger becomes efficient, for a more precise evaluation of the threshold value.
We assigned the average value of the energy range to the relative value of efficiency in every interval of energy. The result is shown in Fig. 3.24.
In the following, for data-MC comparison, we will consider only the region where the ZDC is fully efficient, that is for events with total EM energy larger than 700 GeV.

3.10 Checks of the reconstruction technique with full detector simulation

The π^0 reconstruction technique used for data and the detector performance have been checked with a full detector simulation when only a single particle is directed to the ZDC (single particle MC generator).

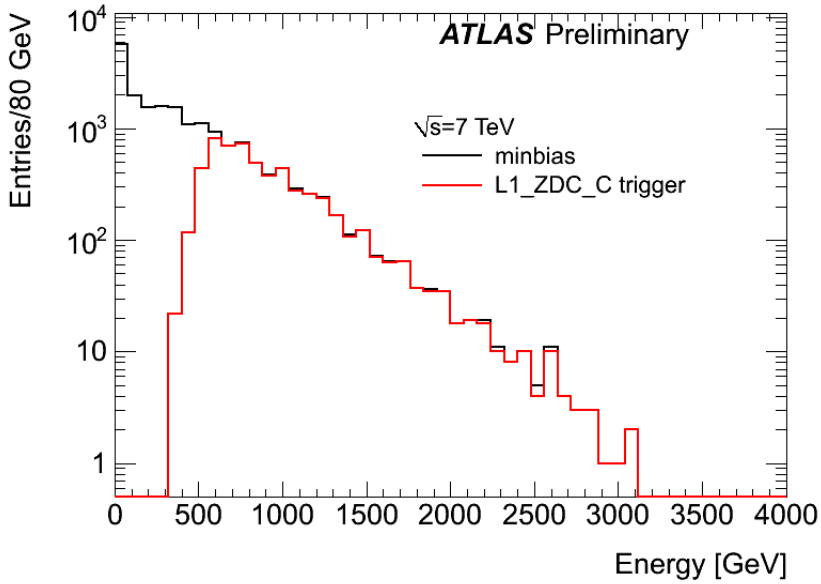

Figure 3.21: Energy distribution of single photon candidates reconstructed in the ZDC-C for pp collisions at 7 TeV, Run 177531, 177540, 177593 and 177682 (LG). Photon candidates are defined using the longitudinal shower development, by selecting events with energy deposition only in the first module. The energy scale is set using the π^0 mass peak. The black curve represents all the photon candidates in the MinBias stream, the red curve is for events triggered by ZDC-C.

The difference with full generators like PYTHIA or EPOS is that the generation is focused on a particular direction and only for selected particles. It does not simulate any physics processes behind the generation of particles, but it is useful to study the expected detector performance. In our case we produced 25000 π^0 and 100000 photons with a flat distribution of energy, respectively comprised between 0.5 and 3.5 TeV and 0.5 and 3 TeV, both directed towards the ZDC.
The first case is the π^0.

3.10.1 Single π^0 MonteCarlo

We can have different scenarios, because the π^0 decays in 2 photons and they both can reach the detector or be lost outside the detector acceptance. Moreover the two γ must be separated enough to reconstruct two different clusters in the detector.
Once a generated particle hits the ZDC, it is possible to apply to simulated data the same analysis used for real data. As we discussed for real data, we have to

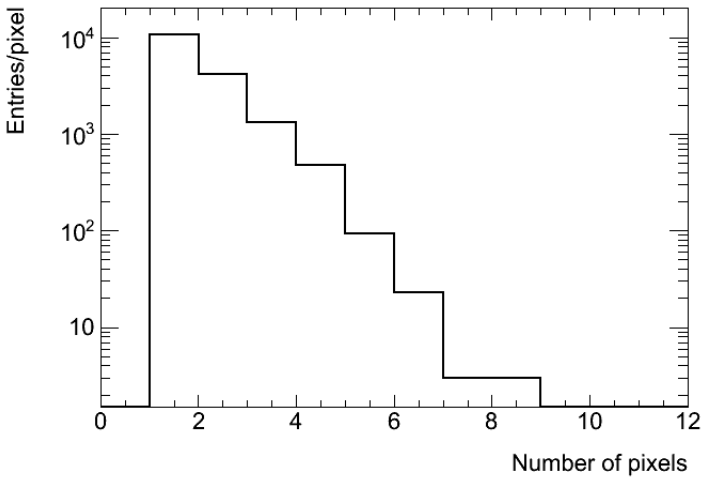

Figure 3.22: Number of pixels included in the cluster of the single photon events in ZDC-C in pp collisions at $\sqrt{s} = 7$ TeV for Runs 177531, 177540, 177593 and 177682.

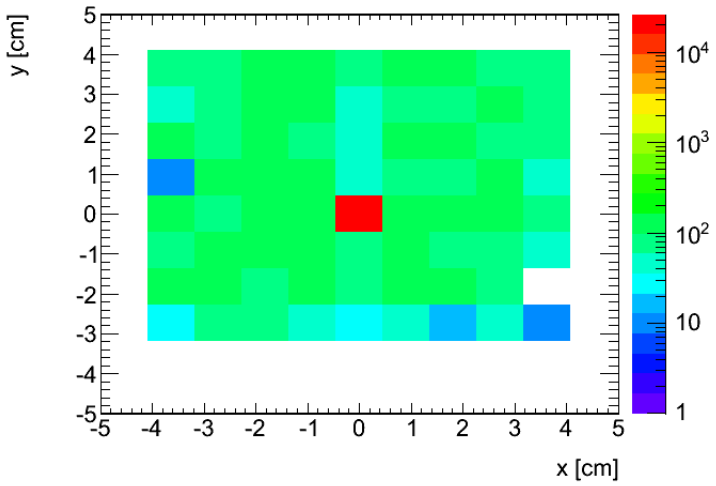

Figure 3.23: X and y coordinates of the impact position of the cluster in the EM module for single photon events in ZDC-C in pp collisions at $\sqrt{s} = 7$ TeV for Runs 177531, 177540, 177593 and 177682.

analyze signal coming from pixels (for the determination of the photon position) and from the full module read-out (for energy measurement). For the case of π^0 decay we expect 2 photons, so we accept events with 2 clusters reconstructed with

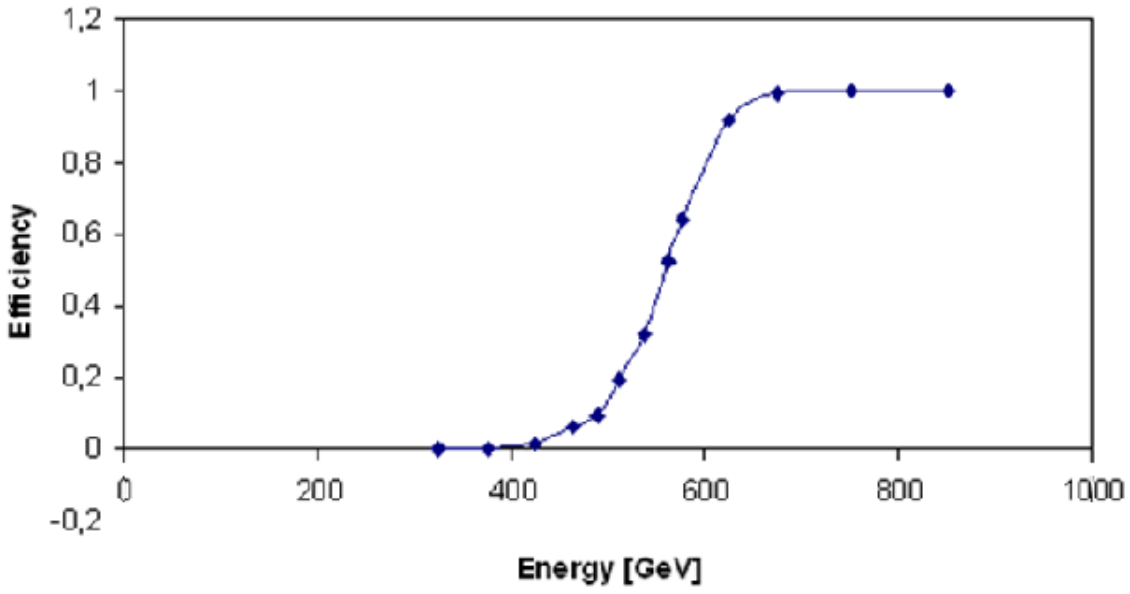

Figure 3.24: Efficiency of the ZDC trigger with respect to the MBTS trigger, in function of energy.

the EM pixels. An example about how many of them are involved every time they are hit by a photon is visible in Fig. 3.25, where we see respectively the number of pixels involved in the first and second cluster. The first reconstructed cluster corresponds to the most energetic one.
As it was observed in real data, the number of pixels composing the first cluster is higher than the one of the second cluster. The different distribution is related to the different π^0 energy of real data with respect to the single π^0 MC sample.
In Fig. 3.26 we show a distribution of the π^0 mass expressed in ADC counts, whose mean value is used for the extrapolation of the calibration constant.

We notice with respect to Fig. 3.14, that the local maximum on the left of distribution disappeared and only the tail on the right remains. Since background contribution is absent, this tail is originated by the approximations adopted in the reconstruction of photons position and energy. The relative contribution of the tail with respect to the main peak depends on the π^0 energy distribution, so the tail in Fig. 3.26 does not reflect the one expected in collision data.
The MC has been tuned in order to obtain the same mean value observed on real data.

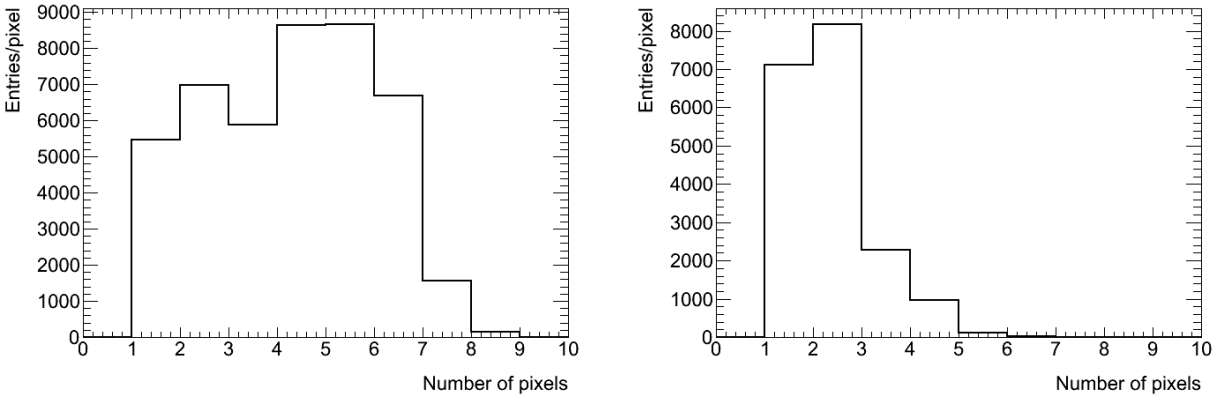

(a) (b)

Figure 3.25: Distribution of the number of pixels hit by the first (a) and second (b) EM cluster.

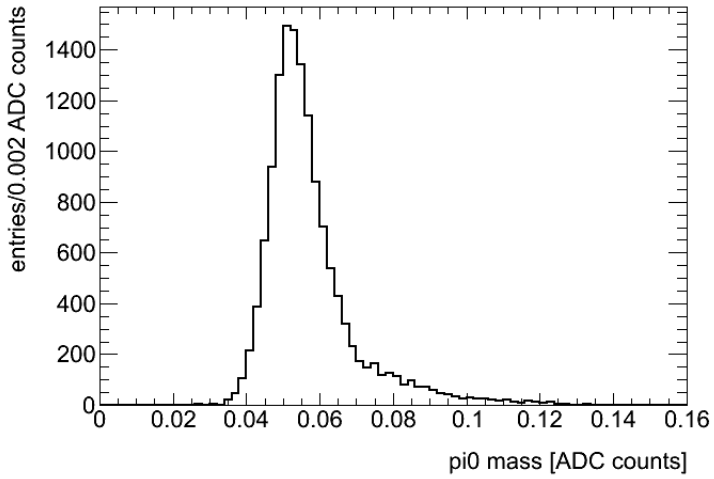

Figure 3.26: Invariant mass in ADC counts of π^0 candidates from Single π^0 MC.

We also tried to reconstruct the π^0 invariant mass on the subsample of events with distance between clusters higher than 4 cm. This has been done in order to be sure to check whether the same calibration constant is obtained when considering only well separated photons (Fig. 3.27).

We can notice that this new mass distribution presents the main peak in the same position; we can conclude that the photon separation does not affect the calibra-

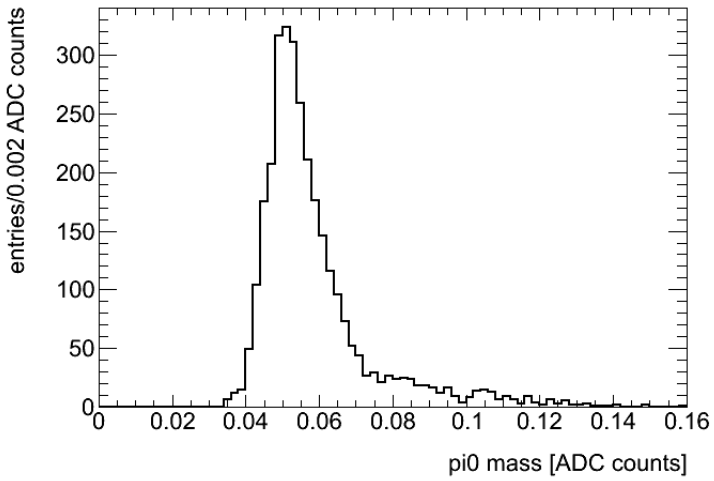

Figure 3.27: Invariant mass in ADC counts of π^0 candidates from Particle Gun generation imposing a distance between the reconstructed clusters higher than 4 cm.

tion procedure.
The MC simulation of the detector also reproduces the saturation effect observed in real data (Fig. 3.28). For this reason in the analysis of single π^0 MonteCarlo, we removed events whose clusters have energy higher than 2300 GeV.

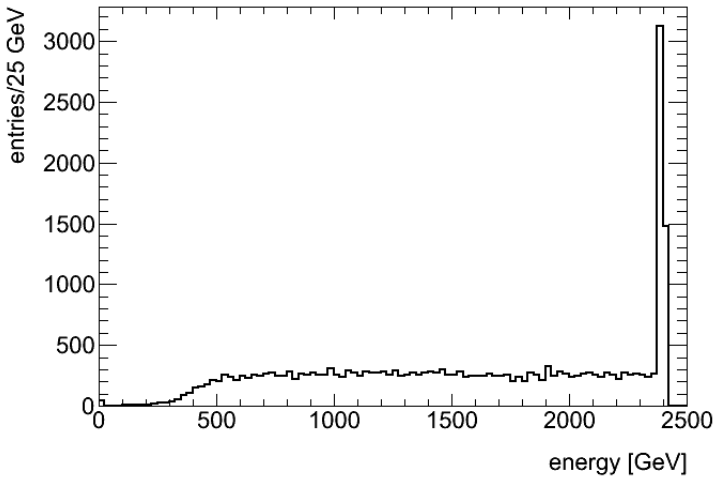

Figure 3.28: Total energy collected by the EM module.

With the same procedure used for data we can compute the calibration constant and obtain the π^0 energy distribution (Fig. 3.29), which is essentially flat above 1 TeV. When the energy falls below this value the efficiency for π^0 reconstruction decreases because the two photons are more separated and the probability that both γ fall in the detector acceptance decreases.

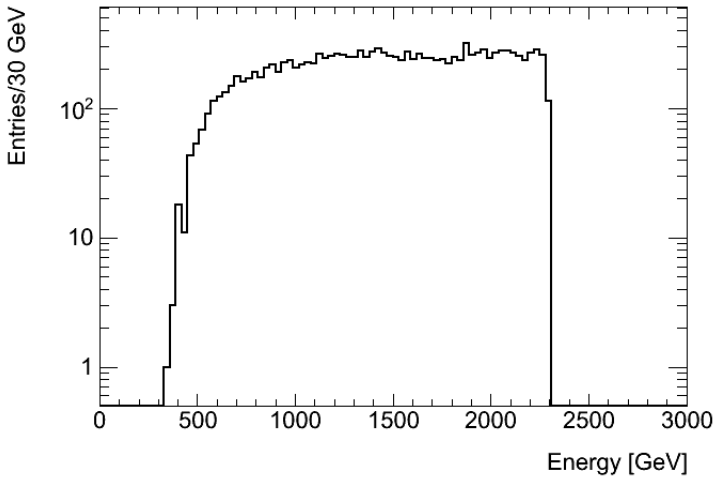

Figure 3.29: Reconstructed π^0 energy distribution from single π^0 MC.

3.10.2 Single photons MonteCarlo

The single γ scenario is simpler than the π^0 case, as it deals with only one particle. So the reconstruction involves only a single cluster, whose number of pixels is shown in Fig. 3.30.
The calibration procedure consists just by comparing the energy released in the EM module, that must be due only to single photons, with the generated single photon energy, that it is a flat distribution ranging between 0.5 and 3 TeV. Cuts applied for selecting the energy in the EM module are the same as in real data. Anyway, as only single photons have been generated in this case, we do not observe any significant signal coming from the other 3 modules, as it was expected.
The single photon calibration constant is obtained through the ratio between the generated energy and the simulated signal expressed in ADC counts. For this sample the calibration constant is 2.73 GeV/ADC. This value is applied to simulated data to obtain the single photon energy distribution, which is shown in Fig. 3.31.

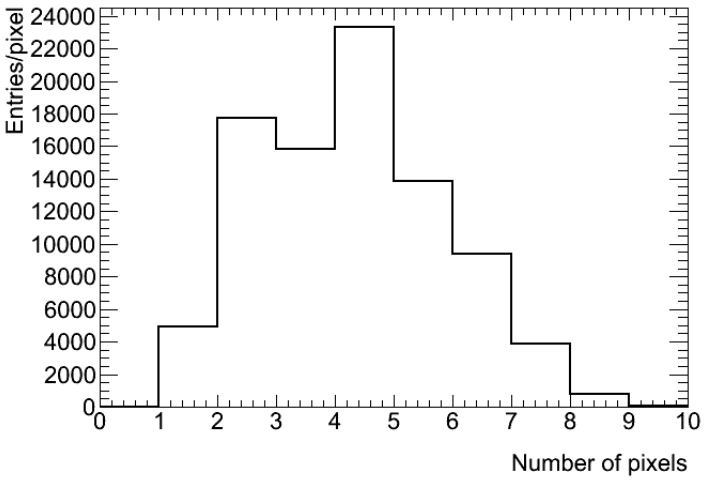

Figure 3.30: Distribution of the number of pixels forming the cluster in single photon MC events.

The distribution shows a main maximum centered at around 2.73. Applying this value to the energy collected by the EM module it is possible to reconstruct the energy distribution of the single photon.

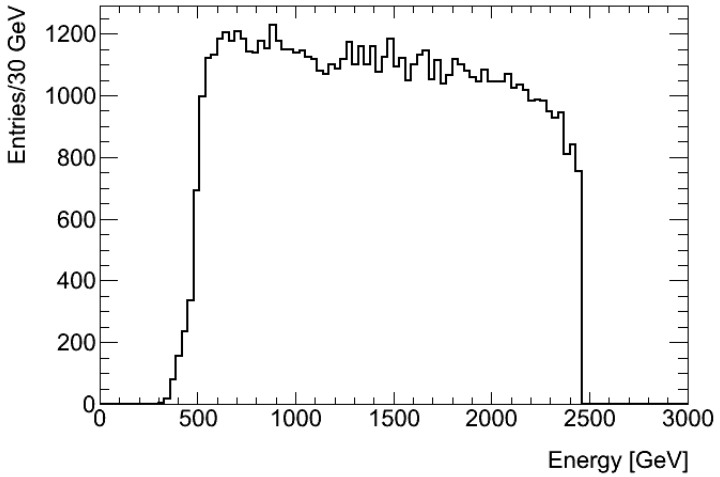

Figure 3.31: Reconstructed energy of the single photon.

It is evident from the picture how the Reconstructed energy of the single photon is in agreement with the initial conditions, that is a production of single photons

with a flat distribution of energy comprised between 0.5 and 3 TeV. In Fig. 3.31 the end point is 2.5 TeV because of the detector saturation at 900 ADC counts which corresponds to 2500 GeV.

Chapter 4

MC Simulation

MC simulators are commonly used in order to reproduce interaction events in particle accelerators and the relative detector response. A comparison between data and MC is necessary in order to test model predictions.
The MC method is usually applied to problems where the calculation of the exact answer is unfeasible or impossible.
S. Ulam, J. von Neumann and N. Metropolis were, in 1949, the first to implement the MC technique on a computer to estimate the distance that a neutron from a radioactive decay would travel in matter [37]. Since then the power of the method has been understood and widely used in almost all branches of science.
Considering the probabilistic nature of the quantum mechanics and multi-dimensional integrals it contains, the MC method is a natural match for the problems in high energy physics and found various applications in fields such as calculation of Feynman diagrams, event generation and detector simulation.
The event generators try to simulate events in accelerators in a *virtual world* including all the features concerning our understanding of the processes. However we still do not know how to describe nor how to calculate all the stages of an event formation, thus event generators compute the parts which can be calculated from first principles and use models for the rest. Typical steps in the generation of a pp or $p\bar{p}$ event can be outlined as follows [38]:

- Select a parton from both incoming particles and generate the selected interaction.

- Process the decays of the short lived particles such as Z^0, $W^{\pm}$, t coming out of the selected interaction.

- Since colored partons take part in the collision they can go through bremsstrahlung. Bremsstrahlung of the incoming partons are called Initial-State Radiation

(ISR) and outgoing partons are called Final-State Radiation (FSR). Simulate these effects.

- Repeat the same steps for other partons which could also undergo collisions.
- Only a fraction of the incoming energy is used in collisions, remaining partons (beam remnants) carry the rest of the energy and color compensating for the colors of interacting partons. All these partons and those from the hard collision move apart. Due to confinement they can only be observed as color singlets thus models for hadron formation must be employed.
- Short-lived particles such as B mesons and τ leptons that cannot be seen in detectors should be allowed to decay.

Similar steps can be applied to e^-e^+ or e^-p collisions.
The first step involves calculation of matrix elements which correspond to Feynman diagrams for many hard processes. Unfortunately, often these elements are available only at the lowest order. Several MC programs specialize in calculation of a selected set of matrix elements and pass their calculations to the generic event generators for the remaining steps. An alternative approach is called Parton Showers and works by generating complex $2 \to n$ events by factorizing them in terms of simple expressions such as $q \to qg$, $g \to gg$ and $g \to q\bar{q}$. Although it is not exact, it can provide sensible approximations [59].
Incoming and outgoing partons are allowed to emit bremsstrahlung. The emissions get harder as partons approach the main interaction and get softer as they recede. The emissions in ISR and FSR are bounded by a lower limit and upper limit and they are usually modeled by the parton shower approach. Fig. 4.1 shows a representation of the ISR.
As time progresses, the partons created in the interaction, ISR and FSR move away from each other. But they are related with each other by color connections. Since such processes can not be described by perturbative QCD, various models are used.
One of these models is String Fragmentation. In string fragmentation the partons are assumed to be connected to each other through a flux tube. As partons move away the tube is stretched until it breaks down in the middle, producing either a $q\bar{q}$ pair or diquark-antidiquark pair. The process continues until all strings are stable thus forming hadrons. The process is called fragmentation/hadronization and the model requires several parameters to be defined from the data. After the hadronization, short-lived hadrons are allowed to decay depending on their decay channels and widths.

After an event generator finishes processing an event, the results can be passed

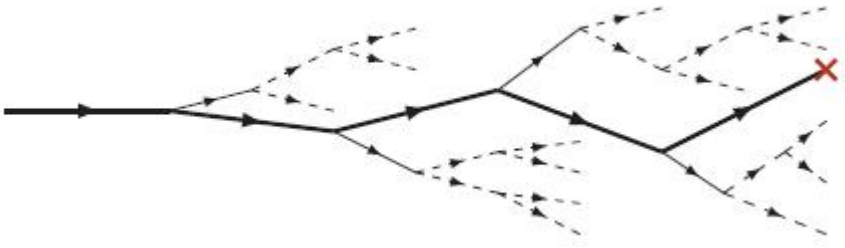

Figure 4.1: A representation of ISR. The thick line is the main parton taking part in the main interaction (the red X mark). Thin lines are partons that can not be recombined and dashed lines are further fluctuations that may or may not recombine. FSR has a similar representation.

through a detector simulation to reproduce the detector response to all the particles in the event. These detector simulations can reproduce the electronic signals observed in the real detector (hits) and can be analyzed through reconstruction and analysis programs to study various aspects of the experiment such as the trigger and data acquisition systems, efficiencies, acceptances, physics signals and possible backgrounds.
In this thesis we will consider in more detail two event generators that are commonly adopted for the simulation of the minimum bias events: PYTHIA and EPOS.

4.1 PYTHIA

PYTHIA is one of the best known and widely used event generators [39]. It has many hard QCD processes implemented and supports Super-symmetry (SUSY) and several other Beyond Standard Model (BSM) physics. It uses the Lund string model for shower evolution and can read events dumped in the Les Houches accord [40] format. It is written in FORTRAN (up to PYTHIA 6.x). The recently released versions 8.x is written in C++. PYTHIA has many parameters to alter the behavior of the program, giving advanced users a lot of flexibility. The default settings, on the other hand, enable novice users to run the program just with a couple of lines of code.
In PYTHIA the total cross-section of hadron-hadron interactions are calculated using the formula [41]:

$$\sigma_{tot}^{AB}(s) = X^{AB}s^{\epsilon} + Y^{AB}s^{-\eta} \tag{4.1}$$

where $s = E_{cm}^2$ and X^{AB} and Y^{AB} correspond to pomeron and reggeon terms depending on the initial states of incoming particles A and B. The powers are taken as $\epsilon = 0.0808$ and $\eta = 0.4525$. The elastic cross-section is calculated using the formula [59]:

$$\sigma_{el} = \frac{\sigma_{tot}^2}{16\pi B_{el}} \tag{4.2}$$

where elastic slope parameter B_{el} is parameterized as

$$B_{el} = B_{el}^{AB}(s) = 2b_A + 2b_B + 4s^{\epsilon} - 4.2 \tag{4.3}$$

with the constants $b_{A,B}$ are $b_p = 2.3$, $b_{\pi,\varrho,\omega,\phi} = 1.4$,$b_{J/\psi} = 0.23$. The diffractive cross-sections are given by [59]:

$$\frac{d\sigma_{sd(XB)}(s)}{dM^2dt} = \frac{g_{3P}}{16\pi}\beta_{AP}\beta_{BP}^2\frac{1}{M^2}e^{tB_{sd(XB)}}F_{sd} \tag{4.4}$$

$$\frac{d\sigma_{sd(AX)}(s)}{dM^2dt} = \frac{g_{3P}}{16\pi}\beta_{AP}\beta_{BP}^2\frac{1}{M^2}e^{tB_{sd(AX)}}F_{sd} \tag{4.5}$$

$$\frac{d\sigma_{dd}(s)}{dM^2dt} = \frac{g_{3P}}{16\pi}\beta_{AP}\beta_{BP}^2\frac{1}{M^2}e^{tB_{dd}}F_{dd} \tag{4.6}$$

Equations 4.4 and 4.5 represent the single-diffractive events where the first or second proton is dissociated, respectively. The double-diffractive cross-section is calculated with equation 4.6. M represents the mass of the diffractive system and coupling terms β_{AP} are related to the pomeron term in equation 4.3.
They are selected such that $\beta_{AP}\beta_{BP} = X^{AB}s_{ref}^{\epsilon}$ where $s_{ref}^{\epsilon} = \sqrt{20}GeV$. The triple pomeron coupling is taken as $g_{3P} \simeq 0.318mb^{-1}$. F_{sd} and F_{dd} are fudge factors introduced in order to obtain a sensible behavior in the whole phase space. These equations are integrated over the full phase space at different center-of-mass energies and the results are parameterized. The nondiffractive cross-section σ_{nd} is found by subtracting diffractive and elastic cross-sections from the total cross-section given by equation 4.3 [59]. Details about calculations of diffractive cross-sections and the parameterization are available elsewhere [39, 42].
Starting from the PYTHIA 8 version 8.130, a new mechanism for diffractive event production making use of the pomeron PDFs is introduced. The details of the mechanism are reported in [43].
For some values of p_{Tmin} and s, σ_{hard} might exceed σ_{tot}. Although this might seem unphysical it can be interpreted as the total cross-section of multiple parton interactions rather than one interaction [44]. In PYTHIA the average number of parton-parton interactions in an event is found by using the relation $< n >= \frac{\sigma_{hard}}{\sigma_{nd}}$, where σ_{nd} is the non-diffractive cross-section. Multiple parton interactions are modeled with or without a dependence on the transverse distance between

the incoming partons, the impact parameter. The basic model assumes no impact parameter dependence. The advanced model uses different matter distribution models, one of which is a co-centric double-Gaussian with individual mass densities given by:

$$\rho(r) \propto \frac{1-\beta}{a_1^3} e^{\frac{-r^2}{a_1^2}} + \frac{\beta}{a_2^3} e^{\frac{-r^2}{a_2^2}} \tag{4.7}$$

In this equation a_1 and a_2 correspond to the variances of the outer and inner Gaussians, respectively, and β is the fraction of the total hadronic matter inside the Gaussian. Fig. 4.2 shows an example distribution with default parameters.

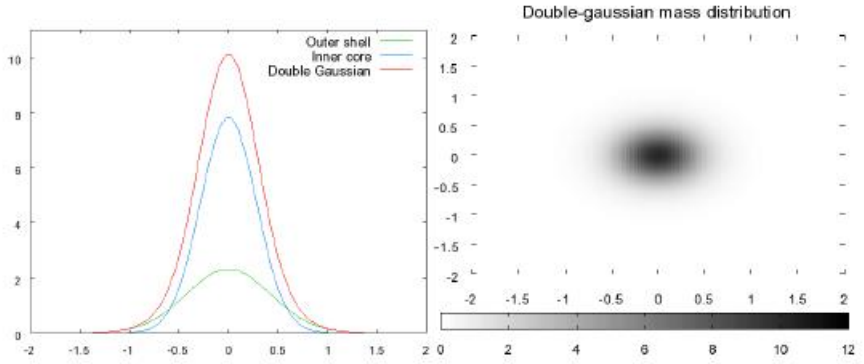

Figure 4.2: An example of double-Gaussian matter distribution given in equation 4.7 with parameter settings $a_1 = 0.6$, $a_1 = 0.4$ and $\beta = 0.5$. Left plot shows Gaussian distributions representing combined, inner-core and outer-shell. Right plot shows the distribution viewed from above [59].

Another impact parameter dependent model uses a matter overlap profile in the form of

$$O(b) \propto e^{-b^d} \tag{4.8}$$

where b is impact parameter of the collision and d is the model parameter. Details about the models and event generation are available in reference [45]. The divergence of hard cross section at $low - p_T$ is regulated either by a sharp or a gradual cutoff [44]. Gradual regularization is done by multiplying the matrix elements with the factor:

$$R = \frac{\alpha_s(p_{T_0}^2 + p_T^2)}{\alpha_s(p_T^2)} \frac{p_T^4}{(p_{T_0}^2 + p_T^2)^2} \tag{4.9}$$

With this approach the perturbative QCD cross-section is recovered when p_T is sensibly higher than p_{T_0} and strongly damped otherwise. Hard interaction cut-off

$p_{T_{min}}$ and the regulation parameter p_{T_0} are chosen as energy dependent values, given by the formulae:

$$p_{T_{min}}(E_{cm}) = p^{ref}_{T_{min}}(\frac{E_{cm}}{E^{ref}_{min}})^{E^{pow}} \tag{4.10}$$

$$p_{T_0}(E_{cm}) = p^{ref}_{T_0}(\frac{E_{cm}}{E^{ref}_{0}})^{E^{pow}} \tag{4.11}$$

In these equations, E^{ref}_0 and E^{ref}_{min} represent the scales where p_{T_0} and $p_{T_{min}}$ are equal to their respective reference scales $p^{ref}_{T_0}$ and $p^{ref}_{T_{min}}$. E^{pow} is common in both equations and defines the extrapolation slope. These parameters should be determined from collision data. $p^{ref}_{T_0}$, $p^{ref}_{T_{min}}$ and E^{pow}, together with the matter distribution parameters, are important parameters in the tuning process. In PYTHIA initial state showers do not evolve below $Q_0 = 1$ GeV. However this is compensated by assigning a primordial k_T to shower initiators as a source of softer activity. There are different choices for the distributions of primordial k_T. An example for PYTHIA 6 it is

$$e^{-\frac{(k_T)^2}{\sigma^2}} k_T dk_T \tag{4.12}$$

with an upper cut-off. On the other hand for PYTHIA 8 it is a Normal distribution with a width

$$\sigma = \frac{\sigma_{soft} Q_{half} + \sigma_{hard} Q}{Q_{half} + Q} \frac{m}{m_{half}} \tag{4.13}$$

where Q is the scale of the hardest process, m is the mass of the system and σ_{hard}, σ_{soft}, Q_{half} and m_{half} are parameters [59]. Explaining the capabilities and models in PYTHIA is beyond the scope of this thesis. For detailed discussions and explanations of the models used in PYTHIA 6 and PYTHIA 8, see [39, 43, 46] and the reference therein.

4.2 EPOS

EPOS stands for Energy conserving quantum mechanical multiple scattering approach, based on Partons (parton ladders) Off-shell remnants and Splitting of parton ladders.
EPOS is a hadronic interaction model with a multiple scattering approach based on partons and pomerons [47]. The EPOS generator is used also to simulate heavy-ion collisions and cosmic-ray interactions and can describe the existing minimum bias data quite accurately [48, 49, 50, 51].
Parton ladder structure is composed of two parts, a hard part including the space-like initial state cascade and the hard interaction, and a soft part which is a purely

phenomenological object parameterized in Regge pole fashion [47]. In addition to the parton ladder, remnants of the incoming particles are included in calculations as colorless and usually off-shell objects. The energy-momentum sharing is taken into consideration at the parton-ladder level which is a unique feature of EPOS. Such a parton-ladder may be considered as a longitudinal color field or flux-tube [52], conveniently treated as a relativistic string.

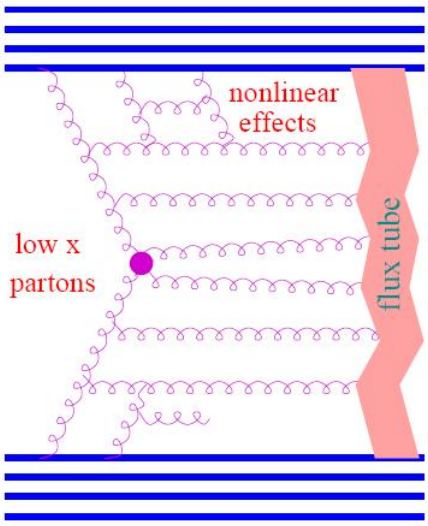

Figure 4.3: Elementary interaction in the EPOS model [52].

The intermediate gluons are treated as kink singularities in the language of relativistic strings. This flux tube approach is just a continuation of 30 years of very successful applications of the string picture to particle production in collisions of high energy particles [53, 54, 55, 56], in particular in connection with the parton model. An important issue at high energies is the appearance of so-called nonlinear effects, which means that the simple linear parton evolution is no longer valid, gluon ladders may fuse or split.
All realistic string model implementations have nowadays to deal with screening and saturation, and EPOS is not an exception, (see [49, 57]). Without screening, proton-proton cross sections and multiplicities will explode at high energies.
A phenomenological treatment of non-linear effects in EPOS employs two contributions: a simple elastic rescattering of a ladder parton on a projectile or target nucleon (elastic ladder splitting), or an inelastic rescattering (inelastic ladder splitting), see fig. 4.4.
The elastic process provides screening, therefore a reduction of total and inelastic cross sections.

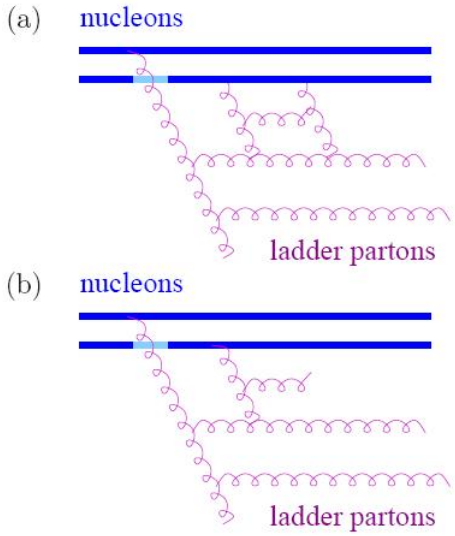

Figure 4.4: (a) Elastic "rescattering" of a ladder parton. We refer to elastic parton ladder splitting; (b) Inelastic "rescattering" of a ladder parton. We refer to inelastic parton ladder splitting.

Finally we have to mention that another unique feature is the use of the same formulae for the partial cross-section calculation and parton generation.
Anyway EPOS also has several drawbacks. Probably the most notable one is the lack of a manual. Another one is that it does not have process selection and certain processes are not implemented yet. However these problems are expected to be solved in the near future and it can be used for the minimum bias predictions at the LHC already. The details of the EPOS model are available in [47, 49, 58] and the references therein.

4.3 MC tuning

Due to the uncertainties in the underlying models, Monte Carlo event generators usually have parameters which can be tuned to better describe the data. The tuning process involves comparison of MC generated distributions with data and adjustment of the parameters until they match.
There are two important issues in MC tuning. One of them is the generation of distributions. The generation of MC distributions should be done as close to the experimental conditions as possible. The event generation and selection to describe the experimental conditions is the most important and most crucial step of any tuning process, since it defines the optimum parameter set. That is, the optimum

parameter set for a crude implementation of event selection and experimental conditions can be very different than a detailed one.
Another important thing in tuning is the search method used in finding the optimum set. The parameters are altered within given ranges which form a volume with the number of dimensions equal to the number of parameters to tune. Each parameter set correspond to a point within this volume. Usually a MC generator has several parameters to tune which makes the volume of the parameter space

$$V = \Pi r_i \tag{4.14}$$

where r is the range of parameter. Thus as the number of parameters and their ranges increase it becomes harder to find an optimum parameter set. This part is essentially a search problem in a multi dimensional space.
There are various methods used in search problems. In general, the following list of methods are used for steering the search of a good parameter set:

- manually by eye;
- fitting distributions to the data;
- brute force;
- parameterization;
- Genetic Algorithms.

Probably the most basic approach to tuning a generator would be changing some parameters and looking at the distributions. In this method, user steers the parameters depending on his or her observations of the distributions. Although this method produced some of the most commonly used tunes to date, it requires expertise and depends on the judgement of the person. Moreover it becomes a cumbersome process as the number of parameters or distributions increase.
Another approach is trying to fit the generator response to the data using a minimization package such as Minuit [60]. This method can work, but it has very little potential to be run in parallel and for each point in the parameter space, evaluation of several points required for calculating the derivatives. Considering that the evaluation of a point may take a long time, it quickly becomes unfeasible for large number of parameters. The brute force approach is based on random evaluation of the points in the parameter space with the hope that one of them will be a good match to data. It can be parallelized and might work for one or two parameters with small ranges. However it quickly becomes unfeasible for any realistic number of parameters.
The idea of the parameterization of the generator response is based on the evaluation of randomly selected points in the parameter space and then bin-by-bin

parameterizing the resulting distributions using a polynomial function of the parameters. A tool called Professor [61, 62, 63] using the approach based on the ideas in [64] works in this manner. In Professor, generator response for each distribution is bin-by-bin parameterized using a second or third order polynomial function of tuned parameters by singular value decomposition method. Then a minimization is done using these parameterized distributions to find the optimum values of the parameters. A detailed description of Professor can be found in [65] and the references therein.
The parameterization approach provides a way of doing systematic tuning and reducing the subjectivity. However it assumes the generator response can be sufficiently approximated by a polynomial function of the input parameters. The order of this polynomial cannot be very high since the minimum number of evaluations required for a singular value decomposition is

$$\sum \frac{(n+P-1)!}{n!(P-1)!} \tag{4.15}$$

where n can reach a maximum equal to N, that is the order of the polynomial, and P is the number of parameters.
Parameterizing the generator response permits the use of analytic minimization techniques, however if the generator response is more complicated than the polynomial, the minima of the function set might not necessarily be even a local minima. Genetic Algorithms provide a compromise between the analytic search and random sampling. They do not make any assumptions about the functional dependence of the generator response on the parameters and are less likely to converge to a local minimum. In this respect it is a combination of all previous methods [59].
In particular for the analysis, we are particularly interested in Pythia and Epos. The most recent release of Pythia used in this thesis is 8. Among their tunings, we selected the A2CTEQ6L1 and MSTW2008LO. Anyway for each generators, there are several tunings, summarized in Tab. 4.1 [66].
What differs between these 2 tuning is the parton distribution function (PDF). The first thing to note is that moving from the CTEQ6L1 to the MSTW2008LO PDFs (and keeping all tune parameters the same) decreases the amount of energy in the central region of the ATLAS detector, but increases it in the forward region, presumably due to the increase in both the high-x and low-x gluon PDF with respect to the mid-x region, where x is the proton momentum fraction carried by the gluon. When the parameters are tuned to data in the central region, the energy increases for the minimum bias prediction. For example, if we scale down the transverse energy density obtained using A2CTEQ6L1 to match the MSTW2008LO in the most central bin, the latter provides a better description of the data in the forward region.

Generators	Version	Tune	PDF	MB	UE
Pythia6	6.423	AMBT1	MRSTLO*	yes	no
Pythia6	6.423	DW	CTEQ6L	no	no
Pythia6	6.423	Perugia0	CTEQ6L	no	no
Pythia8	8.145	4C	CTEQ6L1	yes	no
Herwig++	2.5.1	UE7-2	MRSTLO**	no	yes

Table 4.1: MC tunes used to unfold the data and to determine the physics model dependent systematic uncertainty. The last two columns indicate whether the data used in the tune included 7 TeV minimum bias (MB) and/or underlying event (UE) data.

4.4 Generated energy distributions

In this section some preliminary results concerning the energy distribution of particles generated by EPOS and PYTHIA for pp collisions at LHC will be shown. Chosen datasets have been taken generated and processed in the "ATHENA" framework of the ATLAS experiment and for each of them 250000 events has been selected both for the EPOS and PYTHIA generators. In particular we chose the following generators: EPOS, Pythia8 A2CTEQ6L1, Pythia8 MSTW2008LO, Pythia6 AUET24Minus, and Pythia6 Perugia2011. Every collision has been simulated with a center of mass energy equal to 7 TeV. We will focus on neutral particles produced at high pseudorapidity in the ZDC acceptance region (η>8.5), like neutrons, gamma and pions.
Figure 4.5 shows the energy spectrum of the event generator level of these selected particles.
In Figure 4.5a we can notice a good agreement between the PYTHIA8 generators with the 2 different tunings and a small difference between EPOS and PYTHIA, as the maximum of the energy distribution for EPOS is centered at around 2 TeV while for PYTHIA at 1.3 TeV, with the same endpoint at 3.5 TeV.
In Fig. 4.5b also we have a little difference between 2 Pythia6: the Perugia11 Tuning with the other one (AUET24Minus).

For what concerns gammas both EPOS and PYTHIA8 show the same shape of the energy distribution (Fig. 4.6). The only noticeable difference regards the highest energies: we have very nice agreement till 600 GeV, then PYTHIA8 foresees a bigger amount of γ in the whole spectrum, becoming bigger towards the endpoint (around 3 TeV). Again, for the PYTHIA generators with the 2 different tunings we obtain almost the same distribution.
Gammas generated by the two Pythia6 tunings show a similar distribution (Fig. 4.6b), with the Perugia11 Tuning ranging between an agreement with the other

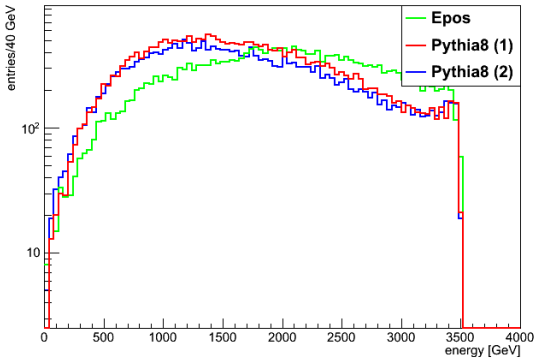

(a)

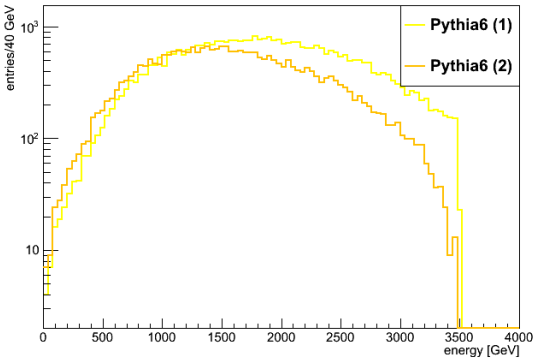

(b)

Figure 4.5: Energy distribution for neutrons with $\eta > 8.5$ (ZDC acceptance) coming from 250000 selected events generated by EPOS, PYTHIA8 A2CTEQ6L1 (1) and Pythia8 MSTW2008LO (2) and by PYTHIA6 AUET24Minus (1) and PYTHIA6 Perugia2011 in collisions with a center of mass energy equal to 7 TeV.

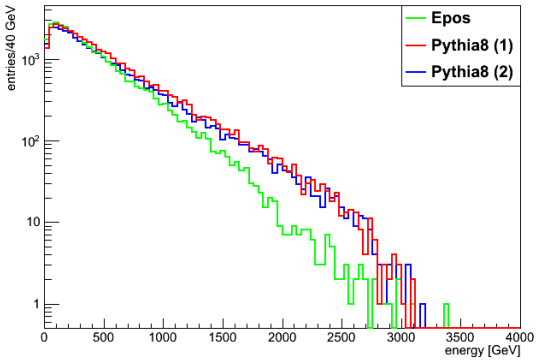

(a)

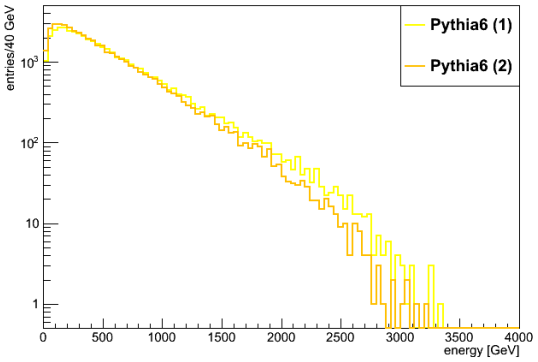

(b)

Figure 4.6: Energy distribution for gamma coming from 250000 selected events generated by EPOS and PYTHIA8 A2CTEQ6L1 (1) and Pythia8 MSTW2008LO (2) and by PYTHIA6 AUET24Minus and PYTHIA6 Perugia2011 (2) in collisions with a center of mass energy equal to 7 TeV.

Pythia6 Tuning AUET24Minus and a little difference at higher energies.

Similar considerations are valid for π^0: the PYTHIA8 distribution is still higher than EPOS at higher energies but with the difference that at lower energies roles

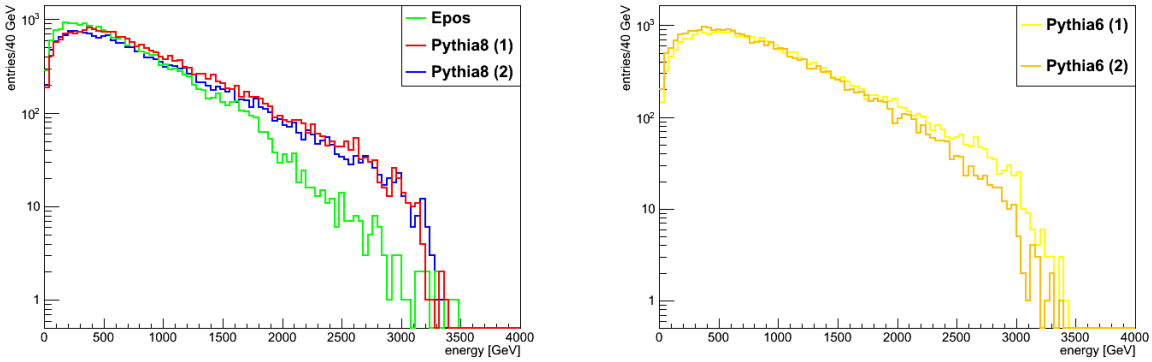

(a) (b)

Figure 4.7: Energy distribution for π^0 coming from 250000 selected events generated by EPOS, PYTHIA8 A2CTEQ6L1 (1) and PYTHIA8 MSTW2008LO (2) and by PYTHIA6 AUET24Minus (1), PYTHIA6 Perugia2011 (2) in collisions with a center of mass energy equal to 7 TeV.

are inverted,as PYTHIA shows a smaller amount of entries with respect to EPOS (Fig. 4.7). A small difference in forward π^0 production can be noticed at very high π^0 energies for the two Pythia6 tunings (Fig. 4.7b).

4.5 The detector response

All the samples from the different event generators are passed to the full detector simulation. Particles reaching the ZDC detector interact with it and it is possible to simulate the detector response. The full detector simulation has been realized through the use of GEANT4 [67], a MC software for the simulation of the interaction between particles and matter. It simulates the particles hitting the detector and the signal produced in the active parts of the detector, as it happens for real data.
We started the MC analysis with a sample of 250000 events (the generation phase, see Section 4.4). The full detector simulation is a CPU intensive process. For the purpose of this study, in order to have enough statistics to be compared with real data, we produced a sample of 50000 events with full detector response.
The procedure for the π^0 reconstruction is the same used for real data, that is the signal coming from pixels is used for the determination of the photon position and the energy collected by the module PMT is equally divided between the 2 photons. The simulated signal distribution in the EM module of the ZDC for EM events

is shown in Fig. 4.8. It is possible to observe the High Gain read-out saturation reproduced as in real data at 900 ADC counts.

Fig. 4.9 shows the π^0 reconstructed mass for the 5 selected generators: Pythia8

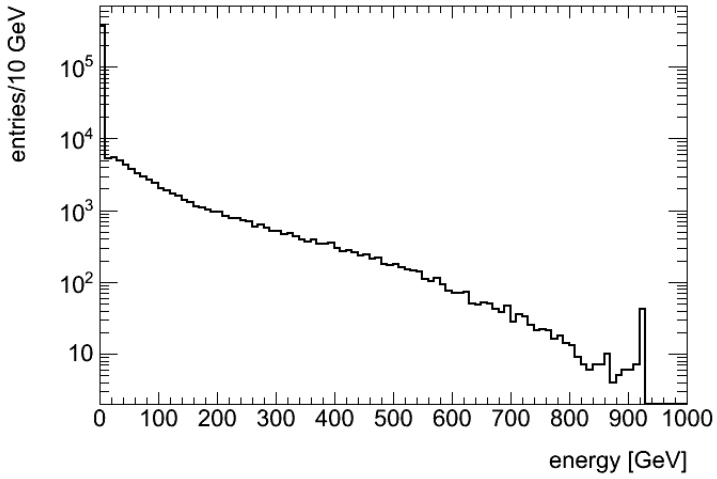

Figure 4.8: Energy collected (ADC counts) by the EPOS MC simulated response of the EM module. It is evident a saturation at 900 ADC counts, like the one observed in real data.

A2CTEQ6L1, Pythia8 MSTW2008LO, EPOS, Pythia6 AUET24Minus and Pythia6 Perugia2011.

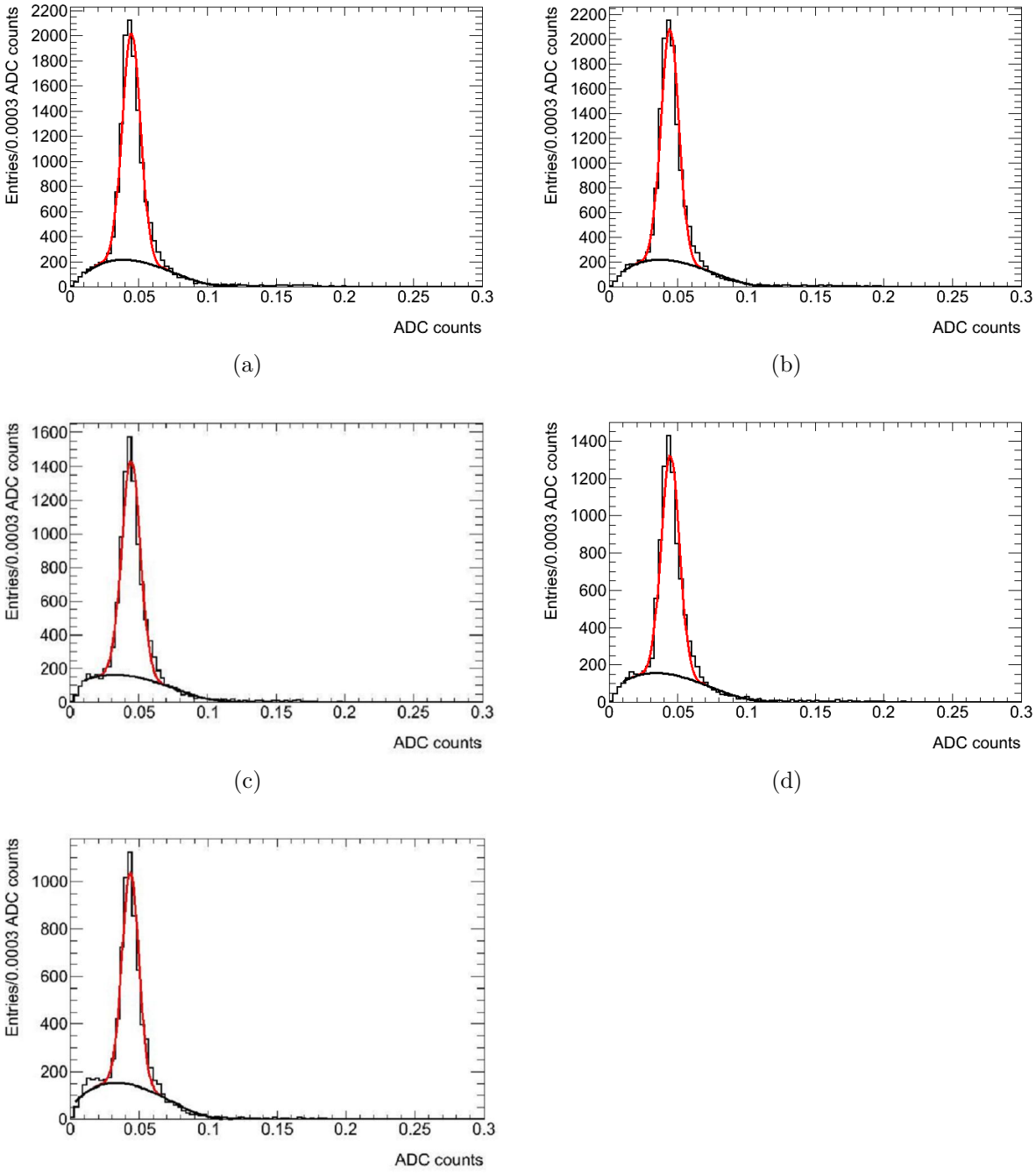

Figure 4.9: Uncalibrated π^0 reconstructed mass with Pythia6 AUET24Minus (a), Pythia6 Perugia2011 (b), Pythia8 A2CTEQ6L1 (c), Pythia8 MSTW2008LO (d) and EPOS (e). The distribution is fitted using the sum of a gaussian distribution for the main π^0 peak and a Polynomial of 3 degree distribution for the background events, whose contribution is shown by the black curve.

The fit has been made using 2 different distributions: a gaussian for the main π^0 peak and a Polynomial of 3 degree for background, as it was done for real data. Actually in the MC sample we can observe much less background contribution. In fact we can notice that the local maximum due to background on the left of the main π^0 peak present in Fig. 3.14, is absent in Fig. 4.9.
In the MC simulation only primary interactions are considered and the effect of pile-up is neglected, so the signal is much cleaner with respect to real data. Anyway the same function used in the analysis of real data was adopted to model simulated data, as the third degree polynomial has a relatively small effect on the fit result.
This leads the main π^0 peak to be narrower than the one obtained from real data.
Repeating the same procedure for the π^0 reconstruction for all the 5 MC gener-

MC	Peak Position	σ	σ/Peak Position
Pythia8 A2CTEQ6L1	0.044	0.0069	0.157
Pythia8 MSTW2008LO	0.044	0.0067	0.152
EPOS	0.044	0.0061	0.139
Pythia6 Perugia11	0.044	0.0065	0.148
Pythia6 AUET24Minus	0.045	0.0067	0.149

Table 4.2: Runs at 7 TeV chosen for analysis.

ators we obtained 5 calibration constants. A tuning of the signal produced by the full detector simulation was necessary in order to have for MC a calibration constant approximately matching the other observed for real data. After these tunings the 5 calibration constants are listed in Table 4.3. Hence it is possible to have the

MC Generators	Calibration constant [GeV/ADC counts]
Pythia8 A2CTEQ6L1	3.07
Pythia8 MSTW2008LO	3.07
EPOS	3.07
Pythia6 AUET24Minus	3.00
Pythia6 Perugia2011	3.07
Pythia	3.07

Table 4.3: MC Generators and their calibration constant.

reconstructed energy distribution in GeV of the same π^0. Results for the 5 MC generators are shown in Fig 4.10. These plots has been obtained collecting the energy from the EM module and considering only events where exactly 2 clusters has been reconstructed.

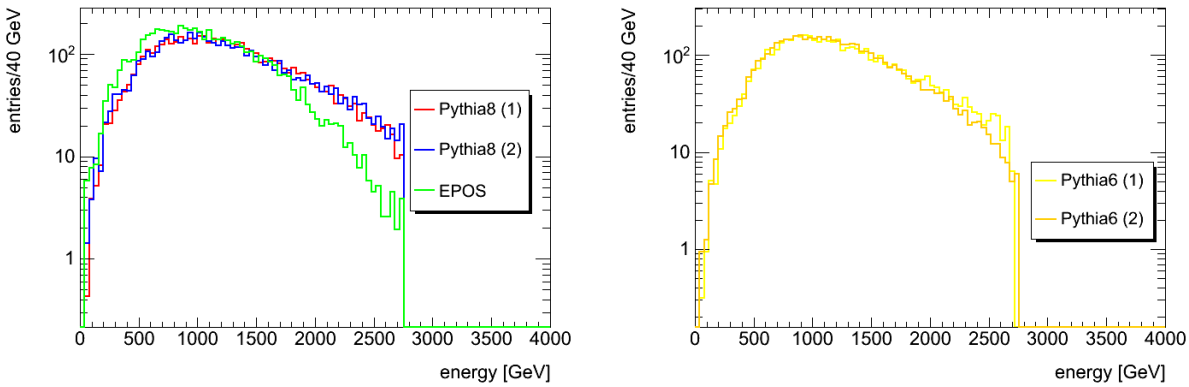

(a) (b)

Figure 4.10: Distribution of reconstructed energy of the π^0 obtained from the simulated detector response with Pythia8 A2CTEQ6L1 (1), Pythia8 MSTW2008LO (2) and EPOS and with Pythia6 AUET24Minus (1) and Pythia6 Perugia2011 (2). The sharp cut at around 2.7 TeV corresponds to the rejection of events saturating the HG read-out of the ZDC.

Selecting instead only events with a single cluster, the relative total energy collected by the EM module is the energy of a single photon candidate, whose distributions calculated from the 5 MC generators are shown in Fig. 4.11. For what

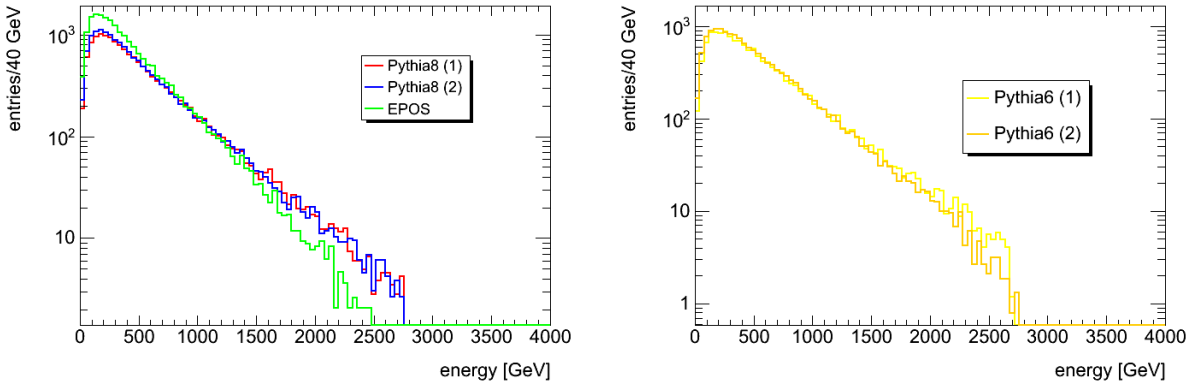

(a) (b)

Figure 4.11: Distribution energy of the single photon candidate obtained from the simulated detector response with Pythia8 A2CTEQ6L1 (1), Pythia8 MSTW2008LO (2) and EPOS and with Pythia6 AUET24Minus (1) and Pythia6 Perugia2011 (2).

concerns the impact position of the single photon candidate, we saw that it is mostly concentrated around the center of the detector (Fig. 4.12). It is evident how all the 5 generators are in a good agreement to each other.
Then, Fig. 4.13 (EPOS has been chosen for this test, similar results are obtained for the other generators) demonstrated that this photon spatial distribution does not depend on the photon energy as it is present at all energy scales.

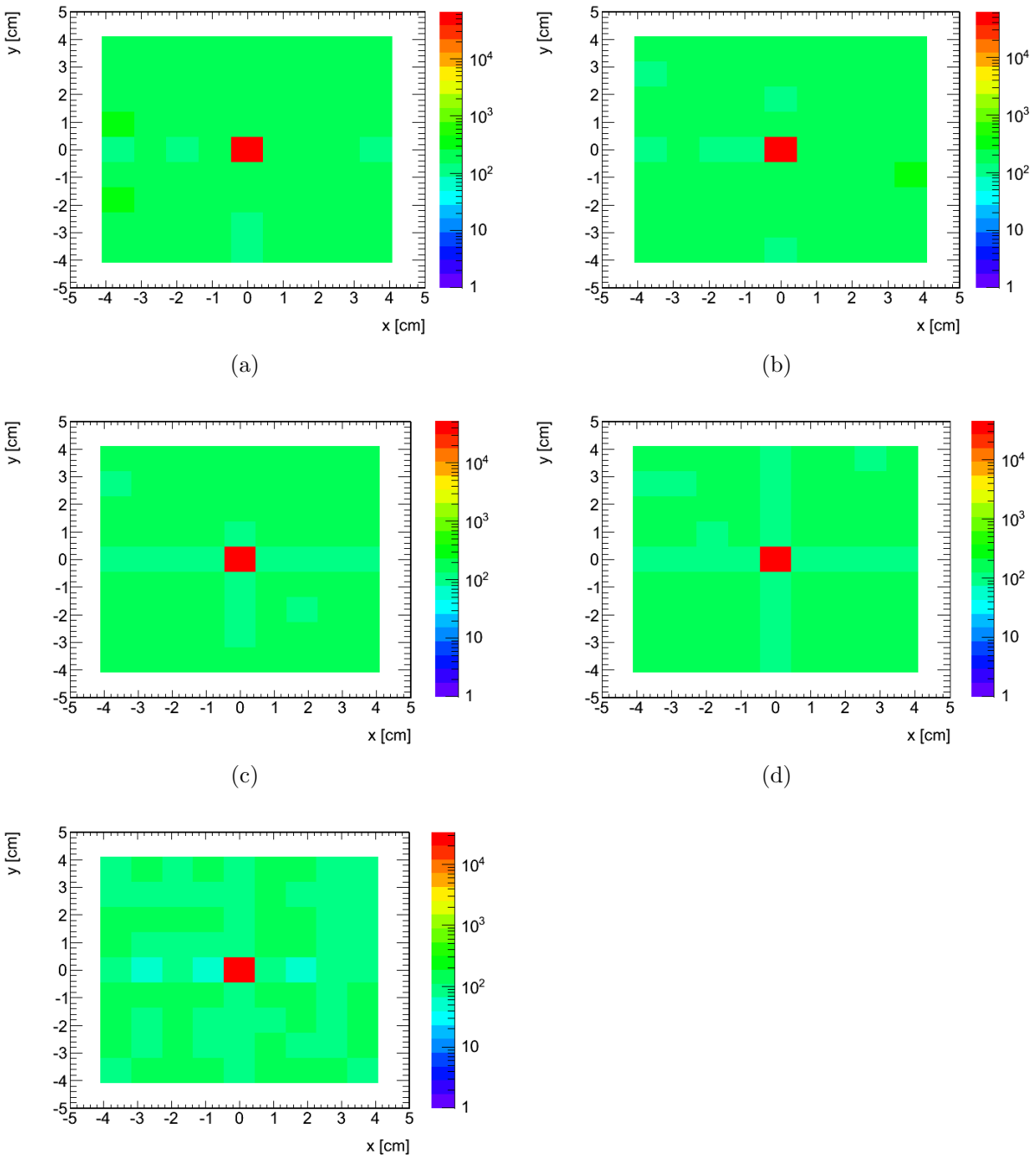

Figure 4.12: Distribution of the impact position of the single photon candidate in the EM module simulated by the Pythia6 generators Perugia11 (a) and AUET24Minus (b), the Pythia8 generator A2CTEQ6L1 (c) and the MSTW2008LO (d) and EPOS (e).

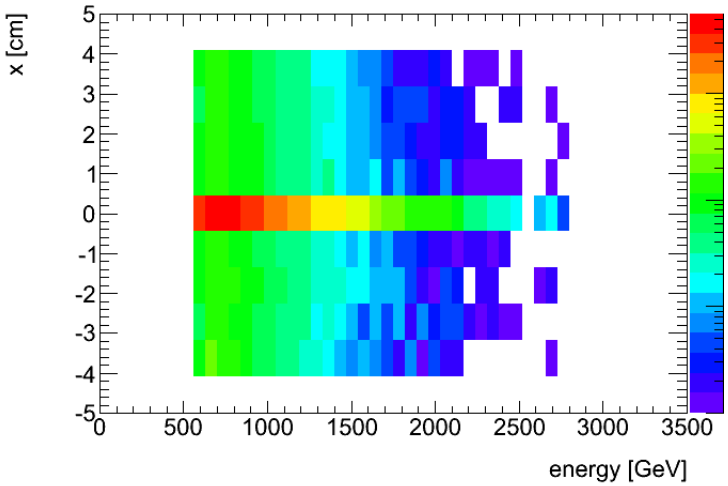

Figure 4.13: Distributions of the impact position on the x axis of the single photon candidate simulated in function of the energy collected by the EM module and simulated by EPOS.

Chapter 5

Conclusions

In this chapter we will discuss the comparison of the forward photon energy distribution observed in pp collisions at $\sqrt{s} = 7$ TeV with the predictions of Pythia6, Pythia8, and EPOS MonteCarlo generators.
Fig. 5.1 and 5.2 show the energy distribution of single photon candidates obtained from the high gain (HG) and low gain (LG) read-out chain.
MC results have been normalized in order to obtain the same number of events observed in data in the whole energy range where the ZDC is fully efficient, that is for photon energies > 700 GeV (see Sec. 3.9).
The generators yield a good description of the energy distribution observed in data at intermediate energies (700-1500 GeV). In this range the ratio between MC and data is close to 1, in particular for the two Pythia6 and the two Pythia8.
At higher energies the behavior of the 5 selected MC generators differs. EPOS underestimates data, at highest energies the ratio between MC and data reaches the 0.3 value. Instead the two Pythia6 and the two Pythia8, which show a similar behavior, overestimate data, but with less difference with respect to data than EPOS. The ratio between MC and data obtained from Pythia6 and Pythia8 show a peak at 2200-2300 GeV, where it reaches the value of 3, although with a large statistical error.
We can conclude that among the 5 generators, the 2 Pythia6 and Pythia8 show a better behavior (LG and HG) with respect to EPOS, which underestimates data. In particular MSTW2008LO for Pythia8 and Perugia11 for Pythia6 fit better data with a ratio MC/data which never exceeds 2.5.
In Fig. 5.3 we also compared the horizontal and vertical coordinates, relative to the impact on the EM module of the single photon candidates.

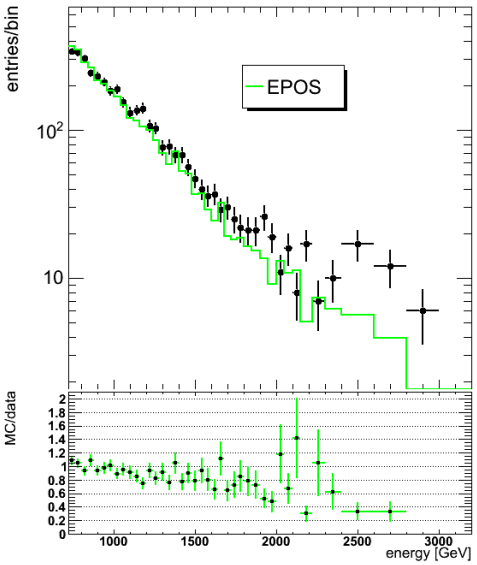

(a)

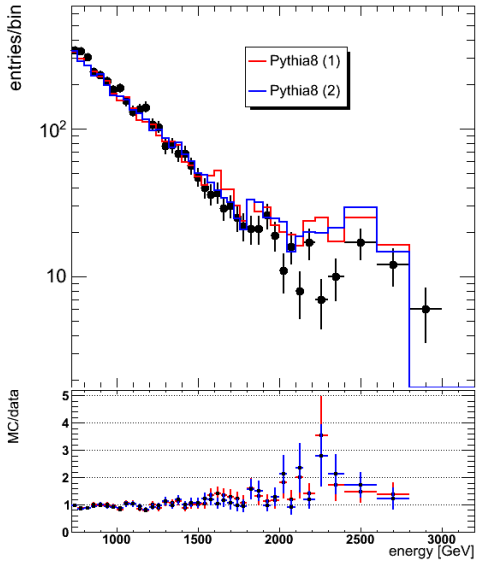

(b)

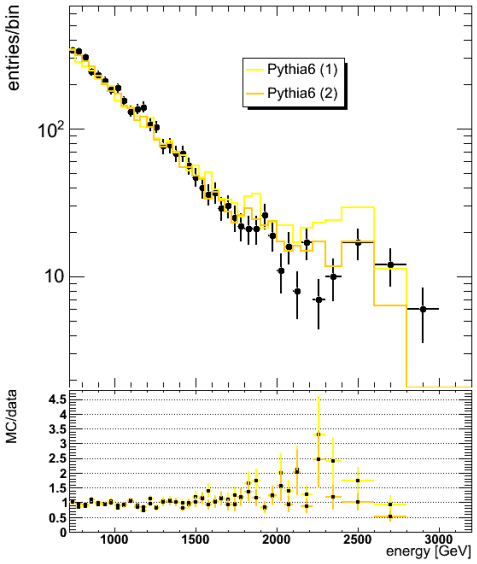

(c)

Figure 5.1: Energy distribution of single photon candidates reconstructed in the ZDC-C from the HG read-out chain for pp collisions at 7 TeV and simulated by EPOS (a), the two Pythia8 tunings (b) and the 2 Pythia6 tunings (c).

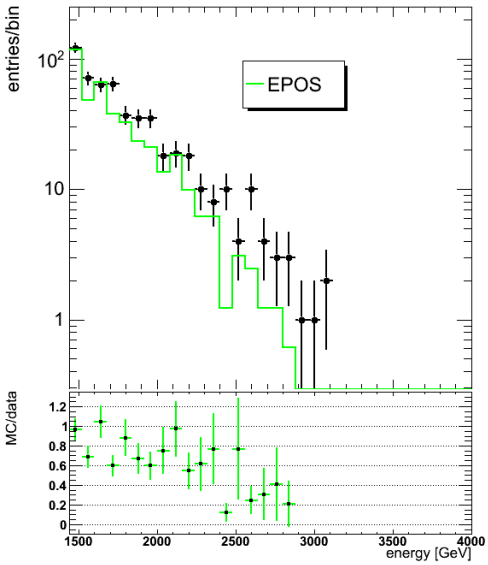

(a)

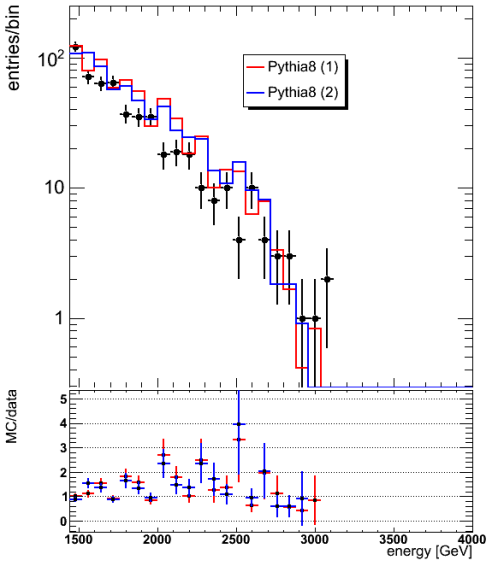

(b)

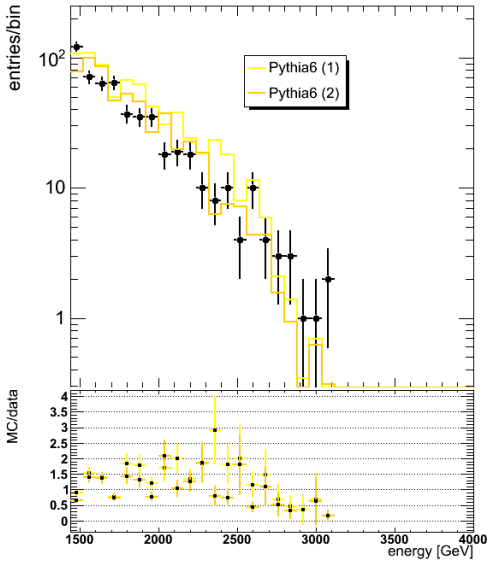

(c)

Figure 5.2: Energy distribution of single photon candidates reconstructed in the ZDC-C from the LG read-out chain for pp collisions at 7 TeV and simulated by EPOS (a), the two Pythia8 tunings (b) and the 2 Pythia6 tunings (c).

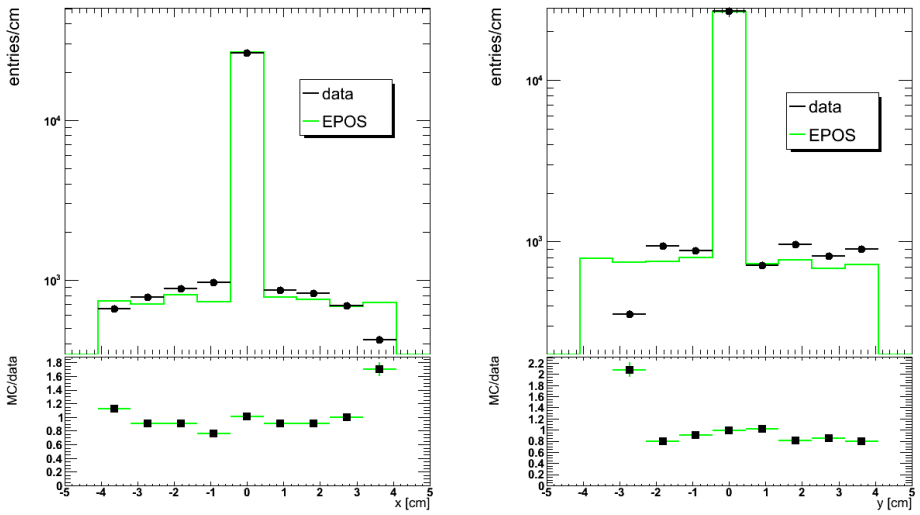

(a)

(b)

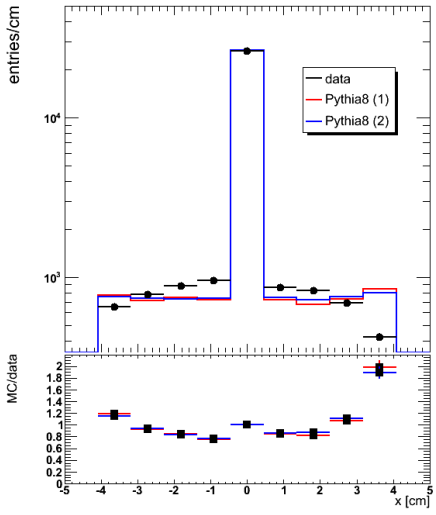

(c)

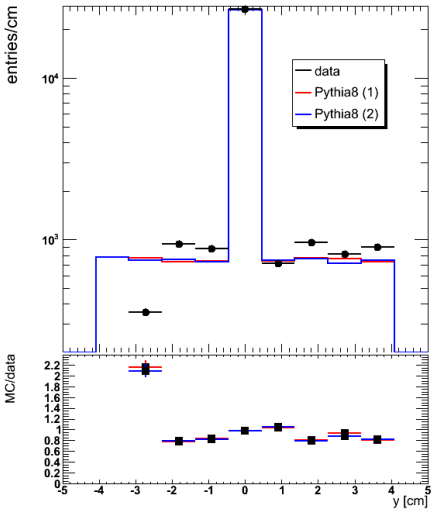

(d)

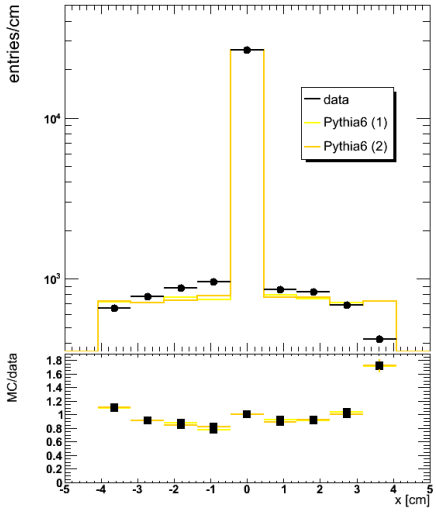

(e)

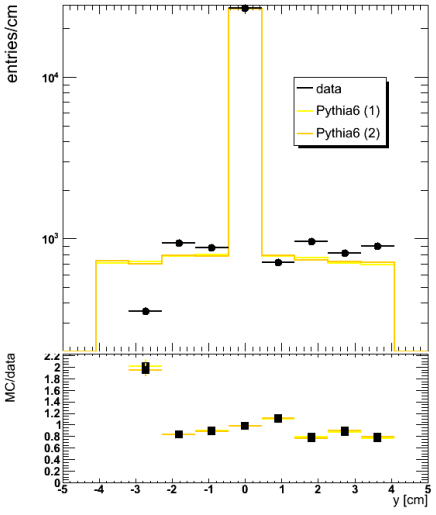

(f)

Figure 5.3: X and Y coordinate distributions in the EM module of single photon candidates from data and EPOS (a,b), the 2 selected Pythia8 tunings (c,d) and Pythia6 tunings (e,f).

Also in this case we can see that in the 2 plots MC prediction is consistent with data, concentrating the most part of the single photons in the center of the detector.
Also around the center, there is consistency between MC and data as the ratio between the two is always comprised between 0.8 and 1 also for values of x and y not centered on the origin. Only on the border of the EM module, the ratio increases to 2. The discrepancy on the horizontal axis is originated by an inefficiency of one pixel close to the edge of the detector. On the vertical axis, a misalignment of the detector produces a reduced coverage of the detector on the bottom edge.
All the selected MC generators reproduce the position previously obtained on real data. This means that for both data and the 5 generators, most of photons are concentrated exactly on the LHC beam axis, with just a small fraction uniformly distributed in the whole detector surface.

List of Figures

List of Tables

Bibliography

[1] ATLAS Collaboration, *Zero Degree Calorimeters for ATLAS* (2007).

[2] S. Tapprogge,*Prospects of Experimental Measurements at LHC to Better Understand Cosmic Ray Air Showers*, Phys. of At. Nucl. 67 1 (2004).

[3] E. Pare et al. *Phys. Lett.*, B242 (1990) 531.

[4] The LHCF Collaboration, *Measurements of photons and neutral pions in the very forward region of LHC*, Technical Design Report of the LHCf experiment (2006).

[5] S. Yoshida et al., *Astrophyis. J.*, 479 (1997) 547.

[6] S. Coleman and S. Glashow, *Phys. Rev.*, D59 (1999) 116008.

[7] H. Sato and T. Tati, *Theor. Phys.*, 47 (1972) 1788.

[8] Abu-Zayyard et al., *astro-ph/0208243*, PRL 92 (2004) 151101.

[9] Abu-Zayyard et al., *astro-ph/0208301*, Astropart.Phys. 23:157-174 (2005).

[10] Abu-Zayyard et al., *Phys. Rev. Lett.*, 92 (2004) 151106.

[11] P. Sommers et al., *Proc. of 29th Int. Cosmic Ray Conf.*, Pune (2005), in press (astro-ph/0507150).

[12] J. Bluemer for the Pierre Auger Collaboration in "*Frontiers of Cosmic Ray Science*", edited by T. Kajita, Y. Asaoka, A. Kawachi, Y. Matsubara and M. Sasaki, Universal Academy Press (2003) 361.

[13] The AUGER Collaboration, *Observation of the suppression of the flux of cosmic rays above* $410^{19}eV$ (2010).

[14] R.U. Abbasi et al., *Phys. Rev. Lett.* 100, 101101 (2008).

[15] G.J. Feldman and R.D. Cousins, *Phys. Rev. D* 57, 3873 (1998).

[16] M. Takeda et al., *Phys. Rev. Lett.*, 81 (1998) 1163.

[17] J. Knapp et al., *Astropart. Phys.*, 19 (2003) 77.

[18] V. Berezinsky, *astro-ph/0509069*, DOI:10.1088/1742-6596/47/1/018 (2005).

[19] S. Roesler, R. Engel, J. Ranft, *The MonteCarlo event generator DPMJET-III*, SLAC-PUB-8740 (2000).

[20] A. Baltz et al., *Nuc. Inst. and Meth.* A417, 1 (1998).

[21] M. Chiu et al., *Phys. Rev. Lett.* 89, 012302 (2002).ATLAS Collaboration.

[22] Y. Kawasaki et al., *Nucl. Inst. and Meth*, A564 378 (2006).

[23] http://www.hamamatsu.com/

[24] http://www.photonis.com/

[25] ATLAS Collaboration, *Level-1 Trigger. Technical Design Report*, http://atlasinfo.cern.ch/Atlas/GROUPS/DAQTRIG/TDR/V1REV1/L1TDR all.pdf (1998).

[26] ATLAS Collaboration, *ATLAS High-Level Trigger, Data Acquisition and Controls. Technical Design Report*, http://atlas-proj-hltdaqdcs-tdr.web.cern.ch/atlas-proj-hltdaqdcs-tdr/tdr-v1-r4/ PDF/TDR.pdf (2003).

[27] ATLAS Collaboration, *The ATLAS ROBIn Prototype*, http://robin-group.web.cern.ch/robin-group/ml.html (2004).

[28] R. Spiwoks, *ATLAS TTC Review*, (2002), http://atlas.web.cern.ch/Atlas/GROUPS/DAQTRIG/LEVEL1/ctpttc/meet ttc 150502.pdf.

[29] ATLAS Collaboration, *The ATLAS Level-1 Trigger, CTP*, http://atlas.web.cern.ch/Atlas/GROUPS/DAQTRIG/LEVEL1/ctpttc/L1CTP.html (2005).

[30] ATLAS Collaboration, *The Level One Central Trigger Operation* (2010).

[31] ATLAS Collaboration, *HOLA - High-speed Optical Link for Atlas, 2.0 Gbps S-LINK LSC and LDC S-LINK Interface*, http://www94.web.cern.ch/HSI/s-link/devices/hola/ (2002).

[32] ATLAS Collaboration, *The ATLAS Level-1 Calorimeter Trigger*, http://hepwww.rl.ac.uk/Atlas-L1/Home.html (2008).

[33] http://www.nichia.com/.

[34] A.A. Poblaguev, *Shower Reconstruction in the ATLAS ZDC* (2006).

[35] A.A. Poblaguev, *Comment to the ECAL calibration algorithm*, http://pubweb.bnl.gov/users/e865/www/calibration algorithm.pdf (2005).

[36] N.V. Mokhov, I.L. Rakhno, J.S. Kerby, J.B. Strait, *Protecting LHC IP1/IP5 Components Against Radiation from Colliding Beam Interactions*, (2002).

[37] Nicholas Metropolis and Stanislaw Ulam, The monte carlo method, *Journal of the American Statistical Association*, 44(247): 335-341 (1949). Doi: 10.2307/ 2280232. URL http://www.jstor.org/stable/2280232.

[38] Torbjorn Sjostrand, *Monte Carlo Tools* (2009).

[39] Torbjorn Sjostrand, Stephen Mrenna, and Peter Skands. *PYTHIA 6.4 Physics and Manual*, JHEP, 05:026 (2006).

[40] E. Boos et al. *Generic user process interface for event generators* (2001). URL http://arxiv.org/pdf/hep-ph/0109068v1.

[41] A. Donnachie and P. V. Landshoff, *Total cross sections*, Phys. Lett., B296:227-232 (1992). Doi: 10.1016/0370-2693(92)90832-O.

[42] Gerhard A. Schuler and Torbjorn Sjostrand, *Hadronic diffractive cross sections and the rise of the total cross section*, Phys. Rev., D49:2257-2267 (1994). Doi: 10.1103/PhysRevD.49.2257.

[43] Sjostrand, Torbjorn, *Pythia8 Web Page* (2007). URL http://home.thep.lu.se/ torbjorn/pythiaaux/present.html.

[44] Torbjorn Sjostrand and Maria van Zijl, *A Multiple Interaction Model for the Event Structure in Hadron Collisions*, Phys. Rev., D36:2019 (1987). Doi: 10.1103/ PhysRevD.36.2019.

[45] T. Sjostrand and P. Z. Skands, *Multiple interactions and the structure of beam remnants*, JHEP, 03:053 (2004).

[46] Torbjorn Sjostrand, Stephen Mrenna, and Peter Skands, *A Brief Introduction to PYTHIA 8.1*, Comput. Phys. Commun., 178:852-867 (2008). Doi: 10.1016/j.cpc. 2008.01.036.

[47] Klaus Werner. *The hadronic interaction model EPOS*, Nucl. Phys. Proc. Suppl., 175-176:81-87 (2008). doi: 10.1016/j.nuclphysbps.2007.10.012.

[48] A. V. Glushkov et al. *Muon content of ultra-high-energy air showers: Yakutsk data versus simulations*, JETP Lett., 87:190-194 (2008). doi: 10.1134/S0021364008040024.

[49] Klaus Werner, Fu-Ming Liu, and Tanguy Pierog, *Parton ladder splitting and the rapidity dependence of transverse momentum spectra in deuteron gold collisions at RHIC*, Phys. Rev., C74:044902 (2006). doi: 10.1103/PhysRevC.74.044902. URL http://arxiv.org/pdf/hep-ph/0506232.

[50] B. I. Abelev et al. *Strange particle production in p + p collisions at s**(1/2) = 200-GeV*, Phys. Rev., C75:064901 (2007). doi: 10.1103/PhysRevC.75.064901.

[51] Tanguy Pierog, *Forward physics : from SPS to LHC, what can we learn from air showers ?* (2009).

[52] K.Werner, Iu.Karpenko, T.Pierog, M. Bleicher, K. Mikhailov, *Evidence for Hydrodynamic Evolution in Proton-Proton Scattering at LHC Energies* (2010).

[53] B. Andersson, G. Gustafson, G. Ingelman, and T. Sjostrand, *Phys. Rept.* 97, 31 (1983).

[54] K. Werner, *Phys. Rep.* 232, 87 (1993).

[55] H. J. Drescher, M. Hladik, S. Ostapchenko, T. Pierog and K. Werner, *Phys. Rept.* 350, 93 (2001).

[56] A. Capella, U. Sukhatme, C.-I. Tan, and J. Tran Thanh Van, *Phys. Rept.* 236, 225 (1994).

[57] K.Werner, Iu.Karpenko, T. Pierog, M. Bleicher, K. Mikhailov, arXiv:1004.0805, *Phys. Rev. C* (2010).

[58] S. Porteboeuf and K. Werner, *Generation of complete events containing very highp(T) jets*, Eur. Phys. J., C62:145-150 (2009). Doi: 10.1140/epjc/s10052-008-0840-y.

[59] Sami Kama, *Automatic Monte-Carlo Tuning for Minimum Bias Events at the LHC*, Dissertation, Humboldt-Universitt zu Berlin (2010).

[60] F. James and M. Roos, *Minuit: A System for Function Minimization and Analysis of the Parameter Errors and Correlations*, Comput. Phys. Commun., 10:343-367 (1975). Doi: 10.1016/0010-4655(75)90039-9.

[61] Andy Buckley, Hendrik Hoeth, Heiko Lacker, Holger Schulz, and Jan Eike von Seggern, *Systematic event generator tuning for the LHC*, Eur.Phys.J.C65:331-357 (2010).

[62] Andy Buckley, Hendrik Hoeth, Holger Schulz, and Jan Eike von Seggern, *Monte Carlo event generator validation and tuning for the LHC*, PoS ACAT08:112 (2009).

[63] Andy Buckley, Hendrik Hoeth, Heiko Lacker, Holger Schulz, and Eike von Seggern, *Monte Carlo tuning and generator validation*, MCnet/09/12 (2009).

[64] P. Abreu et al. *Tuning and test of fragmentation models based on identified particles and precision event shape data*, Z. Phys., C73:11-60 (1996). Doi: 10.1007/s002880050295.

[65] Holger Schulz, *Systematic Event Generator Tuning with Professor*, Diploma thesis, Humboldt-Universitt zu Berlin (2009). URL http://projects.hepforge.org/professor/diplomathesis.pdf.

[66] ATLAS Collaboration, *Measurements of the pseudorapidity dependence of the total transverse energy in proton-proton collisions at* $\sqrt{s} = 7$ *TeV with ATLAS* (2012).

[67] Agostinelli, S.; Allison, J.; Amako, K.; Apostolakis, J.; Araujo, H.; Arce, P.; Asai, M.; Axen, D. et al. (2003), *Geant4-a simulation toolkit*, Nuclear Instruments and Methods in Physics Research Section A (Accelerators, Spectrometers, Detectors and Associated Equipment) 506 (3): 250.